BULK AND INTERFACIAL NATURE OF SPIN HALL MAGNETOTRANSPORT WITH IRON GARNET HETEROSTRUCTURES

LI PEIGEN

PhD

The Hong Kong Polytechnic University

2025

The Hong Kong Polytechnic University

Department of Applied Physics

Bulk and Interfacial Nature of Spin Hall Magnetotransport with Iron Garnet Heterostructures

A thesis submitted in partial fulfilment of the requirements for the degree of Doctor of Philosophy

LI Peigen

August 2024

Certificate of Originality

I hereby declare that this thesis is my own work and that, to the best of my knowledge and belief, it reproduces no material previously published or written, nor material that has been accepted for the award of any other degree or diploma, except where due acknowledgement has been made in the text.

_____ (Signed)

LI PEIGEN (Name of student)

Abstract

Artificial intelligence technologies have put forward more stringent requirements for information storage devices. Compared with electronic devices made of traditional semiconductor materials, spintronic devices have advantages such as low energy dissipation and fast writing and reading of data. Taking the device composed of magnetic insulator (MI) and heavy metal (HM) as an example. Due to the low damping of MI and its ability to transmit spin information through magnon, combined with the spin orbit coupling effect of MI/HM, high energy efficiency can be achieved with extremely low Ohmic losses. Therefore, such devices are expected to be widely adopted in the next-generation storage devices.

The spin transport mechanism of MI/HM systems is complicated, especially for heterostructure composed of platinum (Pt) and ferrimagnetic rare earth iron garnet (REIG) with compensation phenomenon, which leads to anomalous spin magnetotransport behavior and has attracted much attention. This thesis is based on the study of magnetic and electrical properties of the $Tb_3Fe_5O_{12}$ (TbIG)/Pt systems, including the magnetization compensation behavior, the presence of two sign cross-over points in anomalous Hall effect resistance (R_{AHE}) vs. temperature plot, the impact of REIG/HM interface and REIG bulk on spin magnetotransport. Specifically, the content is organized as follows:

The first part introduces the influence of ultra-thin garnet-like spacers ($Y_3Al_5O_{12}$ (YAG) and $Gd_3Ga_5O_{12}$ (GGG)) on the spin magnetotransport of TbIG/Pt system. Hall devices are fabricated by pulsed laser deposition (PLD), magnetron sputtering (MS), and photolithography, and the influence of different spacer thicknesses on magnetic proximity effect (MPE) and spin Hall transport are studied.

Then, I construct a bilayer REIG system composed of TbIG and $Eu_3Fe_5O_{12}$ (EuIG). A thickness-dependent compensation temperature (T_{comp}) is realized by changing the

thickness of EuIG. The exchange coupling between TbIG and EuIG is analyzed, and the effect on two R_{AHE} sign cross-over points is systematically presented.

Finally, I introduce the REIG bulk effect on spin transport, by investigating a REIG sandwich structure based on TbIG and EuIG. It is realized through modulating the individual layer thickness of TbIG/EuIG/TbIG/Pt with fixed total thickness. As TbIG gradually moves away from the Pt, the different contributions of REIG/Pt interface and REIG bulk on two R_{AHE} cross-over points are discussed.

Scholarly activities

Journal publications

1. J.M. Liang, X.W. Zhao, Y.K. Liu, **P.G. Li**, S.M. Ng, H.F. Wong, W.F. Cheng, Y. Zhou, J.Y. Dai, C.L. Mak, C.W. Leung, The thickness effect on the compensation temperature of rare-earth garnet thin films, Applied Physics Letters, 122 (2023) 242401.
2. J.M. Liang, X.W. Zhao, X. Yuan, Y.K. Liu, S.M. Ng, H.F. Wong, **P.G. Li**, Y. Zhou, F.X. Zhang, C.L. Mak, C.W. Leung, Interlayer antiferromagnetic coupling in $Tb_3Fe_5O_{12}/Y_3Fe_5O_{12}$ bilayers, Applied Physics Letters, 123 (2023) 092405.
3. **P.G. Li**, J.M. Liang, S.M. Ng, H.F. Wong, Y. Zhou, L.J. Huang, K.W. Lin, Y.H. Tsang, C.L. Mak, C.W. Leung, Tunable compensation temperature through ferromagnetic coupling in perpendicular $Tb_3Fe_5O_{12}/Eu_3Fe_5O_{12}$ bilayer heterostructure, Journal of Magnetism and Magnetic Materials, 592, (2024) 171785.
4. **P.G. Li**, S.M. Ng, X. Yuan, F.X. Zhang, H.F. Wong, Z.Q. Chu, P. Cao, C.W. Leung, Spin magnetotransport in rare-earth iron garnet (REIG)/Pt: the effects of modulated bulk and REIG/Pt interfaces, APL Materials, 12 (2024) 081114.
5. **P.G. Li**, S.M. Ng, X. Yuan, F.X. Zhang, H.F. Wong, C.W. Leung, Impact of ultrathin garnet spacers on the magnetotransport in $Tb_3Fe_5O_{12}$/Pt bilayers, Applied Physics Letters, 125 (2024) 102404.

Conference Poster

1. **P.G. Li**, J.M. Liang, X.W. Zhao, S.M. Ng, H.F. Wong, C.L. Mak, C.W. Leung, Impact of ultrathin garnet spacers on the magnetotransport in Pt/$Tb_3Fe_5O_{12}$ bilayers, The 67th Conference on Magnetism and Magnetic Materials, Minneapolis, 2022.

Acknowledgements

Time flies and my PhD study is coming to an end. The experience is one of the most unforgettable memories in my life. Looking back on the first year of my PhD study, I entered a research field that I had never encountered before. Along the way, I stumbled and gradually became familiar with the field I needed to delve into. I am grateful for the success and failure I have experienced during my PhD studies, which will be my lifelong wealth. I also want to thank many people who have helped me during this period.

The first person I would like to thank the most is my chief supervisor, Dr. Chi Wah LEUNG. He carefully guided me on how to become a qualified researcher. His rigorous attitude and keen insight into science helped me avoid many detours. I want to say thank you sincerely.

I would like to offer my special thanks to Dr. Hon Fai WONG and Dr. Sheung Mei NG for their help in the experiments, guiding me in using the experimental equipment and analyzing the problems encountered. I also want to thank them for giving me a lot of care in my life. I am also particularly grateful to the group members, Dr. Xu Wen ZHAO and Dr. Jing Ming LIANG. They imparted their experimental experience to me and patiently guided me in using the instruments. Special thanks also to all friends of the DE706 office, for their support and companionship, which has made my PhD study exciting.

Finally, I would like to thank my family for their encouragement and care. You are the most vital support on my life journey.

Table of contents

List of figures

List of tables

List of abbreviations

MI	Magnetic insulator
HM	Heavy metal
REIG	Rare earth iron garnet
GMR	Giant magnetoresistance
TMR	Tunneling magnetoresistance
SHE	Spin Hall effect
STT	Spin-transfer torque
SOC	Spin-orbit coupling
ISHE	Inverse spin Hall effect
FMI	Ferromagnetic insulator
SMR	Spin Hall magnetoresistance
AHE	Anomalous Hall effect
T_c	Curie temperature
T_{comp}	Compensation temperature
M_s	Saturation magnetization
R_{AHE}	Anomalous Hall resistance
MPE	Magnetic proximity effect
TbIG	$Tb_3Fe_5O_{12}$
PLD	Pulsed laser deposition
MS	Magnetron sputtering
EuIG	$Eu_3Fe_5O_{12}$
MRAM	Magnetoresistive random access memory
DRAM	Dynamic random access memory
QSHE	Quantum spin Hall effect
GGG	$Gd_3Ga_5O_{12}$
YAG	$Y_3Al_5O_{12}$

YIG	$Y_3Fe_5O_{12}$
MOKE	Magneto-optic Kerr effect
XMCD	X-ray magnetic circular dichroism
PMA	Perpendicular magnetic anisotropy
STO	$SrTiO_3$
PVD	Physical vapor deposition
XRD	X-ray diffraction
AFM	Atomic force microscope
TEM	Transmission electron microscope
HRXRD	High-resolution XRD
XRR	X-ray reflectivity
SEM	Scanning electron microscopy
STEM	Scanning transmission electron microscopy
VSM	Vibration sample magnetometer
PPMS	Physical property measurement system
T_1	The second sign cross-over of R_{AHE}
EDS	X-ray spectroscopy
FWHM	Full-width at half-maximum
FIB	Focused ion beam
H_c	Coercivity
R_{AHE}^0	R_{AHE} at zero magnetic field
PNR	Polarized neutron reflectometry
HAADF	High-angle annular dark field

Chapter 1 Introduction

1.1 Background and objective

Spintronics [1], as an emerging scientific and technological field, has attracted many researchers to explore related theories and applications in recent decades due to its enormous potential. A spintronic device can serve as a carrier and a tool of information, because the spin of electrons can be controlled by electric or magnetic fields to affect their degrees of freedom [2], thereby affecting the properties of materials such as magnetism.

With the discovery of the giant magnetoresistance (GMR) in 1988 [3, 4], spintronics has entered a path of rapid development. Subsequently, tunneling magnetoresistance (TMR) [5, 6], spin Hall effect (SHE) [7, 8], and spin-transfer torque (STT) [9, 10], etc. were discovered, laying the foundation for the new generation of information storage technology. Spintronics is expected to lead the next round of the information industry revolution. Some new and efficient spintronic devices have been applied to information storage and logic calculation for artificial intelligence.

As an important branch of condensed matter physics, a focus in spintronics research is the coupling effect of electron spin and charge, which is strongly related to the generation and detection of spin currents [11]. However, the regulation and detection of spin currents is a complex and challenging issue.

The discovery of the SHE opens a window for studying spin current transport. The SHE commonly appears in systems with strong spin-orbit coupling (SOC) [12]. For example, when a charge current is applied to a heavy metal with strong SOC (such as Pt), the electron flow in Pt will deviate from its original direction. Electrons with different spin directions (up or down) will deflect in opposite directions, resulting in spin currents perpendicular to the direction of charge current and spin polarization [13]. In addition, SHE also has a reciprocal effect known as the inverse spin Hall effect (ISHE) [14]. The ISHE is the process of generating charge current through spin current, which

can be used to detect spin current.

One of the hot research topics related to SHE is the spin Hall magnetoresistance (SMR) [15]. Up to now, most of the relevant studies are based on ferrimagnetic insulator (FMI)/heavy metal (HM) systems, especially in $Y_3Fe_5O_{12}$ (YIG)/Pt heterostructures [16-18]. Due to the low intrinsic damping coefficient of YIG and the strong SOC of Pt [19], the transmission distance of the spin signal in this system is much better than in other materials. For example, Comelissen *et al.* measured a spin transmission distance of 40 μm at room temperature in the YIG/Pt system [20]. Interestingly, due to the recently observed angular dependence of SMR [21], the FMI/HM interface has attracted great attention. SMR originates from the interaction between spin Hall-induced spin accumulation at the FMI/HM interface and the magnetization of FMI [22-24]. In studying SMR, an anomalous Hall effect (AHE)-like behavior was also found and is termed spin Hall-AHE (SH-AHE) [25]. To study the interesting phenomena, magnetic insulators of rare earth (RE) iron garnets (IG) are widely used for analyzing spin Hall behavior.

REIG has the general chemical formula $RE_3Fe_5O_{12}$. As a ferrimagnetic insulator, REIG has a cubic symmetry that belongs to the $Ia-\bar{3}d$ space group [26] with a complex crystal structure. REIGs usually display two temperature peculiarities: one is Curie temperature (T_c), which is determined by the REIG composition and crystal structure. The other peculiarity is the magnetization compensation temperature (T_{comp}) [28, 29], at which the saturation magnetization (M_s) of the material temporarily disappears. T_{comp} can be explained by the competition between magnetic moments of RE^{3+} and Fe^{3+} sublattices [30]. Their moments are antiparallel and completely cancel out at T_{comp}. It can be noted that the YIG does not have T_{comp} as Y^{3+} is non-magnetic [31]. Representative REIGs with T_{comp} include $Gd_3Fe_5O_{12}$ (GdIG) [32], $Tb_3Fe_5O_{12}$ (TbIG) [33], and $Dy_3Fe_5O_{12}$ (DyIG) [34].

In REIG/HM systems, the existence of T_{comp} can greatly affect spin Hall magnetotransport. For example, in the magnetotransport measurements of GdIG/Pt system, the existence of T_{comp} is accompanied by the sign flipping of anomalous Hall

resistance (R_{AHE}) and the spin Seebeck voltage [35, 36]. This interesting phenomenon means that fast logical calculation and information storage can be achieved by controlling T_{comp}. In REIG, T_{comp} can be regulated by doping [37], layer thickness [38], stress [39], or through the construction of multilayer stacks [40]. The diverse routes of T_{comp} regulation makes the study of spin transport in REIG/HM systems an attractive field.

The REIG/HM interface plays an important role in SMR, as the quality of interface would alter the spin Hall effect and magnetic proximity effect (MPE) of heterostructures. There was some controversy about the origin of SMR. In early studies, it was suggested that SMR and related spin Hall-induced AHE are determined by the spin diffusion length, spin Hall angle, heavy metal layer thickness, and magnetization direction of the magnetic layer, etc. [41], and the spin-mixing conductivity formula ($G = G_r + iG_i$) was proposed [42]. With in-depth research, the magnetic proximity effect (MPE) within HM layer in the REIG/HM interface was also considered to contribute to SMR [43, 44].

To study these interface effects (MPE and SHE), efforts have been made to explore specific transport mechanisms, such as through additional interlayers. For example, Cu inserted at the $Tm_3Fe_5O_{12}$ (TmIG)/Pt interface was used to study the relative contributions of SHE and MPE [45]. In addition, antiferromagnetic spacers (such as CoO or NiO) were inserted between YIG and Pt. Contrary to the typical positive SMR behavior, negative SMR was found at low temperatures for such systems [46, 47]. However, there are limitations in using such spacers in studying heterogeneous interfaces, such as the parasitic magnetic contributions by antiferromagnetic spacers, or the significant lattice mismatch between REIG and spacer materials. Besides, there are few reports about the effect of modulating FMI bulk on spin magnetotransport through a fixed REIG/HM interface. The impact of additional interfaces caused by multilayer stacking, or the overall FMI situation, should be considered in REIG/HM heterostructure. These issues are worth exploring.

In this project, TbIG with magnetization compensation behavior was selected as the FMI layer, and Pt with strong SOC was chosen as the HM layer, with a focus on

studying the bulk and interfacial nature of spin Hall magnetotransport. TbIG/Pt heterostructures were constructed using pulsed laser deposition (PLD) and magnetron sputtering (MS). Also, a multilayer stacking method was utilized to regulate the magnetic compensation point, providing useful reference for the design of spin magnon valves.

1.2 Significance of this work

The REIG films, and the interface nature of REIG/HM system, are critical and worth studying. On one hand, REIGs with magnetization compensation have great potential for application in controllable memory devices. On the other hand, the spin transport is greatly influenced by the REIG/HM interface, and the successful control of the interface has significant impact for the development of spintronic devices.

Here, I choose TbIG with T_{comp} (bulk value around 248 K) as the REIG material [48]. TbIG/Pt heterostructures are prepared in this work, and their spin magnetotransport properties are systematically analyzed, particularly around T_{comp}. Epitaxial TbIG films are grown on lattice-matching substrates before they are covered with Pt and patterned into Hall bar structures. Magnetoresistance and AHE measurements on those systems are conducted as functions of temperature and layer thicknesses. I construct multilayer structures to regulate the compensation behavior, and systematically analyze the contribution of spin transport from the TbIG/Pt interface to the TbIG bulk. The results will provide a holistic picture of the SMR behavior and the experimental basis for building better models of SMR-related phenomena.

1.3 Outlines of thesis

This thesis is based on the study of magnetic and electrical properties of TbIG/Pt systems, including the magnetization compensation behavior, the R_{AHE} sign cross-over point, REIG/HM interface effects, and FMI bulk effects on spin magnetotransport. The thesis is organized as follows:

(1) In Chapter 2, I will briefly introduce the development history of spintronics

and the fundamental theory related to SMR. Also, the MPE and SHE mechanism at REIG/HM interfaces will be introduced. The impact of T_{comp} on REIG/HM heterojunctions will be summarized, and methods used by other researchers on studying interface and T_{comp} regulation are discussed. Through the research and analysis of the existing results, a deeper understanding of spin Hall transport can be achieved, providing guidance on the design of the experiments.

(2) Chapter 3 describes the overall experimental design, including sample preparation process, basic principles and experimental conditions of thin film deposition, and characterization methods of the samples (including microstructural, magnetic, and electrical performance characterizations).

(3) Chapter 4 introduces the influence of ultra-thin garnet spacers on the magnetotransport of TbIG/Pt systems. Hall devices are fabricated by the methods in Chapter 3, and the influence of different spacer thicknesses on MPE and spin Hall transport are studied.

(4) Chapter 5 explores the bilayer FMI system composed of TbIG and $Eu_3Fe_5O_{12}$ (EuIG). EuIG does not exhibit T_{comp} while possess good lattice matching with TbIG, which permits the observation of T_{comp} variations in such bilayer FMI system. The thickness-dependent T_{comp} is realized by changing the thickness of EuIG in the bilayer stacks. The interlayer coupling between TbIG and EuIG is analyzed, and the effect on the R_{AHE} cross-over points is systematically presented.

(5) Chapter 6 introduces the REIG bulk effect on spin transport. Trilayer REIG based on TbIG and EuIG are deposited, and different REIG/Pt interfaces are realized through modulating the TbIG layer thicknesses in the TbIG/EuIG/TbIG/Pt structure while keeping a fixed total thickness. As the TbIG gradually moves away from the Pt layer, the different contributions of REIG/Pt interfaces and REIG bulk on the R_{AHE} cross-over points are discussed.

(6) Chapter 7 summarizes the important conclusions and unresolved issues of this project, and briefly introduces possible future research directions and prospects.

References for Chapter 1

[1] I. Žutić, J. Fabian, S. D. Sarma, Spintronics: Fundamentals and applications, Rev. Mod. Phys. 76 (2004) 323-411.

[2] W.-H. Li, C.-W. Wang, D. Hsu, C.-H. Lee, C.-M. Wu, C.-C. Chou, H.-D. Yang, Y. Zhao, S. Chang, J.W. Lynn, H. Berger, Interplay between the magnetic and electric degrees of freedom in multiferroic Co_3TeO_6, Phys. Rev. B 85 (2012) 094431.

[3] M.N. Baibich, J.M. Broto, A. Fert, F. Nguyen Van Dau, F. Petroff, P. Etienne, G. Creuzet, A. Friederich, J. Chazelas, Giant magnetoresistance of (001)Fe/(001)Cr magnetic superlattices, Phys. Rev. Lett. 61 (1988) 2472-2475.

[4] G. Binasch, P. Grunberg, F. Saurenbach, W. Zinn, Enhanced magnetoresistance in layered magnetic structures with antiferromagnetic interlayer exchange, Phys. Rev. B Condens. Matter. 39 (1989) 4828-4830.

[5] J. Inoue, S. Maekawa, Theory of tunneling magnetoresistance in granular magnetic films, Phys. Rev. B 53 (1996) R11927.

[6] T. Miyazaki, N. Tezuka, Giant magnetic tunneling effect in $Fe/Al_2O_3/Fe$ junction. J. Magn. Magn. Mater. 139 (1995) L231-L234.

[7] J. Sinova, D. Culcer, Q. Niu, N.A. Sinitsyn, T. Jungwirth, A.H. MacDonald, Universal intrinsic spin Hall effect, Phys. Rev. Lett. 92 (2004) 126603.

[8] J. E. Hirsch, Spin hall effect, Phys. Rev. Lett. 83 (1999) 1834-1837.

[9] D.C. Ralph, M.D. Stiles, Spin transfer torques, J. Magn. Magn. Mater. 320 (2008) 1190-1216.

[10] M.D. Stiles, A. Zangwill, Anatomy of spin-transfer torque, Phys. Rev. B 66 (2002) 014407.

[11] J.C. Sanchez, L. Vila, G. Desfonds, S. Gambarelli, J.P. Attane, J.M. De Teresa, C. Magen, A. Fert, Spin-to-charge conversion using Rashba coupling at the interface between non-magnetic materials, Nat. Commun. 4 (2013) 2944-2950.

[12] J. Sinova, S.O. Valenzuela, J. Wunderlich, C.H. Back, T. Jungwirth, Spin Hall

effects, Rev. Mod. Phys. 87 (2015) 1213-1260.

[13] H. Nakayama, M. Althammer, Y.T. Chen, K. Uchida, Y. Kajiwara, D. Kikuchi, T. Ohtani, S. Geprags, M. Opel, S. Takahashi, R. Gross, G.E. Bauer, S.T. Goennenwein, E. Saitoh, Spin Hall magnetoresistance induced by a nonequilibrium proximity effect, Phys. Rev. Lett. 110 (2013) 206601.

[14] B.F. Miao, S.Y. Huang, D. Qu, C.L. Chien, Inverse spin Hall effect in a ferromagnetic metal, Phys. Rev. Lett. 111 (2013) 066602.

[15] Y.T. Chen, S. Takahashi, H. Nakayama, M. Althammer, S.T. Goennenwein, E. Saitoh, G.E. Bauer, Theory of spin Hall magnetoresistance (SMR) and related phenomena, J. Phys. Condens. Matter. 28 (2016) 103004.

[16] B.F. Miao, S.Y. Huang, D. Qu, C.L. Chien, Physical origins of the new magnetoresistance in Pt/YIG, Phys Rev Lett, 112 (2014) 236601.

[17] S. Velez, V.N. Golovach, A. Bedoya-Pinto, M. Isasa, E. Sagasta, M. Abadia, C. Rogero, L.E. Hueso, F.S. Bergeret, F. Casanova, Hanle Magnetoresistance in Thin Metal Films with Strong Spin-Orbit Coupling, Phys. Rev. Lett. 116 (2016) 016603.

[18] S. Meyer, M. Althammer, S. Geprägs, M. Opel, R. Gross, S.T.B. Goennenwein, Temperature dependent spin transport properties of platinum inferred from spin Hall magnetoresistance measurements, Appl. Phys. Lett. 104 (2014) 242411.

[19] S.R. Marmion, M. Ali, M. McLaren, D.A. Williams, B.J. Hickey, Temperature dependence of spin Hall magnetoresistance in thin YIG/Pt films, Phys. Rev. B 89 (2014) 220404(R).

[20] L.J. Cornelissen, J. Liu, R.A. Duine, J.B. Youssef, B.J. van Wees, Long-distance transport of magnon spin information in a magnetic insulator at room temperature, Nat. Phys. 11 (2015) 1022-1026.

[21] L.K. Zou, Y. Zhang, L. Gu, J.W. Cai, L. Sun, Tunable angular-dependent magnetoresistance correlations in magnetic films and their implications for spin Hall magnetoresistance analysis, Phys. Rev. B 93 (2016) 075309.

[22] M. Isasa, S. Vélez, E. Sagasta, A. Bedoya-Pinto, N. Dix, F. Sánchez, L.E. Hueso, J. Fontcuberta, F. Casanova, Spin Hall magnetoresistance as a probe for surface

magnetization in Pt/$CoFe_2O_4$ bilayers, Phys. Rev. Appl. 6 (2016) 034007.

[23] P.M. Haney, H.-W. Lee, K.-J. Lee, A. Manchon, M.D. Stiles, Current induced torques and interfacial spin-orbit coupling: Semiclassical modeling, Phys. Rev. B 87 (2013) 174411.

[24] P. Blonski, S. Dennler, J. Hafner, Strong spin-orbit effects in small Pt clusters: geometric structure, magnetic isomers and anisotropy, J. Chem. Phys. 134 (2011) 034107.

[25] L. Liu, Z. Fan, Z. Chen, Z. Chen, Z. Ye, H. Zheng, Q. Zeng, W. Jia, S. Li, N. Wang, J. Liu, L. Ma, T. Lin, M. Qiu, S. Li, P. Han, J. Shi, H. An, Spin–orbit torques in heavy metal/ferrimagnetic insulator bilayers near compensation, Appl. Phys. Lett. 119 (2021) 052401.

[26] S. Geller, M. A. Gilleo, The crystal structure and ferrimagnetism of yttrium-iron garnet, $Y_3Fe_2(FeO_4)_3$, J. Phys Chem. Solids. 3 (1957) 30-36.

[27] T. Takeuchi, N. Ohta, Y. Sugita, Curie temperatures and anisotropy fields in very thin garnet films, J. Magn. Magn. Mater. 31 (1983) 925-926.

[28] A. Budkowski, A. Szytuła, D. Rodic, R. Duraj, J. Mayer, J. Sciesinski, V. Spasojevic, The compensation point in reig and some of its properties, J. Magn. Magn. Mater. 78 (1989) 226-236.

[29] L. Liensberger, A. Kamra, H. Maier-Flaig, S. Geprags, A. Erb, S.T.B. Goennenwein, R. Gross, W. Belzig, H. Huebl, M. Weiler, Exchange-Enhanced Ultrastrong Magnon-Magnon Coupling in a Compensated Ferrimagnet, Phys. Rev. Lett. 123 (2019) 117204.

[30] J.S. McCloy, B. Walsh, Sublattice Magnetic Relaxation in Rare Earth Iron Garnets, IEEE. T. Magn. 49 (2013) 4253-4256.

[31] N.B. Ibrahim, Y. Noratiqah, The microstructure and magnetic properties of yttrium iron garnet film prepared using water-alcohol solvents, J. Magn. Magn. Mater. 510 (2020) 166953.

[32] S. Geprags, A. Kehlberger, F.D. Coletta, Z. Qiu, E.J. Guo, T. Schulz, C. Mix, S. Meyer, A. Kamra, M. Althammer, H. Huebl, G. Jakob, Y. Ohnuma, H. Adachi, J.

Barker, S. Maekawa, G.E.W. Bauer, E. Saitoh, R. Gross, S.T.B. Goennenwein, M. Klaui, Origin of the spin Seebeck effect in compensated ferrimagnets, Nat. Commun. 7 (2016) 10452.

[33] Y.K. Liu, H.F. Wong, K.K. Lam, K.H. Chan, C.L. Mak, C.W. Leung, Anomalous Hall effect in Pt/$Tb_3Fe_5O_{12}$ heterostructure: Effect of compensation point, J. Magn. Magn. Mater. 468 (2018) 235-240.

[34] J.J. Bauer, E.R. Rosenberg, S. Kundu, K.A. Mkhoyan, P. Quarterman, A.J. Grutter, B.J. Kirby, J.A. Borchers, C.A. Ross, Dysprosium iron garnet thin films with perpendicular magnetic anisotropy on silicon, Adv. Electron. Mater. 6 (2019) 1900820.

[35] Y. Li, D. Zheng, C. Liu, C. Zhang, B. Fang, A. Chen, Y. Ma, A. Manchon, X. Zhang, Current-Induced Magnetization Switching Across a Nearly Room-temperature compensation point in an insulating compensated ferrimagnet, ACS Nano 16 (2022) 8181-8189.

[36] A. Chanda, C. Holzmann, N. Schulz, J. Seyd, M. Albrecht, M.H. Phan, H. Srikanth, Scaling of the thermally induced sign inversion of longitudinal spin Seebeck effect in a compensated ferrimagnet: Role of magnetic anisotropy, Adv. Funct. Mater. 32 (2021) 2109170.

[37] T. Xu, Y. Cheng, Y. Dong, H. Bai, H.-A. Zhou, X. Shu, P. Gargiani, M. Valvidares, P. Yu, W. Jiang, Evolution of compensated magnetism and spin-torque switching in ferrimagnetic $Fe_{1-x}Tb_x$, Phys. Rev. Appl. 19 (2023) 034088.

[38] J.M. Liang, X.W. Zhao, Y.K. Liu, P.G. Li, S.M. Ng, H.F. Wong, W.F. Cheng, Y. Zhou, J.Y. Dai, C.L. Mak, C.W. Leung, The thickness effect on the compensation temperature of rare-earth garnet thin films, Appl. Phys. Lett. 122 (2023) 242401.

[39] Y. Li, X. Yang, H. Bai, M. Wang, D. Cheng, C. Song, Z. Yuan, Y. Liu, Z. Shi, Strain-tunable magnetic compensation temperature of epitaxial $Tb_3Fe_5O_{12}$ thin films, Phys. Rev. B 108 (2023) 184403.

[40] S. Becker, Z. Ren, F. Fuhrmann, A. Ross, S. Lord, S. Ding, R. Wu, J. Yang, J. Miao, M. Kläui, G. Jakob, Magnetic coupling in $Y_3Fe_5O_{12}$/$Gd_3Fe_5O_{12}$

heterostructures, Phys. Rev. Appl. 16 (2021) 014047.

[41] N. Vlietstra, J. Shan, V. Castel, J. Ben Youssef, G.E.W. Bauer, B.J. van Wees, Exchange magnetic field torques in YIG/Pt bilayers observed by the spin-Hall magnetoresistance, Appl. Phys. Lett. 103 (2013) 032401.

[42] S. Meyer, R. Schlitz, S. Geprägs, M. Opel, H. Huebl, R. Gross, S.T.B. Goennenwein, Anomalous Hall effect in YIG|Pt bilayers, Appl. Phys. Lett. 106 (2015) 132402.

[43] Y.M. Lu, Y. Choi, C.M. Ortega, X.M. Cheng, J.W. Cai, S.Y. Huang, L. Sun, C.L. Chien, Pt magnetic polarization on $Y_3Fe_5O_{12}$ and magnetotransport characteristics, Phys. Rev. Lett. 110 (2013) 147207.

[44] R. Yadav, A. Bake, W.T. Lee, Y.-K. Liu, D.R.G. Mitchell, X.-R. Yang, D.L. Cortie, K.-W. Lin, C.W. Leung, Interfacial spin structures in Pt/$Tb_3Fe_5O_{12}$ bilayer films on $Gd_3Ga_5O_{12}$ substrates, Phys. Rev. Mater. 7 (2023) 124407.

[45] C. Tang, P. Sellappan, Y. Liu, Y. Xu, J.E. Garay, J. Shi, Anomalous Hall hysteresis in $Tm_3Fe_5O_{12}$/Pt with strain-induced perpendicular magnetic anisotropy, Phys. Rev. B 94 (2016) 140403(R).

[46] D. Hou, Z. Qiu, J. Barker, K. Sato, K. Yamamoto, S. Velez, J.M. Gomez-Perez, L.E. Hueso, F. Casanova, E. Saitoh, Tunable sign change of spin Hall magnetoresistance in Pt/NiO/YIG structures, Phys. Rev. Lett. 118 (2017) 147202.

[47] W. Lin, C.L. Chien, Electrical detection of spin backflow from an antiferromagnetic insulator/$Y_3Fe_5O_{12}$ interface, Phys. Rev. Lett. 118 (2017) 067202.

[48] D. Rodić, Z.Tomkowicz, L. A. Novaković, Szytula, M. L. Napijalo, The initial magnetic susceptibilities of $Gd_3Fe_5O_{12}$ and $Tb_3Fe_5O_{12}$ in the compensation point region. Solid State Commun. 73 (1990) 243-246.

Chapter 2 Literature review

2.1 Spintronics and spin current

2.1.1 Magnetism and spintronics

The rapid development of modern spintronics is closely related to the advancement of information storage technology. There is continuous evolvement of our understanding in magnetic materials and the role of electron spin in high-density computer storage. The concept of spin was based on the Pauli exclusion principle and spin-related mathematical theory [1], followed by Dirac's equation of electron motion [2]. From then on, many interesting spin-related phenomena were observed through spintronic devices. Fig. 2.1 summarizes some vital phenomena related to spintronics [3].

Spintronics is strongly related to magnetism because magnetic moments are closely associated with the spin angular momentum of charge carriers. Magnetism has many applications [4], such as hard disk read heads, magnetic recording components, magnetic field sensors, etc. However, the real driving force behind the commercial impact of spintronics is the discovery of giant magnetoresistance (GMR) [5, 6]. Grünberg *et al*. found that Fe/Cr/Fe multilayer films exhibit antiferromagnetic exchange interactions at room temperature, accompanied by a significant change in resistance at different magnetization orientation states of the Fe layers [6]. A low resistance value is displayed if the magnetization directions of adjacent Fe layers are parallel, while relatively high resistance is observed if they are antiparallel. Meanwhile, Fert *et al*. observed similar GMR phenomena at low temperatures (~4.2 K) in Fe (001)/Cr (001) superlattice samples [5].

The effect of GMR generated by sandwich structured film has been adopted in the application of hard disk read heads, confirming the market value of spin transport of electrons. Meanwhile, Moodera *et al*. observed a significant tunneling

magnetoresistance (TMR) in Fe/Al_2O_3/Fe multilayers [7], which became another milestone discovery in the commercialization of spintronics. In 2001, it was theoretically predicted that epitaxial Fe/MgO/Fe tunnel junction TMR could reach 1000% [8, 9], and TMR of 200% was realized at room temperature experiments in 2004 [10, 11]. Until now, the TMR ratio has reached 631% in CoFe/MgO/CoFe (001) devices [12].

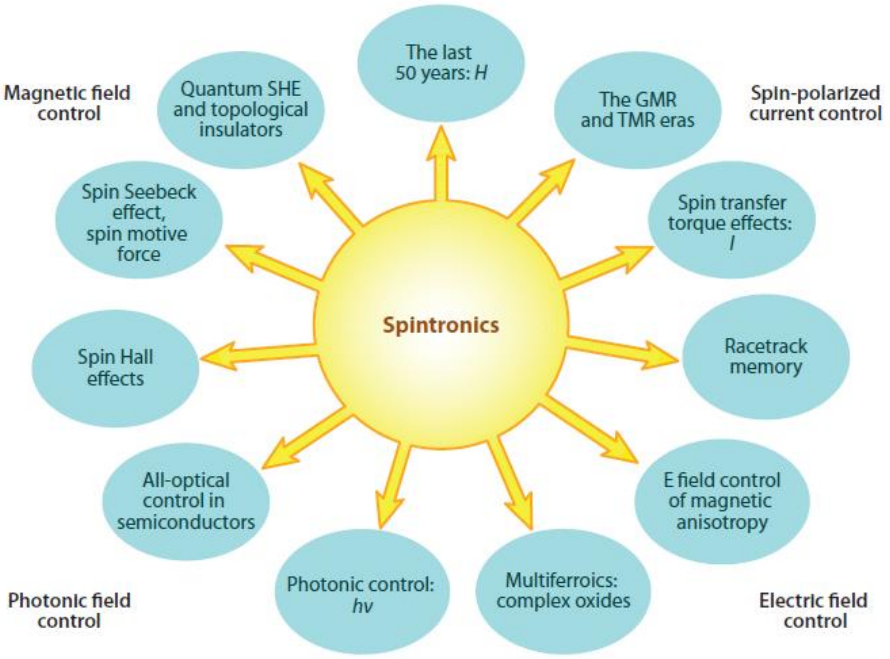

Fig. 2.1 Overview of spin phenomena related to spintronics [3].

The spin-transfer torque (STT) is defined as an effect that uses spin-polarized current to change the magnetization direction of the magnetic layers in a spin valve or magnetic tunnel junction, through the transfer of angular momentum in multilayer films. STT has paved the way for magnetoresistive random access memory (MRAM) applications [13, 14]. Some companies have developed STT-MRAM products. Such STT-MRAM technologies can compete with dynamic random access memory (DRAM) products, such as the 256 Mbit STT-MRAM device fabricated by Everspin [15]. STT is also applied to other spintronic products, such as racetrack memory and spin-logic devices. The racetrack memory designed by IBM has high density and reading speed advantages [16].

The spin Hall effect is another critical phenomenon in spintronics. Charge current can generate spin current and spin accumulation through the SHE [17]. SHE and its inverse effect (ISHE) became the theoretical basis for generating and detecting spin currents. Simultaneously, the quantum spin Hall effect (QSHE) was observed in graphene [18], bringing spintronics into the field of quantum technology, especially through the application of topological materials [19].

Besides, the spin Seebeck effect of generating spin currents through thermal gradient [20], and spin pumping of generating spin currents through the coherent precession of magnetization [21], expand the application fields of spintronics, promoting the development of green energy in the new century. Today, in pursuing small-sized and high-performance information devices, Moore's Law has reached its limit [22], especially as the development of artificial intelligence requires enormous energy and computing power. Spintronic devices offer opportunities for further development and are expected to replace traditional semiconductor devices in a new technological revolution.

2.1.2 Spin current

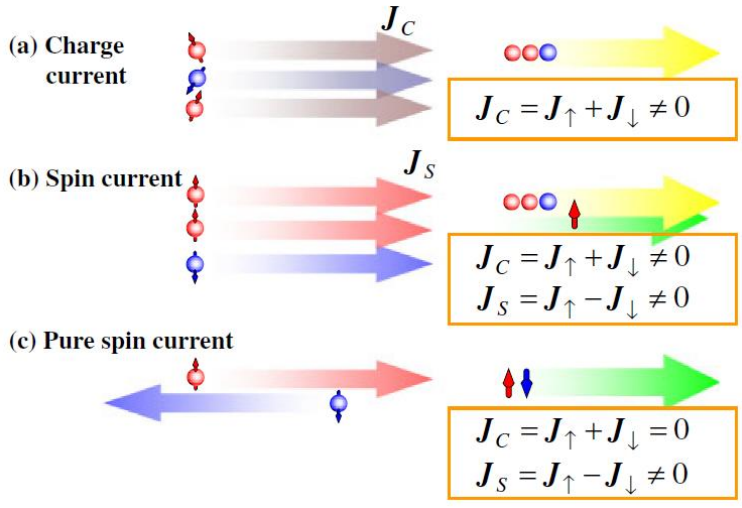

Fig. 2.2 Schematic diagram of (a) charge current, (b) spin current, and (c) pure spin current [23]. J_C represents the charge current density, J_S is the spin current density, $J_\uparrow$ and $J_\downarrow$ are spin up and spin down currents, respectively.

Understanding spin currents is the first step in exploring spintronics. Fig. 2.2 describes the difference between spin current and conventional charge current. Before the concept of spin was proposed, the widely accepted view was that the charge current is caused by the movement of charges [Fig. 2.2(a)]. However, if the spin of electrons is considered [Fig. 2.2(b)], when electrons with different spins (up or down) move in the same direction, the existing charge current density is $J_C = J_\uparrow + J_\downarrow$. But there is an additional part of spin current density $J_S = J_\uparrow - J_\downarrow$. When the motion direction for spin up and spin down electrons are exactly opposite [Fig. 2.2(c)], the net charge current becomes zero, and a pure spin current density remains with $J_S = J_\uparrow - J_\downarrow$. Pure spin current has almost no energy dissipation and has excellent potential in the post-Moore era.

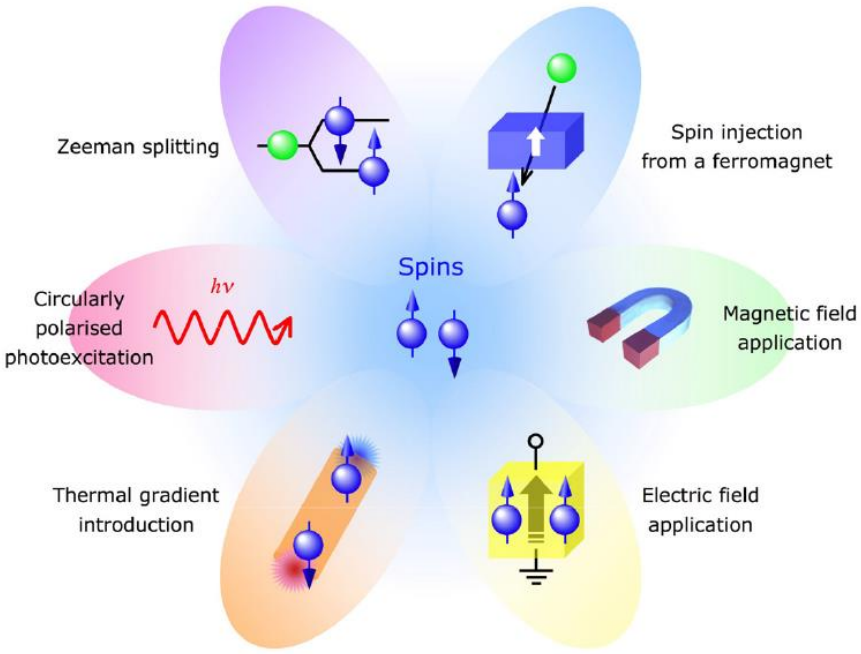

Fig. 2.3 Some methods to generate spin current [4].

After decades of exploration, researchers have found that spin currents can be generated through various methods. As shown in Fig. 2.3, spin current can usually be driven by an electric field, a magnetic field, or activated through spin injection from ferromagnets [24]. Zeeman splitting [25] and circularly polarized photo-excitation [26] are also commonly used to generate spin currents. Moreover, since the discovery of

spin Seebeck effect in 2008 [20], thermal gradient-induced spin current has been widely accepted and deeply explored. The spin current conversion efficiency (η) is defined as $\eta = J_S/J_C$ [27]. A higher efficiency implies lower energy dissipation. In theory, η of the ferromagnetism/non-magnetic material system can reach 100% if no dissipation exists, but it is only close to 20% in actual systems [28, 29], indicating some uncertain conditions can affect the conversion efficiency. For instance, the interface quality and spin Hall angle can greatly affect the spin current transport [30].

2.2 Phenomena related to spintronics

2.2.1 Spin-obit coupling

Spin-orbit coupling is the interaction between spin angular momentum and orbitals [31]. The discovery of SOC can be traced back to 1896 [32] when Zeeman proved the existence of SOC through spectral splitting phenomena. When electrons with momentum p move in a magnetic field B, the resulting Lorentz force can be expressed as:

$$F = -e\frac{B \times p}{m} \qquad (2-1)$$

Where e represents the electronic charge and m is the mass of the electron. Similarly, when an electric field E replaces B, the electric field will apply an equivalent magnetic field, expressed as:

$$B_E = -\frac{E \times p}{mc^2} \qquad (2-2)$$

Where c is the speed of light. Considering that electrons have a Zeeman energy of:

$$\triangle E = \mu_B \boldsymbol{\sigma} \cdot \boldsymbol{B} \qquad (2-3)$$

Where μ_B is Bohr magneton, and $\boldsymbol{\sigma}$ represents the Pauli spin matrix vector. Then, the SOC can be expressed by the following formula:

$$\widehat{H} = -\mu_B \frac{E \times p}{mc^2}\,\boldsymbol{\sigma} \qquad (2-4)$$

Due to the time-reversal symmetry of spin-orbit coupling, it is necessary to break this symmetry to realize the SOC. The discovery of SOC leads to many interesting spin

phenomena, such as induced polarization spin current [33] and spin precession [34]. As we will see soon, the spin Hall effect is strongly related to spin-obit coupling.

2.2.2 Spin Hall effect

The origin of the Hall effect can be traced back to 1879 [35]. As shown in Fig. 2.4(a), Edwin H. Hall accidentally found that when a conductor with current is subjected to a magnetic field perpendicular to the direction of current, the track of electron motion will deflect due to the Lorentz force, thus generating a potential difference. The phenomenon is called the Hall effect. Two years later, the anomalous Hall effect (AHE) was also discovered [36]. As shown in Fig. 2.4(b), it was found that when the conductor was replaced by a ferromagnetic material (e.g. Co or Ni), the resistance slope under low magnetic field became abnormal.

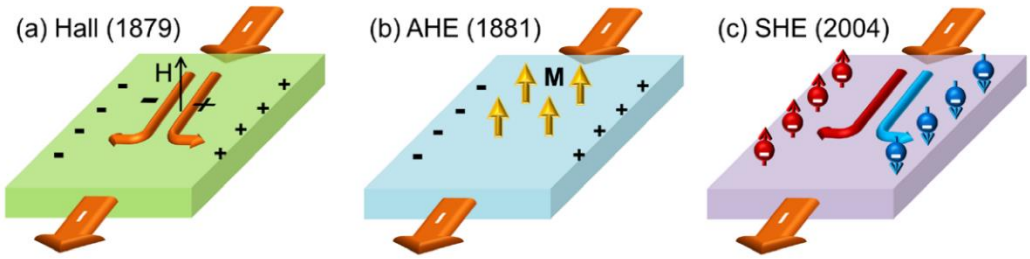

Fig. 2.4 Schematic diagram of (a) Hall effect, (b) anomalous Hall effect, and (c) spin Hall effect [37].

The concept of SHE is derived from the AHE. The external magnetic field is not a necessary condition for SHE generation. As shown in Fig. 2.4(c), when a charge current is applied to a material, carriers with two different spin directions (spin up and spin down) accumulate at the edge of the material and generate a spin current perpendicular to the charge current. The concept of SHE was initially proposed based on Mott scattering [38], but the first prediction of SHE was proposed in 1971 by Dyakonov and Perel in non-magnetic materials [39, 40]. It took over thirty years from the prediction to the observation of SHE, when Awschalom *et al*. measured the effect in semiconductor GaAs and InGaAs thin films through Kerr rotation (Fig. 2.5) [41].

AHE and SHE are inseparable from the spin-orbit coupling effect and are considered to share the same physical mechanisms. In traditional views, three mechanisms are widely discussed in explaining AHE and SHE: intrinsic deflection, side jump, and skew scattering [42, 43]. Fig. 2.6 shows the schematic diagram of the three mechanisms.

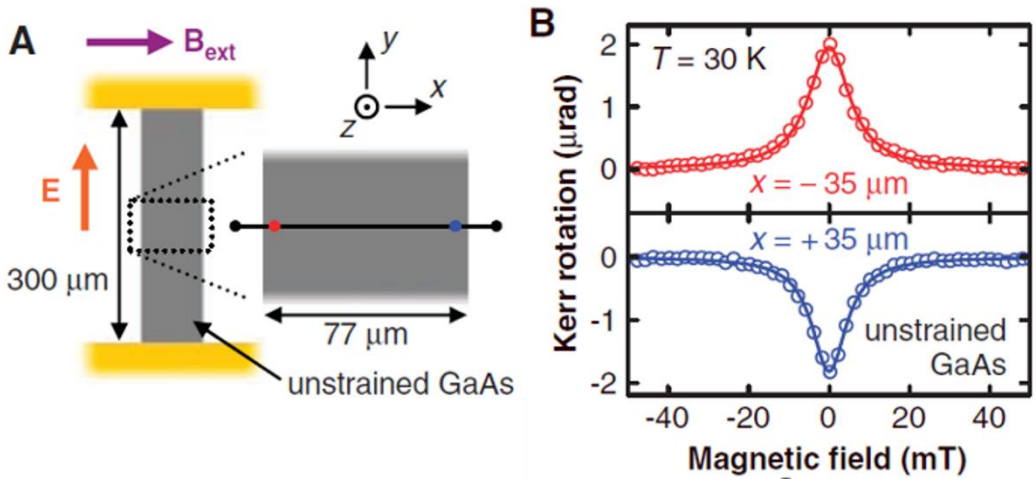

Fig. 2.5 (a) Schematic diagram of the measurement geometry of unstrained semiconductor GaAs sample using static Kerr rotation measurement. (b) Kerr rotation as a function of external magnetic field [41].

Intrinsic deflection in Fig. 2.6(a) was first proposed by Karplus and Luttinger in 1954 [44]. They proposed that the carrier motion in the band structure has an anomalous velocity proportional to the Berry curvature. This anomalous velocity causes the unequal number of spin-up and spin-down electrons, resulting in a net transverse current generated in an electric field, ultimately leading to the AHE. This also means that the band structure plays a crucial role in AHE and belongs to the intrinsic property of materials. In other words, AHE is an inevitable result of the action of SOC. According to the description, the anomalous Hall coefficient R_S would be proportional to the square of the resistance ρ^2 ($R_S \propto \rho^2$).

However, the concept of intrinsic deflection has not been entirely accepted. Smit refutes the theory because it is impossible to ignore the presence of impurities and defects, which inevitably lead to scattering. Based on this consideration, Smit proposed

the skew scattering [Fig. 2.6(b)] [45]. He believed that under the action of SOC, the scattering of electrons with different spin directions is asymmetric, and the deviation of electrons from their original motion direction would lead to the accumulation of transverse charges. According to the theory of skew scattering, it could be concluded that the Hall resistivity R_{xy} is proportional to the resistance ρ ($R_{xy} \propto \rho$).

The debate between Luttinger and Smit regarding the physical mechanism of AHE continued until 1970, when a new concept called the side jump was proposed by Berger [46]. As shown in Fig. 2.6(c), because the angle between the spin angular momentum S and the orbital angular momentum L would affect SOC, the scattered electrons generate a transverse jump Δy during motion, which leads to an accumulation of transverse charge. According to the side jump mechanism, the Hall resistivity R_{xy} is proportional to the square of the resistance ρ^2 ($R_{xy} \propto \rho^2$). It is worth noting that both side jump and skew scattering belong to external mechanisms, as both are caused by defect scattering.

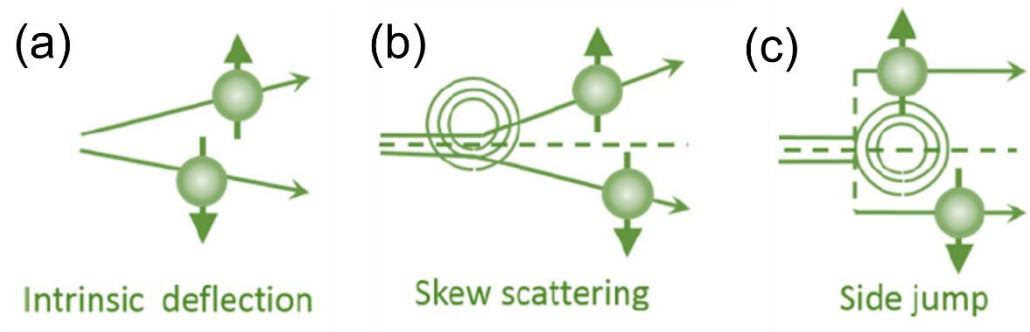

Fig. 2.6 Schematic diagram of (a) intrinsic deflection, (b) skew scattering, and (c) side jump [45].

2.2.3 Inverse spin Hall effect

To detect spin currents, researchers used optical methods to detect spin accumulation in semiconductors at the beginning. However, because the spin diffusion length of metals with strong SOC is ~10 nm, which is much smaller than that of semiconductors (~1 μm) [47], optical methods showed limitations on metal spin current

detection. After discovering the SHE, people began to use the ISHE to detect spin currents.

Fig. 2.7 compares the mechanisms of SHE and ISHE. ISHE is the process of converting spin current into charge current. In other words, the conversion between J_S and J_C is reversible. As mentioned above, a charge current in metal with strong SOC (like Pt) would generate a J_S perpendicular to the direction of the current J_C. Because the spin Hall angle α_{SHE} is the ratio of spin Hall conductivity σ_{xy} to charge conductivity σ_{xx}, expressed as:

$$\alpha_{SHE} = \frac{\sigma_{xy}}{\sigma_{xx}} \frac{e}{\hbar} \tag{2-5}$$

The spin current J_S generated by SHE is:

$$J_S = \alpha_{SHE} \frac{\hbar}{2e} J_C \times \sigma \tag{2-6}$$

where $\hbar$ represents Planck constant and σ is the spin polarization direction. ISHE refers to the charge flow perpendicular to the J_S generated within metals under the effect of SOC, expressed as:

$$J_C = \alpha_{SHE} \frac{2e}{\hbar} J_S \times \sigma \tag{2-7}$$

It can be noticed from the formula and above descriptions that both SHE and ISHE are not dependent on moments or external fields, but only on the strength of SOC.

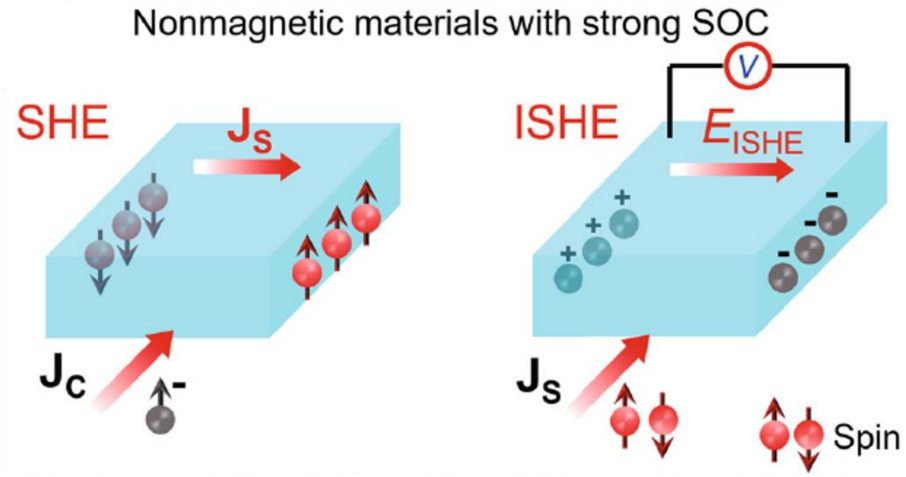

Fig. 2.7 Schematic diagram of SHE and ISHE [48].

2.2.4 Spin Hall magnetoresistance

As ISHE became a mature method for detecting spin currents, researchers started to use ISHE to study the magnetotransport characteristics of ferromagnet/normal metal heterostructures. Nakayma *et al*. proposed a non-equilibrium proximity effect called spin Hall magnetoresistance (SMR) in studying abnormal resistance signals in YIG/Pt [49].

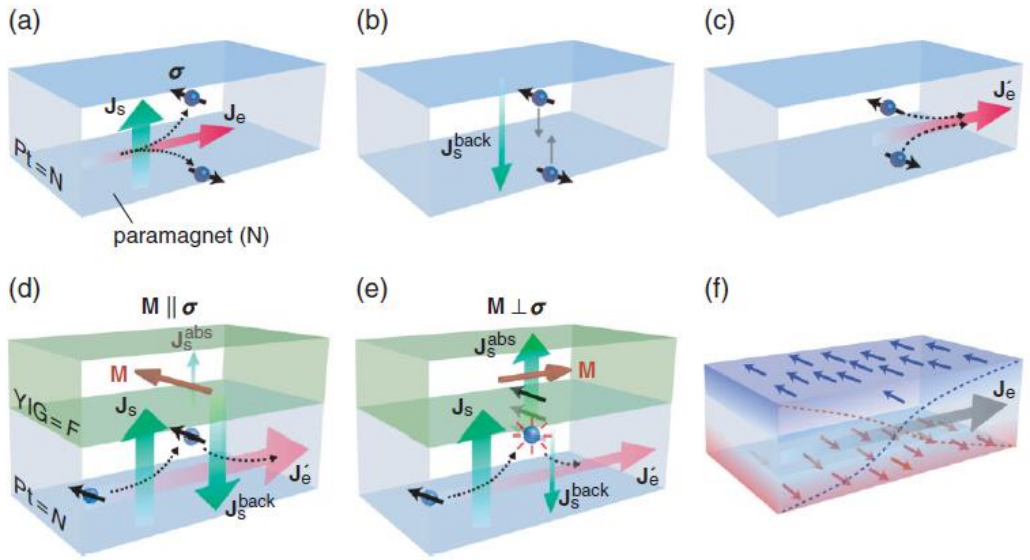

Fig. 2.8 (a-c) Schematic diagrams of SHE and ISHE in Pt with strong SOC. (d) and (e) show the relationship between spin current and magnetic moment direction. (f) illustrates the process of spin accumulation [49].

Fig. 2.8 shows the SMR theoretical model with YIG/Pt as an example. Because of the strong SOC in Pt, spin accumulation happens at the YIG/Pt interface. A spin current J_S would be induced perpendicular to the plane defined by spin polarization σ and charge current J_e [Fig. 2.8(a)]. Then, as shown in Fig. 2.8(b-c), part of J_S will be reflected inside Pt (called J_S^{back}) and transferred into charge current J_e' parallel to the original J_e direction through ISHE. When Pt is in contact with a ferromagnetic insulator like YIG, as shown in Fig. 2.8(d) and (e), although the electrons in Pt cannot enter the insulator YIG, the moment of YIG interact with the spin current at the Pt

interface, at which spin angular momentum transfer occurs at the YIG/Pt interface. At this point, two situations will occur. For one, the J_S is almost completely reflected by the YIG/Pt interface when $M \parallel \sigma$ [Fig. 2.8(d)], the resistance of Pt being the smallest. For another [Fig. 2.8(e)], when $M \perp \sigma$, most J_S will be absorbed at the interface, resulting in J_S^{back} being the smallest and the measured resistance of Pt being the largest. The interesting spin accumulation and abnormal resistance phenomena depend on the direction of magnetization and spin Hall angle, known as SMR. Hahn also verified the SMR in YIG/Ta heterostructure [50].

Chen *et al*. explained the non-equilibrium proximity phenomenon of SMR from a theoretical calculation perspective and proposed the concept of spin mixing conductance [51]. They calculated the longitudinal ρ_l and transverse resistances ρ_t as:

$$\rho_l = \rho + \triangle \rho_0 + \triangle \rho_1 \left(1 - m_y^2\right) \tag{2-8}$$

$$\rho_t = \triangle \rho_1 m_x m_y + \triangle \rho_2 m_z \tag{2-9}$$

where

$$\frac{\triangle \rho_0}{\rho} = -\theta_{SH}^2 \frac{2\lambda}{D_N} tanh \frac{D_N}{2\lambda} \tag{2-10}$$

$$\frac{\triangle \rho_1}{\rho} = \theta_{SH}^2 \frac{\lambda}{D_N} Re \frac{2\lambda G_{\uparrow\downarrow} tanh^2 \frac{D_N}{2\lambda}}{\sigma + 2\lambda G_{\uparrow\downarrow} coth \frac{D_N}{\lambda}} \tag{2-11}$$

$$\frac{\triangle \rho_2}{\rho} = -\theta_{SH}^2 \frac{\lambda}{D_N} Im \frac{2\lambda G_{\uparrow\downarrow} tanh^2 \frac{D_N}{2\lambda}}{\sigma + 2\lambda G_{\uparrow\downarrow} coth \frac{D_N}{\lambda}}. \tag{2-12}$$

Here ρ is the resistance of metal, λ is the spin diffusion length, θ_{SH} represents spin Hall angle, and D_N is the thickness of metal. $G_{\uparrow\downarrow}$ is the spin-mixing conductance of the interface, expressed as $G_{\uparrow\downarrow} = G_r + iG_i$. $\triangle \rho_1$ is mainly caused by the real part G_r, while $\triangle \rho_2$ is strongly related to the imaginary part G_i. The calculation of these parameters becomes an essential indicator for research on interface transport in FI/HM systems [52-55].

2.3 Rare earth iron garnets

One of the most commonly used materials in the study of spin Hall magnetotransport is the REIG. Next, I will focus on introducing REIG's structure and performance characteristics.

2.3.1 General structure and performance of REIG

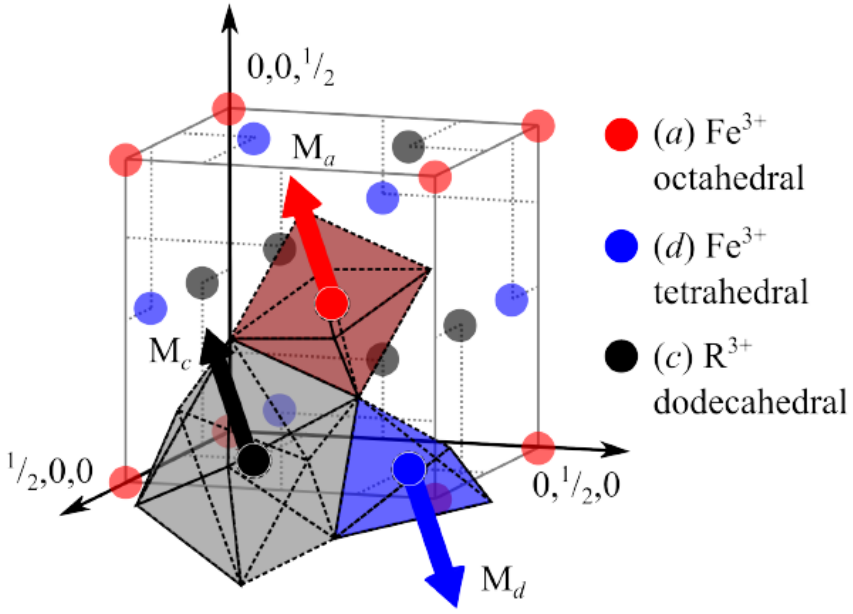

Fig. 2.9 Schematic diagram showing the 1/8 of a unit cell of $RE_3Fe_5O_{12}$ [56].

The first description of the garnet structure can be traced back to 1929 [57]. Detailed experimental and theoretical explorations have been conducted on the structure and magnetism of $RE_3Fe_5O_{12}$ [58-61]. Fig. 2.9 shows the REIG structure. The general REIG has cubic symmetry with $Ia\bar{3}d$ space group [61]. However, the internal structure of REIG is complex. The structure of $RE_3Fe_5O_{12}$ can also be written as $(C)_3(A)_2(D)_3O_{12}$, where C refers to RE elements and occupies the cation position (dodecahedral site). In contrast, A and D represent Fe elements occupying octahedral and tetrahedral sites, respectively. The atoms at the A, C, and D sites display a positive valence and are surrounded by O^{2-}. Table 2-1 summarizes the lattice constant of general REIGs and their typical applications.

REIGs show ferrimagnetism due to the antiparallel alignment between RE^{3+} and Fe^{3+} moment (Fig. 2.9). While the A-site and D-site Fe^{3+} are also aligned antiparallel to each other, the net moment of Fe^{3+} is dominated by D-site throughout the whole temperature range. The phenomenon of antiparallel alignment between sublattices leads to magnetization compensation in REIG, where the magnetization of three kinds of sublattices cancel out and the net moment becomes zero [62-65]. At above T_{comp}, the net moment is dominated by D-site Fe^{3+}. With the temperature decreasing, the stronger temperature-dependent moment of C-site RE^{3+} gradually dominates the net moment. Similar magnetization compensation phenomenon occurs in many REIGs. Fig. 2.10 compares the T_{comp} of different bulk REIG materials. The inflection point of the curve in Fig. 2.10 represents T_{comp}.

Table 2-1 List of REIGs, including chemical formula, bulk lattice constant, and applications [66]

Garnet	Chemical formula	Bulk lattice constant (Å)	Purpose
GGG	$Gd_3Ga_5O_{12}$	12.383	substrate
YAG	$Y_3Al_5O_{12}$	12.005	substrate
GSGG	$Gd_3Sc_2Ga_3O_{12}$	12.480	substrate
NGG	$Nd_3Ga_5O_{12}$	12.520	substrate
YIG	$Y_3Fe_5O_{12}$	12.376	film
TbIG	$Tb_3Fe_5O_{12}$	12.460	film
EuIG	$Eu_3Fe_5O_{12}$	12.500	film
GdIG	$Gd_3Fe_5O_{12}$	12.480	film
DyIG	$Dy_3Fe_5O_{12}$	12.440	film
TmIG	$Tm_3Fe_5O_{12}$	12.324	film

As shown in Fig. 2.10. GdIG has bulk T_{comp} (292 K) [67] close to 300 K, which is very suitable for studying signal regulation of spin-electronic devices at room

temperature. It is worth noting that YIG does not have T_{comp}, as Y^{3+} does not have a moment and Fe^{3+} dominates the net moment throughout the entire temperature range [61]. Similar REIGs without T_{comp} include EuIG [68].

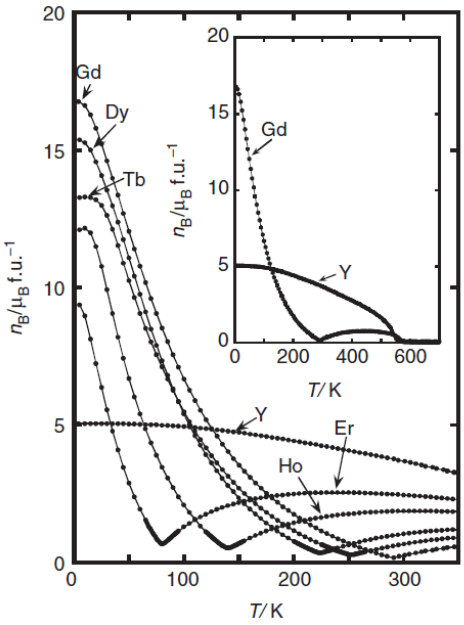

Fig. 2.10 The magnetization as a function of temperature for different REIG materials (RE: Er, Ho, Dy, Tb, Gd and Y) [69].

2.3.2 $Tb_3Fe_5O_{12}$

It is interesting to study spintronic devices composed of REIGs with T_{comp} and heavy metals with strong SOC, because some important information can be obtained from temperature-dependent R_{AHE}-H loops such as coercivity (H_c) and T_{comp}. In electrical measurements of REIGs/heavy metals, similar to the magnetic hysteresis loops, the maximum resistance value in the R_{AHE}-H plots can be obtained at zero field.

Here, I define the R_{AHE} value at zero magnetic field as R_{AHE}^0, when the external field sweeps from positive maximum to negative maximum. Obviously, the R_{AHE}^0 value can be positive or negative. The R_{AHE}^0-T plots can be extracted from the temperature-dependent R_{AHE}-H loops. If the R_{AHE}^0 value changes from positive to negative (or from negative to positive) in the R_{AHE}^0-T plots, it is considered as a R_{AHE} sign flip event (also called cross-over point).

Some REIGs with T_{comp} exhibit two R_{AHE}^{0} sign flips in R_{AHE}^{0}-T. One of such garnets is TbIG. TbIG has a Curie temperature of 568 K and T_{comp} of 246 K [61]. Early studies of TbIG focused on its magnetism and anisotropy when deposited on GGG substrates [70, 71]. Recently, two sign cross-overs of R_{AHE}^{0} were found in R_{AHE}^{0}-T plots of TbIG/Pt system [72, 73]. As shown in Fig. 2.11, the first sign flip happens around 230 K. As the temperature goes down, a second sign change happens, indicating the complexity of the spin transport of TbIG/Pt.

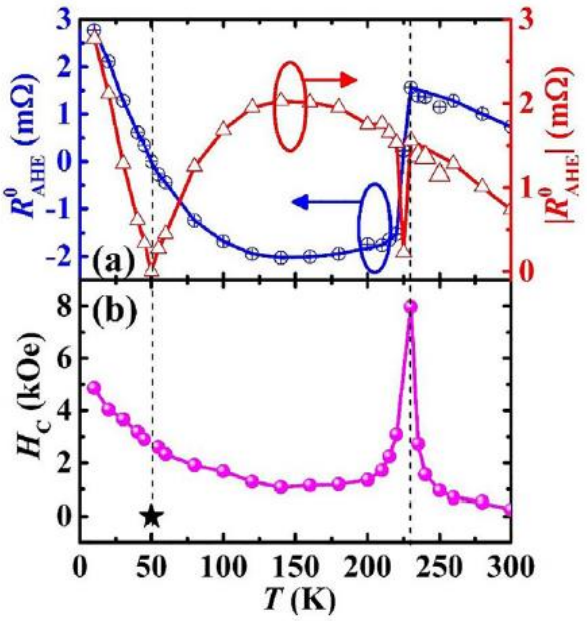

Fig. 2.11 Temperature-dependent anomalous Hall resistance R_{AHE}^{0} at zero field and coercivity H_c [72].

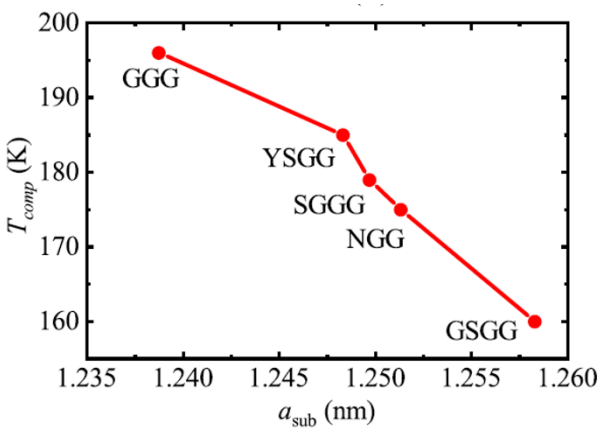

Fig. 2.12 Comparisons of T_{comp} with TbIG deposited on different substrates, including

$Gd_3Ga_5O_{12}$ (GGG), $Y_3Sc_2Ga_3O_{12}$ (YSGG) $Gd_{2.6}Ca_{0.4}Ga_{4.1}Mg_{0.25}Zr_{0.65}O_{12}$ (SGGG), $Nd_3Ga_5O_{12}$ (NGG), and $Gd_3Sc_2Ga_3O_{12}$ (GSGG) [74].

Besides, TbIG is often used to study the regulation of T_{comp}. As shown in Fig. 2.12, Li *et al*. [74] used different substrates to deposit TbIG of fixed thickness, achieving the control of T_{comp} from 196 K (GGG) to 160 K (GSGG), which is attributed to changes in epitaxial strains. Liang *et al*. [73] also realized the tunable T_{comp} by changing the thickness of the TbIG (Fig. 2.13). These routes of achieving T_{comp} regulation provide references for controllable logical operations in spintronic devices.

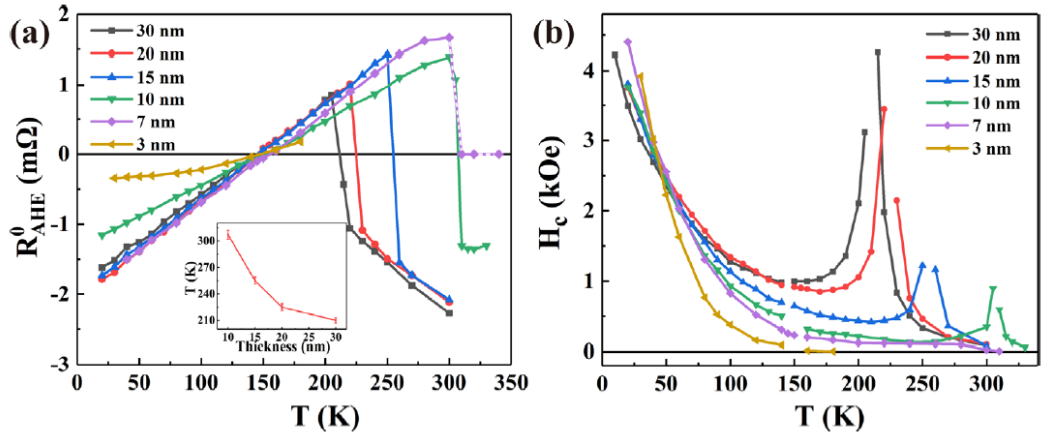

Fig. 2.13 Comparisons of temperature-dependent R^0_{AHE} (a) and H_c (b) for different thicknesses of TbIG [73].

2.3.3 $Eu_3Fe_5O_{12}$

Another important garnet involved in this study is EuIG. Eu^{3+} is a light rare earth element compared with others like Tb^{3+} and Gd^{3+}. Although Eu^{3+} shows antiparallel alignment with Fe^{3+} moment, EuIG does not have a compensation point, mainly because the ground state of Eu^{3+} is $J = 0$ according to the Hund's rule [68, 75], resulting in a negligible contribution of Eu^{3+} moment in EuIG. However, the second-order Zeeman effect may activate the magnetic contribution, especially at higher temperatures [76]. Therefore, EuIG can be used as a substitute material for YIG under

certain conditions, as both do not have T_{comp}.

However, EuIG exhibits some differences compared to YIG. For example, in the study of EuIG anisotropy by Rosenberg *et al*., it was found that EuIG shows an out-of-plane anisotropy when deposited on GGG (111) and (100) [77], while YIG shows an in-plane easy axis on the same substrates [78]. This difference in anisotropy provides choices for the design of multilayer films.

2.4 Magnetic proximity effect in Pt

Pt with strong SOC effect is widely used in the study of spin Hall magnetotransport [79-83]. As the energy band of Pt is approaching the Stoner criterion for itinerant ferromagnetism [84, 85], when Pt forms a heterostructure with ferromagnetic materials, it is easy to induce magnetic moments at a limited interface depth on the Pt side, i.e., Pt would be easily magnetized. The effect is called magnetic proximity effect (MPE).

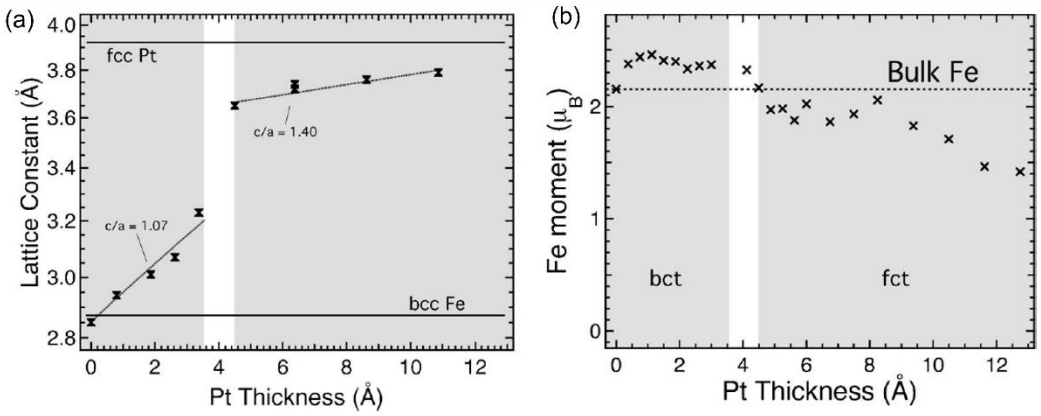

Fig. 2.14 (a) Plot of c-axis lattice constant of Fe/Pt as a function of Pt thickness. Crystalline phase was judged by c/a ratio. The white band represents the boundary of phase transition, and the solid horizontal lines represent bulk lattice constants of Pt and Fe. (b) Fe moment as a function of Pt thickness as measured by X-ray magnetic circular dichroism (XMCD) [86].

In earlier years, Antel *et al*. observed the MPE phenomenon in Pt using magneto-optic Kerr effect (MOKE) and XMCD [86]. In the Pt/Fe system, they found that the

varying thickness of Pt affected the crystal structure of Pt/Fe, resulting in a transition from body-centered tetragonal (bct) to face-centered tetragonal (fct) structure, which leads to variations in magnetic moments (Fig. 2.14). It was found that the moment of Fe with bct structure is about 10% higher than that of fct structure, and through MOKE measurements the Pt/Fe interface anisotropic changes was established. Huang *et al*. also found similar magnetic anisotropy originating from the interface in the Pt thickness-dependence study of YIG/Pt [87].

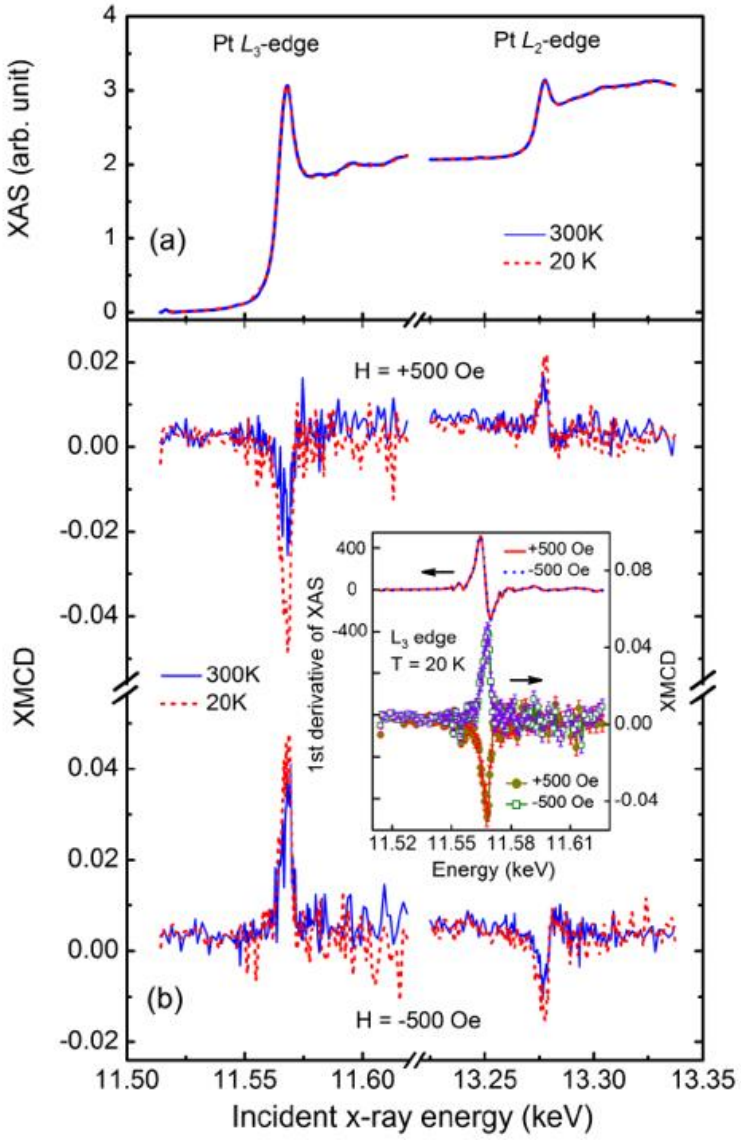

Fig. 2.15 (a) X-ray absorption spectra of Pt in YIG/Pt system. (b) Comparisons of XMCD at 20 K and 300 K for YIG/Pt system [88].

Lu *et al*. [88] directly confirmed the existence of MPE in Pt using XMCD, as shown in Fig. 2.15. They found that both L_2 and L_3 of Pt have moments and show temperature dependence. At low temperatures (20 K), the magnetic moment is stronger than at room temperature (300 K). Besides, the observation of AHE and magnetic anisotropy proves the potential of Pt properties modulation in these effects.

Recently, with the in-depth study of MPE in Pt, especially in the REIG/Pt system, people have become more aware of the importance of MPE in spin transport. For example, in the spin Seebeck effect study of YIG/Pt, Qu *et al*. [89] suggested that MPE can lead to the entanglement of multiple physical effects. Zhang *et al*. [80] found that in Py/Pt system, an increase in Pt moment leads to a decrease in spin Hall conductivity, and there is a substantial trade-off between the two, providing direction for the regulation of spin Hall transport.

2.5 Perpendicular Magnetic Anisotropy (PMA)

Many spin-related phenomena can only be observed through spintronic devices with perpendicular magnetic anisotropy, with the easy axis of magnetization being perpendicular to the plane of the magnetic films. For example, to achieve fast spin-orbit torque response switching with low current density, the easy axis of the magnetization needs to be normal to the sample's surface [90]. The determination of whether a magnetic material has PMA mainly depends on the energy density of anisotropy, also called the effective anisotropy energy density K_{eff} [91], which is expressed as:

$$K_{eff} = K_{strain} + K_{shape} + K_1. \qquad (2-13)$$

Here K_{strain} is the strain-induced anisotropy, K_{shape} represents the shape anisotropy and K_1 is magnetocrystalline anisotropy. K_1 is negative and usually can be neglected as it is much smaller than the other two terms [77, 92, 93]. K_{strain} is strongly related to the lattice mismatch between the substrate and the film. Taking GGG (111) substrate as an example, K_{strain} can be calculated by:

$$K_{strain} = -\frac{3}{2}\lambda_{111}\sigma_{\parallel}, \qquad (2-14)$$

where λ_{111} is the magnetostriction constant and usually shows a negative value in PMA material. But there are a few exceptions, such as the positive λ_{111} of GGG/TbIG with PMA [94]. $\sigma_{\parallel}$ refers to the in-plane stress and express as:

$$\sigma_{\parallel} = \frac{Y}{1-\nu}\frac{A_{film}-B_{sub}}{B_{sub}}, \qquad (2-15)$$

where Y and ν represent elastic modulus and Poisson's ratio, respectively. A_{film} is the lattice constant of film and B_{sub} is substrate lattice constant (c.f. Table 2-1). K_{shape} is related to the saturation magnetization M_s of REIGs, and can be calculated as:

$$K_{shape} = 2\pi M_s^2 \qquad (2-16)$$

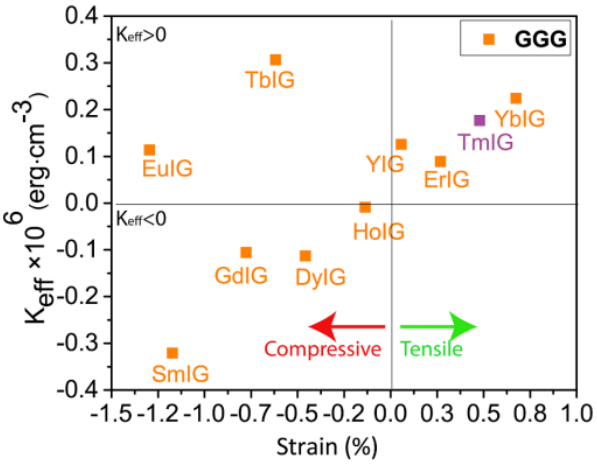

Fig. 2.16 Calculated K_{eff} and stress-state for some popular REIG films when deposited on GGG substrate [66].

According to the formulae presented above, large and negative K_{eff} is desired for realizing PMA. As shown in Fig. 2.16. Zanjani *et al*. summarized K_{eff} of some common REIGs according to theoretical lattice constants [66]. Controlling anisotropy by changing the substrate lattice constant is a direct and effective approach. As shown in Fig. 2.17, the difference in substrate lattice constants can lead to significant changes in the strain of HoIG film epitaxial growth, thereby affecting magnetic anisotropy [95].

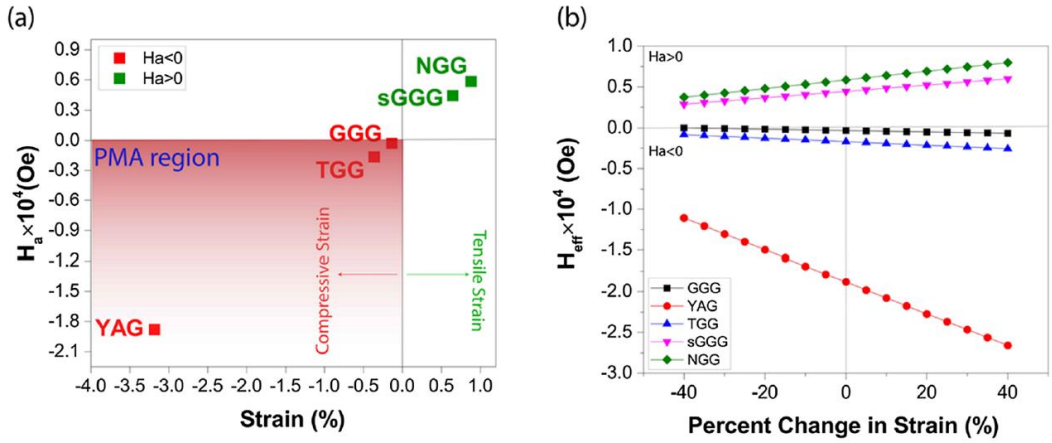

Fig. 2. 17 Comparisons of anisotropy field (a) and effective anisotropy energy density (b) for HoIG deposited on different substrates [95].

There are many studies on achieving PMA in REIG. For example, YIG typically displays an in-plane easy axis because of the large K_{shape} [96]. However, YIG can also achieve PMA through doping and substrate replacement [91, 97, 98]. For TbIG, many studies have confirmed that it displays PMA on GGG(111) [99, 100], but it displays an in-plane easy axis on SGGG (Fig. 2.18) [77]. These demonstrate the tunability of PMA. Moreover, the PMA is also suitable for studying the electrical properties of REIG/HM systems, such as the study of AHE phenomena, creating more possibilities for the study of spin magnetotransport.

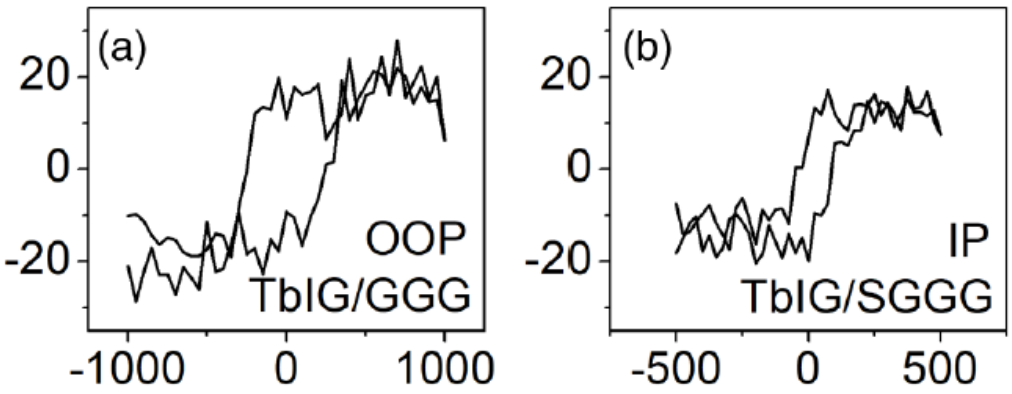

Fig. 2. 18 The easy-axis VSM of TbIG when deposited on (a) GGG and (b) SGGG [77].

It should be noted that K_{eff} value can only be used as a reference for judging

PMA, as the anisotropy of some REIG does not fully follow formula (2-13) [101, 102]. There are many other factors to consider, such as the exchange coupling energy, roughness of the substrate, film deposition rate and temperature, etc., which can influence the final anisotropy state. This is also a fascinating aspect of PMA regulation.

2.6 Summary

In summary, this Chapter provided a brief introduction to the basic principles of spintronics and related phenomena, as well as an understanding of the structural and magnetic characteristics of REIGs. It also discussed the importance of PMA structures and summarized the progress of research on spin magnetotransport in REIG/HM devices. The literature review above provided a deeper understanding of the mechanism of spin transport and effectively guides the experimental design in later Chapters.

References for Chapter 2

[1] I. Duck, W. Pauli, E. Sudarshan, *Pauli and the spin-statistics theorem*, (World Scientific, Singapore, 1997).

[2] B. Thaller, *The Dirac Equation*, (Springer, Berlin, 1992).

[3] S.D. Bader, S.S.P. Parkin, Spintronics, Annu. Rev. Conden. Matter phys. 1 (2010) 71-88.

[4] A. Hirohata, K. Yamada, Y. Nakatani, I.-L. Prejbeanu, B. Diény, P. Pirro, B. Hillebrands, Review on spintronics: Principles and device applications, J. Magn. Magn. Mater. 509 (2020) 166711.

[5] M.N. Baibich, J.M. Broto, A. Fert, F. Nguyen Van Dau, F. Petroff, P. Etienne, G. Creuzet, A. Friederich, J. Chazelas, Giant magnetoresistance of (001)Fe/(001)Cr magnetic superlattices, Phys. Rev. Lett. 61 (1988) 2472-2475.

[6] G. Binasch, P. Grunberg, F. Saurenbach, W. Zinn, Enhanced magnetoresistance in layered magnetic structures with antiferromagnetic interlayer exchange, Phys. Rev. B Condens. Matter 39 (1989) 4828-4830.

[7] T. Miyazaki, N. Tezuka, Giant magnetic tunneling effect in Fe/Al_2O_3/Fe junction, J. Magn. Magn. Mater. 139 (1995) L231-L234.

[8] W.H. Butler, X.G. Zhang, T.C. Schulthess, J.M. MacLaren, Spin-dependent tunneling conductance of Fe|MgO|Fe sandwiches, Phys. Rev. B 63 (2001) 054416.

[9] J. Mathon, A. Umerski, Theory of tunneling magnetoresistance of an epitaxial Fe/MgO/Fe(001) junction, Phys. Rev. B 63 (2001) 220403.

[10] S. Yuasa, T. Nagahama, A. Fukushima, Y. Suzuki, K. Ando, Giant room-temperature magnetoresistance in single-crystal Fe/MgO/Fe magnetic tunnel junctions, Nat. Mater. 3 (2004) 868-871.

[11] S.S. Parkin, C. Kaiser, A. Panchula, P.M. Rice, B. Hughes, M. Samant, S.H. Yang, Giant tunnelling magnetoresistance at room temperature with MgO (100) tunnel barriers, Nat. Mater. 3 (2004) 862-867.

[12] T. Scheike, Z. Wen, H. Sukegawa, S. Mitani, 631% room temperature tunnel

magnetoresistance with large oscillation effect in CoFe/MgO/CoFe(001) junctions, Appl. Phys. Lett. 122 (2023) 112404.

[13] J.C. Slonczewski, Current-driven excitation of magnetic multilayers. J. Magn. Magn. Mater. 159 (1996) L1-L7.

[14] L. Berger, Emission of spin waves by a magnetic multilayer traversed by a current. Phys. Rev. B 54 (1996) 9353-9358.

[15] W. Kang, Z. Wang, H. Zhang, S. Li, Y. Zhang, W. Zhao, Advanced low power spintronic memories beyond STT-MRAM, Proceedings of the Great Lakes Symposium on VLSI (2017) 299-304.

[16] Z. Sun, W. Wu, H. Li, Cross-layer racetrack memory design for ultra high density and low power consumption. In Proceedings of the 50th Annual Design Automation Conference (2013) 1-6.

[17] Y.K. Kato, R.C. Myers, AC. Gossard, D.D. Awschalom, Observation of the spin Hall effect in semiconductors. science 306 (2004) 1910-1913.

[18] K.S. Novoselov, A.K. Geim, S.V. Morozov, D.E. Jiang, Y. Zhang, S.V. Dubonos, I.V. Grigorieva, AA. Firsov, Electric field effect in atomically thin carbon films. Science 306 (2004) 666-669.

[19] X.-L. Qi, S.-C. Zhang, The quantum spin Hall effect and topological insulators, Phys. Today 63 (2010) 33-38.

[20] K. Uchida, S. Takahashi, K. Harii, J. Ieda, W. Koshibae, K. Ando, S. Maekawa, E. Saitoh, Observation of the spin Seebeck effect, Nature 455 (2008) 778-781.

[21] M.V. Costache, M. Sladkov, S.M. Watts, C.H. van der Wal, B.J. van Wees, Electrical detection of spin pumping due to the precessing magnetization of a single ferromagnet, Phys. Rev. Lett. 97 (2006) 216603.

[22] W.M. Holt, Moore's law: A path going forward, IEEE International Solid-State Circuits Conference (ISSCC) (2016) 8-13.

[23] Y. Ando, Spintronics technology and device development, Jpn. J. Appl. Phys. 54 (2015) 070101.

[24] P.R. Hammar, B.R. Bennett, M.J. Yang, M. Johnson, Observation of spin injection

at a ferromagnet-semiconductor interface. Phys. Rev. Lett. 83 (1999), 20375.

[25] J. Linder, T. Yokoyama, Y. Tanaka, A. Sudbø, Strongly spin-polarized current generated in a Zeeman-split unconventional superconductor, Phys. Rev. B 78 (2008) 014516.

[26] J. Rioux, G. Burkard, Photoinduced pure spin-current injection in graphene with Rashba spin-orbit interaction, Phys. Rev. B 90 (2014) 035210.

[27] E. Lesne, Y. Fu, S. Oyarzun, J.C. Rojas-Sanchez, D.C. Vaz, H. Naganuma, G. Sicoli, J.P. Attane, M. Jamet, E. Jacquet, J.M. George, A. Barthelemy, H. Jaffres, A. Fert, M. Bibes, L. Vila, Highly efficient and tunable spin-to-charge conversion through Rashba coupling at oxide interfaces, Nat. Mater. 15 (2016) 1261-1266.

[28] M.-H. Nguyen, M. Zhao, D.C. Ralph, R.A. Buhrman, Enhanced spin Hall torque efficiency in $Pt_{100-x}Al_x$ and $Pt_{100-x}Hf_x$ alloys arising from the intrinsic spin Hall effect, Appl. Phys. Lett. 108 (2016) 242407.

[29] T. Tashiro, S. Matsuura, A. Nomura, S. Watanabe, K. Kang, H. Sirringhaus, K. Ando, Spin-current emission governed by nonlinear spin dynamics, Sci. Rep. 5 (2015) 15158.

[30] L. Jin, K. Jia, D. Zhang, B. Liu, H. Meng, X. Tang, Z. Zhong, H. Zhang, Effect of interfacial roughness spin scattering on the spin current transport in YIG/NiO/Pt heterostructures, ACS Appl. Mater. Interfaces 11 (2019) 35458-35467.

[31] J.B. Goodenough, Spin-orbit-coupling effects in transition-metal compounds, Phys. Rev. 171 (1968) 466-479.

[32] L.I. Schiff, H. Snyder, Theory of the quadratic Zeeman effect, Phys. Rev. 55 (1939) 59-63.

[33] Q.-f. Sun, X.C. Xie, Spontaneous spin-polarized current in a nonuniform Rashba interaction system, Phys. Rev. B 71 (2005) 155321.

[34] S. Datta, B. Das, Electronic analog of the electro-optic modulator, Appl. Phys. Lett. 56 (1990) 665-667.

[35] E.H. Hall, On a new action of the magnet on electric currents. Am. J. Math. 2 (1879) 287-292.

[36] E.H. Hall, On the “Rotational coefficient” in nickel and cobalt, Lond. Edinb. Phil. Mag. J. Sci. 12 (2010) 157-172.

[37] C.Z. Chang, M. Li, Quantum anomalous Hall effect in time-reversal-symmetry breaking topological insulators, J. Phys. Condens. Matter. 28 (2016) 123002.

[38] J. Sinova, S.O. Valenzuela, J. Wunderlich, C.H. Back, T. Jungwirth, Spin Hall effects, Rev. Mod. Phys. 87 (2015) 1213-1260.

[39] M.I. Dyakonov, V.I. Perel, Current-induced spin orientation of electrons in semiconductors. Phys. Lett. A 35 (1971) 459-460.

[40] M.I. Dyakonov, Possibility of orienting electron spins with current. JETP Lett. USSR 13 (1971) 467-469.

[41] Y.K. Kato, R.C. Myers, A.C. Gossard, D.D. Awschalom, Observation of the spin Hall effect in semiconductors, Science 306 (2004) 1910-1913.

[42] L.J. Zhu, J.H. Zhao, Electrical transport of perpendicularly magnetized $L1_0$-MnGa and MnAl Films, Spin 07 (2017) 1730001.

[43] N. Nagaosa, J. Sinova, S. Onoda, A.H. MacDonald, N.P. Ong, Anomalous Hall effect, Rev. Mod. Phys. 82 (2010) 1539-1592.

[44] R. Karplus, J.M. Luttinger, Hall Effect in Ferromagnetics, Phys. Rev. 95 (1954) 1154-1160.

[45] J. Smit, The spontaneous Hall effect in ferromagnetics I. Physica, 21 (1955) 877-887.

[46] L. Berger, Side-jump mechanism for the Hall effect of ferromagnets, Phys. Rev. B 2 (1970) 4559-4566.

[47] S.D. Ganichev, V.V. Bel’kov, S.A. Tarasenko, S.N. Danilov, S. Giglberger, C. Hoffmann, E.L. Ivchenko, D. Weiss, W. Wegscheider, C. Gerl, D. Schuh, J. Stahl, J. De Boeck, G. Borghs, W. Prettl, Zero-bias spin separation, Nature Phys. 2 (2006) 609-613.

[48] P. Wang, Z. Feng, Y. Yang, D. Zhang, Q. Liu, Z. Xu, Z. Jia, Y. Wu, G. Yu, X. Xu, Y. Jiang, Inverse orbital Hall effect and orbitronic terahertz emission observed in the materials with weak spin-orbit coupling, npj Quantum Mater. 8 (2023) 28-33.

[49] H. Nakayama, M. Althammer, Y.T. Chen, K. Uchida, Y. Kajiwara, D. Kikuchi, T. Ohtani, S. Geprags, M. Opel, S. Takahashi, R. Gross, G.E. Bauer, S.T. Goennenwein, E. Saitoh, Spin Hall magnetoresistance induced by a nonequilibrium proximity effect, Phys. Rev. Lett. 110 (2013) 206601.

[50] C. Hahn, G. de Loubens, O. Klein, M. Viret, V.V. Naletov, J. Ben Youssef, Comparative measurements of inverse spin Hall effects and magnetoresistance in YIG/Pt and YIG/Ta, Phys. Rev. B 87 (2013) 174417.

[51] Y.-T. Chen, S. Takahashi, H. Nakayama, M. Althammer, S.T.B. Goennenwein, E. Saitoh, G.E.W. Bauer, Theory of spin Hall magnetoresistance, Phys. Rev. B 87 (2013) 144411.

[52] J.J. Bauer, E.R. Rosenberg, C.A. Ross, Perpendicular magnetic anisotropy and spin mixing conductance in polycrystalline europium iron garnet thin films, Appl. Phys. Lett. 114 (2019) 052403.

[53] Z. Qiu, K. Ando, K. Uchida, Y. Kajiwara, R. Takahashi, H. Nakayama, T. An, Y. Fujikawa, E. Saitoh, Spin mixing conductance at a well-controlled platinum/yttrium iron garnet interface, Appl. Phys. Lett. 103 (2013) 092404.

[54] L. Wang, Z. Lu, J. Xue, P. Shi, Y. Tian, Y. Chen, S. Yan, L. Bai, M. Harder, Electrical control of spin-mixing conductance in a $Y_3Fe_5O_{12}$/platinum bilayer, Phys. Rev. Appl. 11 (2019) 044060.

[55] M. Weiler, M. Althammer, M. Schreier, J. Lotze, M. Pernpeintner, S. Meyer, H. Huebl, R. Gross, A. Kamra, J. Xiao, Y.T. Chen, H. Jiao, G.E. Bauer, S.T. Goennenwein, Experimental test of the spin mixing interface conductivity concept, Phys. Rev. Lett. 111 (2013) 176601.

[56] A.B. Cahaya, Enhancement of thermal spin pumping by orbital angular momentum of rare earth iron garnet, J. Magn. Magn. Mater. 553 (2022) 169248.

[57] G. Menzer, XX. Die kristallstruktur der granate, Zeitschrift für Kristallographie-Crystalline Mater. 69 (1929) 300-396.

[58] S. Becker, Z. Ren, F. Fuhrmann, A. Ross, S. Lord, S. Ding, R. Wu, J. Yang, J. Miao, M. Kläui, G. Jakob, Magnetic coupling in $Y_3Fe_5O_{12}$/$Gd_3Fe_5O_{12}$

heterostructures, Phys. Rev. Appl. 16 (2021) 014047.

[59] S.M. Benford, G.V. Brown, T-S diagram for gadolinium near the Curie temperature, J. Appl. Phys. 52 (1981) 2110-2112.

[60] S. Iida, Magnetostriction constants of rare earth iron garnets, J. Phys. Soc. Jpn. 22 (1967) 1201-1209.

[61] E. P. Wohlfarth, (Ed). *Handbook of magnetic materials* (Vol. 2), (North-Holland, Amsterdam,1980).

[62] S. Geller, J.P. Remeika, R.C. Sherwood, H.J. Williams, G.P. Espinosa, Magnetic study of the heavier rare-earth iron garnets, Phys. Rev. 137 (1965) A1034-A1038.

[63] J.S. McCloy, B. Walsh, Sublattice Magnetic Relaxation in Rare Earth Iron Garnets, IEEE Trans. Magn. 49 (2013) 4253-4256.

[64] S. Geprags, A. Kehlberger, F.D. Coletta, Z. Qiu, E.J. Guo, T. Schulz, C. Mix, S. Meyer, A. Kamra, M. Althammer, H. Huebl, G. Jakob, Y. Ohnuma, H. Adachi, J. Barker, S. Maekawa, G.E.W. Bauer, E. Saitoh, R. Gross, S.T.B. Goennenwein, M. Klaui, Origin of the spin Seebeck effect in compensated ferrimagnets, Nat Commun. 7 (2016) 10452.

[65] M. Lahoubi, A. Bouguerra, A. Kihal, G. Fillion, Magnetic phase diagrams of dysprosium iron garnet (DyIG) in high dc fields, J. Alloy. Compd. 275 (1998) 598-601.

[66] S. Mokarian Zanjani, M.C. Onbaşlı, Predicting new iron garnet thin films with perpendicular magnetic anisotropy, J. Magn. Magn. Mater. 499 (2020) 166108.

[67] P.J. Flanders, Anisotropic properties measured as a function of temperature, J. Appl. Phys. 42 (1971) 1635-1636.

[68] W.P. Wolf, J.H. Van Vleck, Magnetism of Europium Garnet, Phys. Rev. 118 (1960) 1490-1492.

[69] M. Uemura, T. Yamagishi, S. Ebisu, S. Chikazawa, S. Nagata, A double peak of the coercive force near the compensation temperature in the rare earth iron garnets, Philos. Mag. 88 (2008) 209-228.

[70] D. Rodić, Z. Tomkowicz, L. Novaković, A. Szytula, M.L. Napijalo, The initial

magnetic susceptibilities of $Gd_3Fe_5O_{12}$ and $Tb_3Fe_5O_{12}$ in the compensation point region, Solid State Commun. 73 (1990) 243-246.

[71] M. Lahoubi, Magnetic study of the low temperature anomalies in the magnetodielectric terbium iron garnet, Phys. B: Condensed Matter. 536 (2018) 96-101.

[72] Y.K. Liu, H.F. Wong, K.K. Lam, K.H. Chan, C.L. Mak, C.W. Leung, Anomalous Hall effect in Pt/$Tb_3Fe_5O_{12}$ heterostructure: Effect of compensation point, J. Magn. Magn. Mater. 468 (2018) 235-240.

[73] J.M. Liang, X.W. Zhao, Y.K. Liu, P.G. Li, S.M. Ng, H.F. Wong, W.F. Cheng, Y. Zhou, J.Y. Dai, C.L. Mak, C.W. Leung, The thickness effect on the compensation temperature of rare-earth garnet thin films, Appl. Phys. Lett. 122 (2023) 242401.

[74] Y. Li, X. Yang, H. Bai, M. Wang, D. Cheng, C. Song, Z. Yuan, Y. Liu, Z. Shi, Strain-tunable magnetic compensation temperature of epitaxial $Tb_3Fe_5O_{12}$ thin films, Phys. Rev. B 108 (2023) 184403.

[75] S. Geller, H.J. Williams, R.C. Sherwood, J.P. Remeika, G.P. Espinosa, Magnetic study of the lighter rare-earth ions in the iron garnets, Phys. Rev. 131 (1963) 1080-1082.

[76] V.H. Ortiz, B. Arkook, J. Li, M. Aldosary, M. Biggerstaff, W. Yuan, C. Warren, Y. Kodera, J.E. Garay, I. Barsukov, J. Shi, First- and second-order magnetic anisotropy and damping of europium iron garnet under high strain, Phys. Rev. Mater. 5 (2021) 124414.

[77] E.R. Rosenberg, L. Beran, C.O. Avci, C. Zeledon, B. Song, C. Gonzalez-Fuentes, J. Mendil, P. Gambardella, M. Veis, C. Garcia, G.S.D. Beach, C.A. Ross, Magnetism and spin transport in rare-earth-rich epitaxial terbium and europium iron garnet films, Phys. Rev. Mater. 2 (2018) 094405.

[78] Y. Wu, Z. Xu, J. Chen, X. Xu, J. Miao, Y. Jiang, The anisotropy of spin Hall magnetoresistance in Pt/YIG structures, Appl. Phys. A 127 (2021) 1-8.

[79] L. Ma, H.A. Zhou, L. Wang, X.L. Fan, W.J. Fan, D.S. Xue, K. Xia, Z. Wang, R.Q. Wu, G.Y. Guo, L. Sun, X. Wang, X.M. Cheng, S.M. Zhou, Spin orbit coupling

controlled spin pumping and spin Hall magnetoresistance effects, Adv. Electron. Mater. 2 (2016) 1600112.

[80] W. Zhang, M.B. Jungfleisch, W. Jiang, Y. Liu, J.E. Pearson, S.G.E.t. Velthuis, A. Hoffmann, F. Freimuth, Y. Mokrousov, Reduced spin-Hall effects from magnetic proximity, Phys. Rev. B 91 (2015) 115316.

[81] L. Mihalceanu, S. Keller, J. Greser, D. Karfaridis, K. Simeonidis, G. Vourlias, T. Kehagias, A. Conca, B. Hillebrands, E.T. Papaioannou, Spin-pumping through a varying-thickness MgO interlayer in Fe/Pt system, Appl. Phys. Lett. 110 (2017) 252406.

[82] L. Zhu, D.C. Ralph, R.A. Buhrman, Maximizing spin-orbit torque generated by the spin Hall effect of Pt, Appl. Phys. Rev. 8 (2021) 031308.

[83] W. Amamou, I.V. Pinchuk, A.H. Trout, R.E.A. Williams, N. Antolin, A. Goad, D.J. O'Hara, A.S. Ahmed, W. Windl, D.W. McComb, R.K. Kawakami, Magnetic proximity effect in Pt/$CoFe_2O_4$ bilayers, Phys. Rev. Mater. 2 (2018) 011401(R).

[84] M.M. Sigalas, D.A. Papaconstantopoulos, Calculations of the total energy, electron-phonon interaction, and Stoner parameter for metals, Phys. Rev. B Condens. Matter. 50 (1994) 7255-7261.

[85] S. Shimizu, K.S. Takahashi, T. Hatano, M. Kawasaki, Y. Tokura, Y. Iwasa, Electrically tunable anomalous Hall effect in Pt thin films, Phys. Rev. Lett. 111 (2013) 216803.

[86] W.J. Antel, Jr., M.M. Schwickert, T. Lin, W.L. O'Brien, G.R. Harp, Induced ferromagnetism and anisotropy of Pt layers in Fe/Pt (001) multilayers, Phys. Rev. B 60 (1999) 12933.

[87] S.Y. Huang, W.G. Wang, S.F. Lee, J. Kwo, C.L. Chien, Intrinsic spin-dependent thermal transport, Phys. Rev. Lett. 107 (2011) 216604.

[88] Y.M. Lu, Y. Choi, C.M. Ortega, X.M. Cheng, J.W. Cai, S.Y. Huang, L. Sun, C.L. Chien, Pt magnetic polarization on $Y_3Fe_5O_{12}$ and magnetotransport characteristics, Phys. Rev. Lett. 110 (2013) 147207.

[89] D. Qu, S.Y. Huang, J. Hu, R. Wu, C.L. Chien, Intrinsic spin Seebeck effect in

Au/YIG, Phys. Rev. Lett. 110 (2013) 067206.

[90] K. Garello, C.O. Avci, I.M. Miron, M. Baumgartner, A. Ghosh, S. Auffret, O. Boulle, G. Gaudin, P. Gambardella, Ultrafast magnetization switching by spin-orbit torques, Appl. Phys. Lett. 105 (2014) 212402.

[91] J. Fu, M. Hua, X. Wen, M. Xue, S. Ding, M. Wang, P. Yu, S. Liu, J. Han, C. Wang, H. Du, Y. Yang, J. Yang, Epitaxial growth of $Y_3Fe_5O_{12}$ thin films with perpendicular magnetic anisotropy, Appl. Phys. Lett. 110 (2017) 202403.

[92] M. Kubota, K. Shibuya, Y. Tokunaga, F. Kagawa, A. Tsukazaki, Y. Tokura, M. Kawasaki, Systematic control of stress-induced anisotropy in pseudomorphic iron garnet thin films, J. Magn. Magn. Mater. 339 (2013) 63-70.

[93] H. Wang, C. Du, P.C. Hammel, F. Yang, Strain-tunable magnetocrystalline anisotropy in epitaxial $Y_3Fe_5O_{12}$ thin films, Phys. Rev. B 89 (2014) 134404.

[94] M. Kubota, A. Tsukazaki, F. Kagawa, K. Shibuya, Y. Tokunaga, M. Kawasaki, Y. Tokura, Stress-induced perpendicular magnetization in epitaxial iron garnet thin films, Appl. Phys. Express 5 (2012) 103002.

[95] S.M. Zanjani, M.C. Onbasli, Thin film rare earth iron garnets with perpendicular magnetic anisotropy for spintronic applications, AIP Adv. 9 (2019) 035024.

[96] M.C. Onbasli, A. Kehlberger, D.H. Kim, G. Jakob, M. Kläui, A.V. Chumak, B. Hillebrands, C.A. Ross, Pulsed laser deposition of epitaxial yttrium iron garnet films with low Gilbert damping and bulk-like magnetization, APL Mater. 2 (2014) 106102.

[97] Y. Lin, L. Jin, H. Zhang, Z. Zhong, Q. Yang, Y. Rao, M. Li, Bi-YIG ferrimagnetic insulator nanometer films with large perpendicular magnetic anisotropy and narrow ferromagnetic resonance linewidth, J. Magn. Magn. Mater. 496 (2020) 165886.

[98] Q.B. Liu, K.K. Meng, Z.D. Xu, T. Zhu, X.G. Xu, J. Miao, Y. Jiang, Unusual anomalous Hall effect in perpendicularly magnetized YIG films with a small Gilbert damping constant, Phys. Rev. B 101 (2020) 174431.

[99] V.H. Ortiz, M. Aldosary, J. Li, Y. Xu, M.I. Lohmann, P. Sellappan, Y. Kodera,

J.E. Garay, J. Shi, Systematic control of strain-induced perpendicular magnetic anisotropy in epitaxial europium and terbium iron garnet thin films, APL Mater. 6 (2018) 121113.

[100] H. Chen, D. Cheng, H. Yang, D. Wang, S. Zhou, Z. Shi, X. Qiu, Magnetization switching induced by magnetic field and electric current in perpendicular TbIG/Pt bilayers, Appl. Phys. Lett. 116 (2020) 112401.

[101] N. Kumar, N.G. Kim, Y.A. Park, N. Hur, J.H. Jung, K.J. Han, K.J. Yee, Epitaxial growth of terbium iron garnet thin films with out-of-plane axis of magnetization, Thin Solid Films 516 (2008) 7753-7757.

[102] M.X. Guo, C.K. Cheng, Y.C. Liu, C.N. Wu, W.N. Chen, T.Y. Chen, C.T. Wu, C.H. Hsu, S.Q. Zhou, C.F. Chang, L.H. Tjeng, S.F. Lee, C.F. Pai, M. Hong, J. Kwo, Single-crystal epitaxial europium iron garnet films with strain-induced perpendicular magnetic anisotropy: Structural, strain, magnetic, and spin transport properties, Phys. Rev. Mater. 6 (2022) 054412.

Chapter 3 Experimental methods

3.1 Introduction

Chapter 3 introduces the preparation process of the samples used in this project, and the basic working principles of instruments and characterization methods, including the characterization of microstructure, electrical and magnetic properties. The first section mainly introduces sample preparation techniques, including substrate treatment, thin film deposition, and device preparation. The second section describes the microstructural characterization of films, including surface roughness and crystal microstructures. The third section introduces the performance testing of films and devices, including magnetic and magnetotransport characterization principles and methods.

3.2 Sample preparation

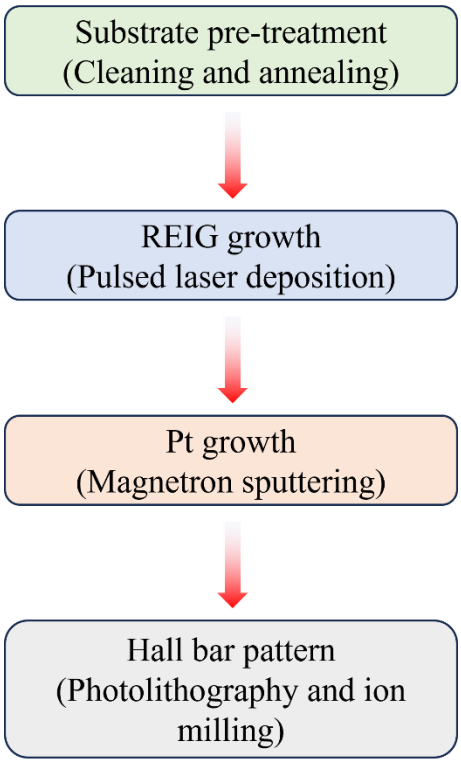

Fig. 3.1 Schematic flowchart of sample preparation.

The study of spin magnetotransport in this thesis is based on the GGG/TbIG/Pt system. Therefore, the sample preparation process mainly involves substrate pre-treatment, thin film deposition, and device fabrication. The specific sample preparation process is shown in the Fig. 3.1.

3.2.1 Substrate pre-treatment

High-quality epitaxial thin films require a flat atomic surface on the substrate, as the substrate's atomic arrangement, defects, and roughness determine the epitaxial thin films' growth and subsequent properties [1]. Taking perovskite ABO_3 substrates as an example. To obtain a surface with only A-type or B-type termination (AO or BO_2), chemical treatment usually plays a crucial role, as wet chemical etching processes (acidic or basic) can be used to selectively remove one specific chemical on the surface. For example, Kawasaki *et al*. successfully prepared chemically homogeneous, atomically-flat surfaces of the commonly-used $SrTiO_3$ (STO) substrate in 1994 [2]. They invented a method for acid etching that relies on the difference in acidity and basicity of different metal oxides on the surface.

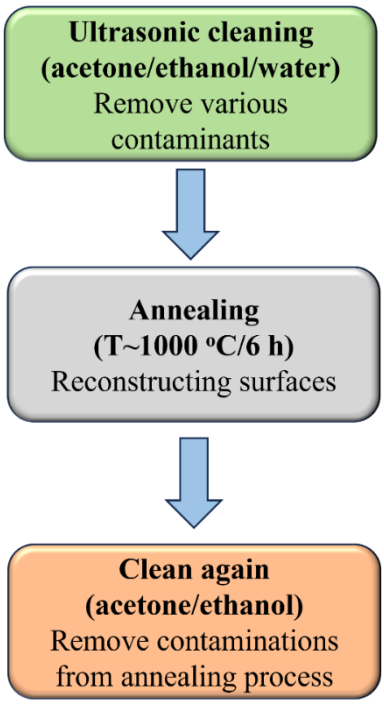

Fig. 3.2 Flowchart of substrate pre-treatment before film growth.

GGG substrates were used throughout the project. Although the GGG substrate does not need to undergo complex chemical etching processes to achieve the expected flat surface like the STO, it should be noted that achieving an atomically flat surface of GGG substrate also requires multiple preprocessing steps such as cleaning and annealing. To achieve a stable GGG surface, it is usually necessary to go through several important steps. Firstly, GGG substrates are cleaned with acetone and alcohol under ultrasonic bath several times, to remove contamination caused by different particles. Then, GGG substrates are annealed 6 hours at high temperature (~1000 ºC), with the aim of reconstructing the surface and obtaining an atomically flat terminal surface with a single chemical composition [3]. Before thin film deposition, the GGG substrates are cleaned again using acetone and ethanol to ensure a clean surface. In this project, one-side-polished GGG (111) substrates were used for the film deposition [4], and the above surface treatment processes were carried out before deposition.

3.2.2 Pulsed laser deposition

Thin film deposition methods can generally be divided into physical and chemical depositions [5, 6]. In this thesis, physical vapor deposition (PVD) technologies were used. The pulsed laser deposition (PLD) method was applied for growing garnet materials [7].

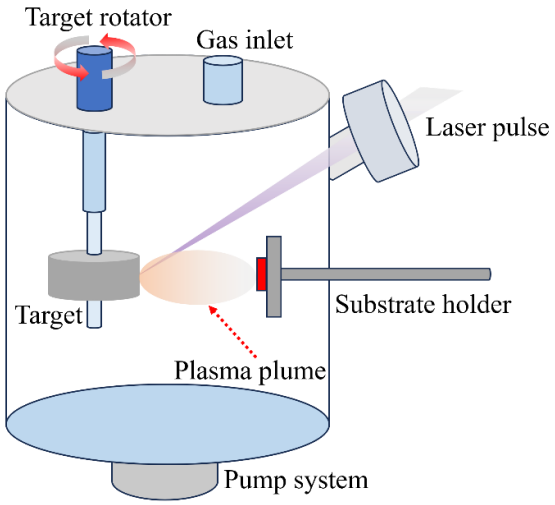

Fig. 3.3 Schematic diagram of the PLD system.

Since Dijkkamp *et al*. successfully prepared $YBa_2Cu_3O_{7-x}$ superconducting thin films by PLD in 1987 [8], widespread attention was drawn towards the PLD technique for preparing epitaxial thin films. Fig. 3.3 illustrates the process of depositing films in a PLD system, which utilizes laser pulses (wavelength $\lambda = 248\,nm$ in this project) to irradiate a rotating target. In an ultra-high vacuum chamber, the surface material is ablated and ejected to form a plasma plume, in which the material required for film growth moves to the substrate. Finally, the plasma condenses and nucleates on the substrate surface, forming the film with expected stoichiometric ratio [9].

Several characteristics of PLD make it advantageous for growing films of complex materials. One of the most important features of PLD is that it ensures the stoichiometric ratio of the deposited films to be consistent with target composition. The ablation process is a non-equilibrium process. When the high-intensity pulsed laser is irradiated onto the target, the target material absorbs the energy of the laser beam, and a thin layer of target surface is heated and ablated. It is noticed that the laser energy density must exceed a certain value, because only sufficiently high energy can cause plasma to appear on the target surface, forming a complex layer (called Knudsen layer) on the target surface [10]. Due to the existence of Knudsen layer on the surface of the target, the density of particles is extremely high, and collisions are frequent. Therefore, the velocities of particles with different compositions tend to be consistent in a short period of time. Their expansion time to reach the substrate is basically the same, ensuring the consistency of the film composition.

Another important feature in the PLD system is the introduction of process gas, which serves two functions. Firstly, the formation of cations typically requires active gases (such as oxygen) as a component of the plasma flux. The interaction between ablative materials and gases typically produces target molecules. In addition, the atmosphere of the chamber can also be used to reduce the kinetic energy of the ablative material, thereby controlling the deposition rate. Moreover, the high-vacuum working environment is also an important feature of PLD, which suppresses contamination and guarantees high-purity of the resultant films.

YAG, TbIG, EuIG, and GGG thin films were deposited with good epitaxy in this thesis. Table 3-1 summarizes the specific growth conditions.

Table 3-1 List of growth conditions for film deposition using PLD

Growth conditions	TbIG, EuIG and GGG	YAG
Temperature (°C)	710	
Laser pulse energy (mJ)	215	
Pulse frequency (Hz)	2	1
Target-substrate distance (mm)	50	
O_2 working pressure (mTorr)	100	
O_2 post-annealing conditions	10 Torr/710 °C/10 min	

3.2.3 Magnetron sputtering

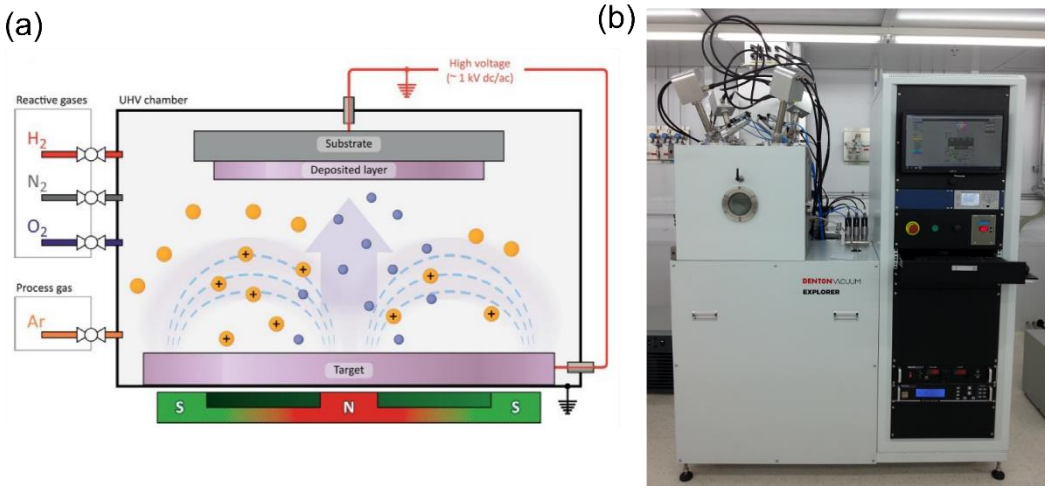

Fig. 3.4 (a) Schematic diagram showing the working principle of a magnetron sputtering system [11]. (b) Sputtering system used in this project.

After the completion of garnets deposition, a thin Pt layer is covered on the garnet film *ex situ* by magnetron sputtering. A magnetron sputtering system mainly consists of vacuum components (e.g. rotary pump and turbomolecular pump), a sputtering chamber, sample stage, and rotating system, direct current (DC)/ radio frequency (RF) sputtering power supply, water cooling system, temperature control system, gas supply

system, etc. DC sputtering is suitable for conductive materials, while RF sputtering is suitable for both conductive and non-conductive materials, such as magnetic insulators.

Fig. 3.4(a) shows the basic principle of the sputtering process. A small amount of high-purity argon (Ar) gas (typically better than 99.995%) is introduced into an ultra-high vacuum chamber, and electrons collide with Ar atoms under the action of an electric field *E* to generate new electrons and Ar^+ ions. The Ar^+ ions move towards the surface of the target and bombard it, allowing neutral molecules or atoms on the target surface to gain sufficient energy and travel to the substrate, forming a thin film. The secondary electrons generated during the sputtering process are bound around the target surface by the dual effects of magnetic and electric fields, and continuously move in a circular motion, which greatly improves the sputtering efficiency [12].

This thesis utilizes the magnetron sputtering system to deposit Pt and electrode materials (titanium and gold), and the specific sputtering parameters are listed in Table 3-2.

Table 3-2 Sputtering conditions for Pt and electrodes

Sputtering condition	Pt	Ti/Au
Temperature	room temperature	
Sputtering mode	RF 80 W	RF 200 W
base pressure	$< 1 \times 10^{-7}$ Torr	
Substrate rotation	30 rpm	
Ar working pressure (Torr)	1.8×10^{-3}	1.8×10^{-3}
Flow control (Ar)	30 sccm	

The magnetron sputtering system used in this project [Fig. 3.4(b)] has a high level of integration, with specific advantages compared with other physical vapor deposition techniques. First, magnetron sputtering deposition can deposit almost any target material, because the magnetron sputtering process does not require evaporation or melting of the material, which means that the melting point of the material is not a

concern. Second, it can accurately control the thickness of the coating and the particle size of the thin film by changing the deposition conditions, such as sputtering energy and the flow rate of working gas. Last but not the least, the sputtering process has good repeatability and can obtain thin films with uniform thickness on large-area substrates, maintaining a similar composition compared with the target material.

3.2.4 Device fabrication

Photolithography and etching are two important steps in making Hall bar patterns. The advantage of photolithography is that it can accurately control the shape and size of the patterns formed, ensuring the repeatability of Hall bars and electrodes. Fig. 3.5 summaries the process of Hall bar fabrication. The main processes include spin coating of photoresist, soft baking, exposure, development, etching, and removal of photoresist [13, 14].

The photoresist spin coating is the initial and important step in the pattern conversion process. According to their different properties, photoresists can be divided into positive and negative photoresists. The difference between these two types of photoresists is that the positive photoresist dissolves in the developer upon UV exposure, forming a three-dimensional pattern. The latter is cured under UV exposure while the unexposed areas are dissolved in the developer. AZ5214E, a positive photoresist, was used in this thesis [15].

The quality of photoresist directly affects the defect density of the processed components. To ensure the repeatability of line widths and the subsequent development time, the uniformity of photoresist thickness of the same series of samples should not exceed ± 5 nm. In this step, a uniform thickness can be achieved by controlling the rotation speed and time of spin coating.

After completing the spin coating of photoresist, soft baking is required for the solvent to evaporate from the photoresist (reducing the solvent content to ~5%), thereby reducing dust contamination. Meanwhile, the soft baking step can also reduce the film stress caused by high-speed rotation, thereby improving the photoresist adhesion.

The proximity printing method is conducted in the exposure step, with a slight separation of approximately 20 μm between the mask and photoresist layers. As shown in the schematic diagram (2) in Fig. 3.5, a specific wavelength (350 ~ 450 nm) of UV light is selectively irradiated on the photoresist covering the substrate. The photosensitive agent in the photoresist undergoes a photochemical reaction, causing a change in the chemical composition of the illuminated area of AZ5214E photoresist. The areas where these chemical components undergo changes can be dissolved in the developing solutions in the next step.

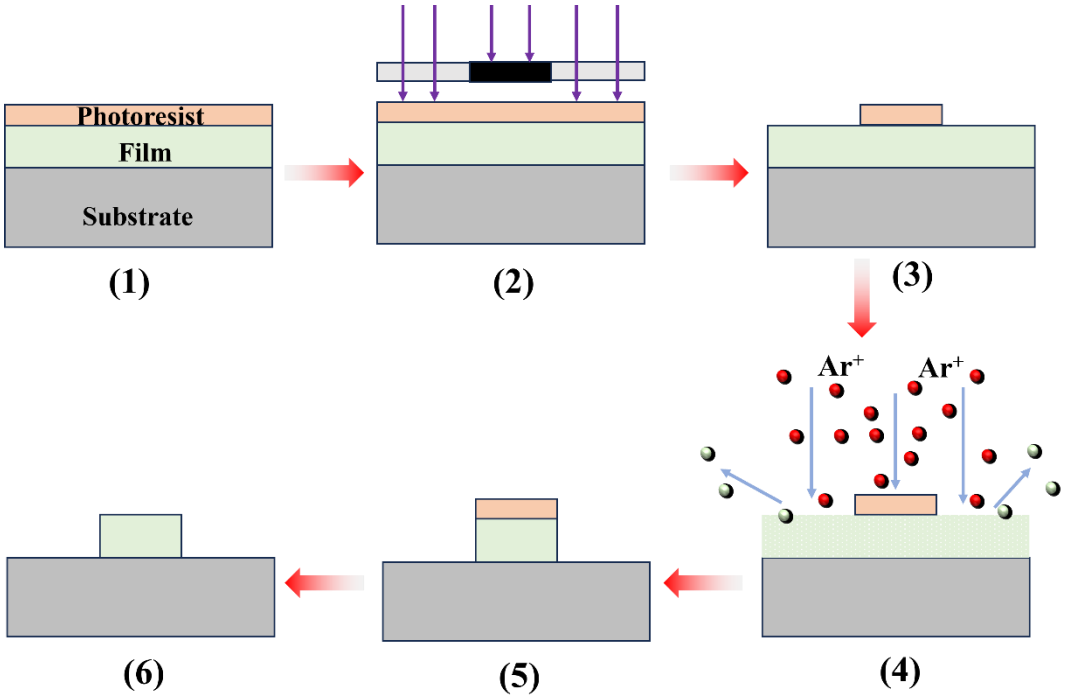

Fig. 3.5 Schematic diagram for fabricating Hall bars in this thesis.

After exposure, the sample is placed in the developer, and the photosensitive area of AZ5214E is dissolved in the developer. When this step is completed, a Hall bar pattern is obtained. To improve resolution, almost every type of photoresist has a dedicated developer to ensure high-quality development effects. Fig. 3.6 shows the photolithography system (SUSS MA6), and the prepared Hall bar devices used in this thesis.

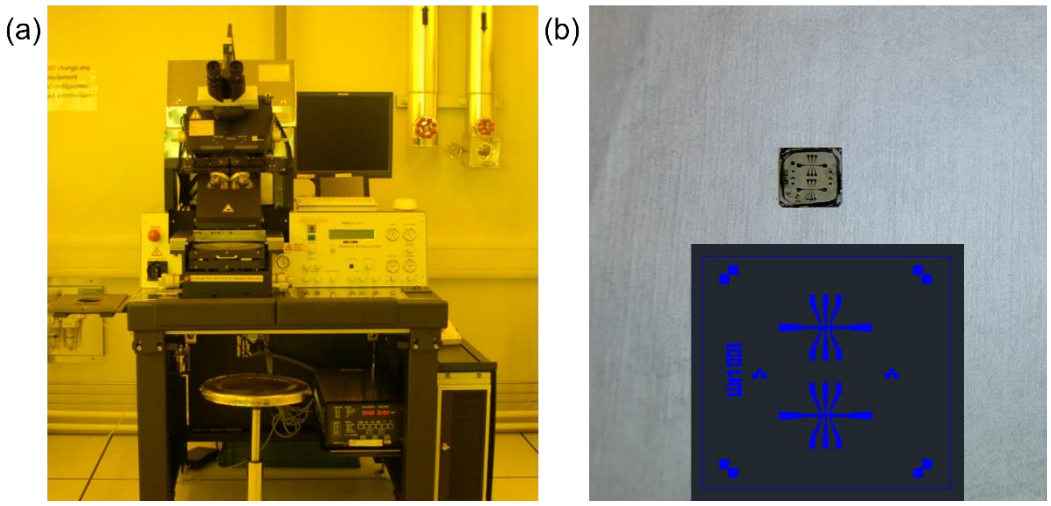

Fig. 3.6 (a) SUSS MA6 Mask Aligner. (b) The Hall device prepared by photolithography and etching.

The Hall bar pattern needs to be obtained through ion etching, which is a purely physical etching process. Firstly, Ar gas is filled into a high vacuum cavity and ionized to form a plasma. Then, ions are controlled in a beam shape and accelerated to bombard on the sample surface, causing material atoms to sputter and achieve etching. Due to the prepared photoresist on the surface of the film, the exposed part will be etched off, while the masked parts will be retained to form the required Hall pattern.

Finally, the cleaning of the photoresist is carried out. The photoresist is dissolved and removed by soaking in acetone and then cleaned several times with alcohol, in order to remove pollutants generated during the lithography process.

3.3 Structure characterization

This section introduces the three structural characterization methods used in the project, namely X-ray diffractometry (XRD), X-ray reflectivity (XRR), atomic force microscopy (AFM), and transmission electron microscopy (TEM).

3.3.1 X-ray Diffractometry

XRD utilizes the X-rays diffraction phenomenon in crystals to obtain the characteristics X-ray spectra of the sample. By utilizing the spectral information, not

only can the crystal phases be determined, but the presence of lattice defects within the sample can also be analyzed.

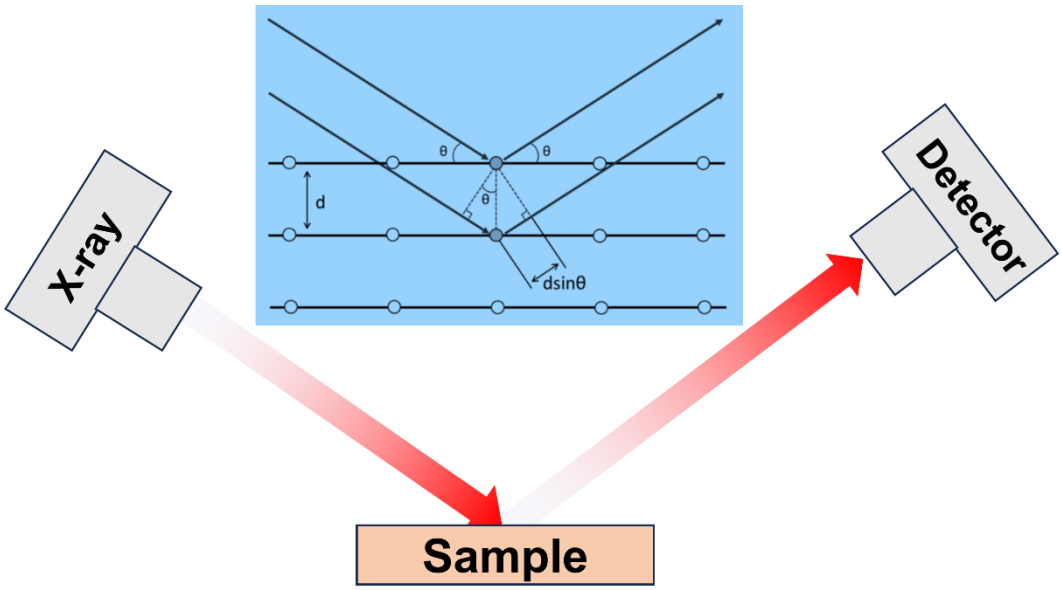

Fig. 3.7 Schematic diagram of principle of XRD.

Fig. 3.7 exhibits the basic principle of XRD. When a beam of X-rays is irradiated on a crystal, electrons around the atoms in the crystal are excited under the action of an electric field and scatter the X-rays. Based on the periodicity of crystal structure, the scattered waves arising from different atomic layers in the crystal can interfere with each other. The diffraction phenomenon of X-rays in crystals is essentially the result of interference of X-rays scattered by a large number of atomic layers acting as diffraction gratings. The Bragg equation is the fundamental formula in diffraction analysis [16] and is expressed as:

$$n\lambda = 2d\sin\theta, \qquad (3-1)$$

where λ, d and θ represent the wavelength of the X-ray, the spacing between crystal planes, and the angle between the incident X-ray and the corresponding crystal plane. When samples are irradiated by X-rays, the optical path difference between two beams scattered by adjacent crystal planes is $2d\sin\theta$. If the optical path difference is equal to $n\lambda$, constructive interference occurs and the diffraction intensity of X-rays is intensified; in other conditions the X-ray intensity is attenuated. Obviously, through the

Bragg equation, the crystal plane spacing d can be solved using λ of X-ray to obtain crystal structure information, thus achieving structural analysis.

The structural characterization of epitaxial films uses high-resolution XRD (HRXRD) technology. HRXRD is commonly used to characterize the quality, thickness, roughness, and dislocation density of epitaxial films. Compared to conventional XRD, HRXRD has the following characteristics:

(1) The incident X-beam is collimated and close to a plane wave.

(2) Sensitive to small lattice changes.

(3) Higher angular resolution.

3.3.2 X-ray Reflectivity

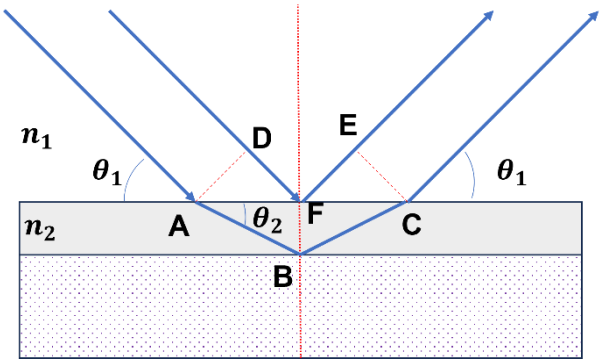

Fig. 3.8 Schematic diagram of principle of XRR.

XRR is a surface analysis method for analyzing film roughness, thickness, and density [17]. The basic principle of XRR is to utilize the reflection of X-rays on the top surface and interfaces between substrates and films, as well as the mutual interference of such reflected beams. The principle of XRR is related to the Snell's law, express as:

$$n_1 \sin\theta_1 = n_2 \sin\theta_2 \qquad (3-2)$$

where n_1 and n_2 represent different refractive indices, θ_1 and θ_2 represent the incident angle and refracted angle, respectively. As shown in Fig. 3.8, when X-rays are directed toward the sample at an angle less than a certain critical angle θ_c, total reflection occurs. When $\theta_1 < \theta_c$, total reflection occurs and no X-rays enter the sample. When $\theta_1 > \theta_c$, refraction occurs. Refracted light will continuously reflect and refract

at the interfaces of the films (Fig. 3.8), and the reflected beams between the interfaces will interfere with each other, forming periodic interference fringes.

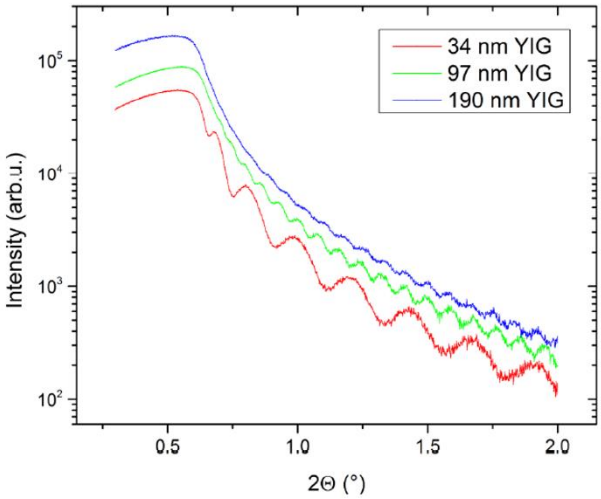

Fig. 3.9 XRR plots for YIG films of different thickness [18].

Fig. 3.9 shows the XRR plots of YIG films deposited on GGG substrates with different thicknesses. The thickness of a film can be approximated by the separation between adjacent oscillation peaks using the following formula:

$$t = \frac{[(n+1) - n] * \lambda}{2 * (\sin\theta_{n+1} - \sin\theta_n)} \approx \frac{\lambda}{2 \triangle \theta} \qquad (3-3)$$

Where t represents the thickness of the film, and $\triangle \theta$ is the angle between adjacent oscillation peaks. As the thickness of the film changes, the oscillation period of the interference fringes also shows a certain variation pattern. The thicker the YIG film, the more closely-packed are the oscillations of the peak.

3.3.3 Atomic force microscopy

AFM can be used for surface observation, surface roughness measurement, feature size measurement, particle size analysis, etc., and has become a basic tool for nanoscience research. The principle of AFM is that it utilizes the van der Waals force between atoms to present the surface characteristics of the sample. While other microscopy techniques [scanning electron microscopy (SEM)] can only provide two-dimensional images, AFM provides three-dimensional surface information.

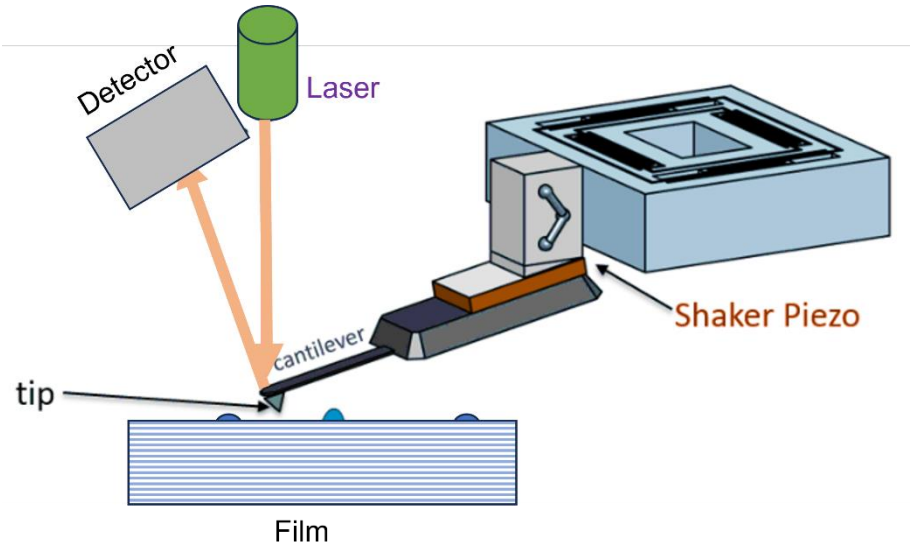

Fig. 3.10 Schematic diagram of principle of AFM.

As shown in Fig. 3.10, one end of a micro cantilever is fixed to a substrate, and the other end has a very small needle tip attached; the long cantilever is extremely sensitive to weak forces. The needle tip then lightly contacts the surface of the sample. Due to the extremely weak repulsive force between the atoms at the needle tip and on the sample surface, by controlling the force during the scanning process the micro cantilever will undulate and move in the direction perpendicular to the surface of the sample, corresponding to the equipotential plane of the interaction force between the needle tip and the sample surface. The optical detection method is used to measure the position changes of the microcantilever corresponding to the scanning points, thereby obtaining information on the surface morphology of the sample.

3.3.4 Transmission electron microscope

Fig. 3.11 shows the schematic structure and the actual appearance of the TEM. The basic imaging principle of TEM is that the electron beam is accelerated onto a very thin sample (at the nanoscale thickness), where electrons collide with atoms in the sample and change direction, resulting in stereo-angular scattering. The size of the scattering angle is related to the density, thickness, etc. of the measured sample, so it

can form images with different bright and dark field conditions. After magnification and focusing, the images are finally displayed on the imaging device.

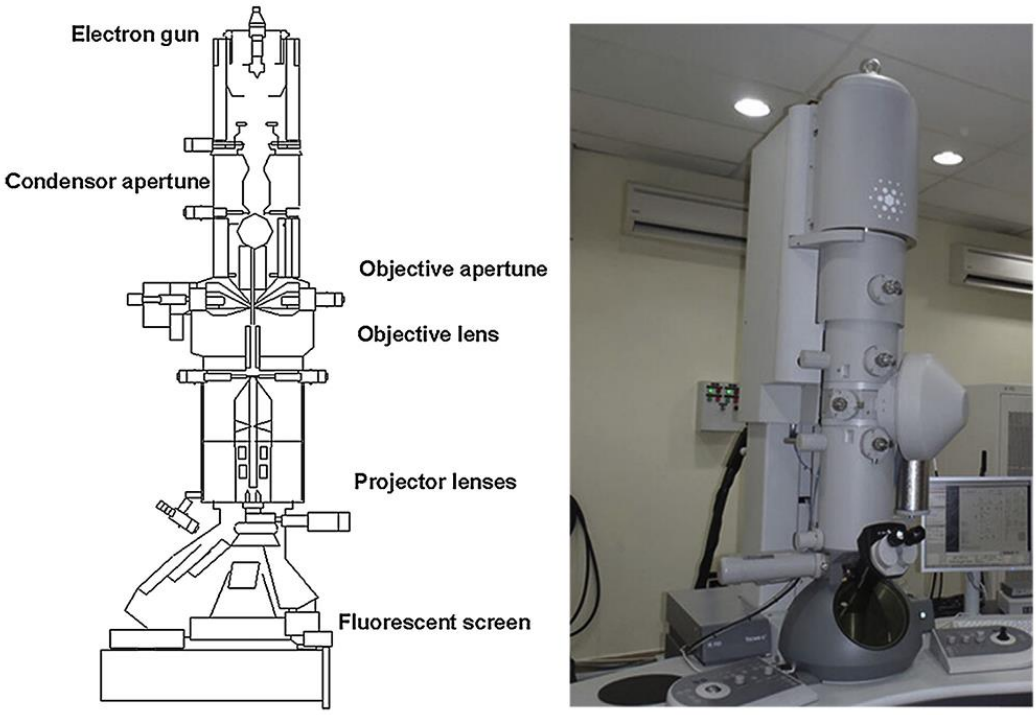

Fig. 3.11 Schematic diagram of principle of TEM system [19].

TEM systems can obtain high-resolution images because it solves two key problems. First, the high-energy electrons emitted by the electron gun have extremely short effective wavelengths. The shorter the wavelength, the more details that can be distinguished. Second, the TEM system can control the movement of electrons, allowing the electron beam to be focused and amplified for imaging purposes. Therefore, the magnification of TEM can be as high as millions of times.

Scanning transmission electron microscopy (STEM) combines the functions of both TEM and SEM. STEM scans the surface of the sample with an electron beam and images it through electron penetration. The scanning coil forces the electron probe to scan on the sample, and its detector is placed below the sample to receive the transmitted electron beam or an elastic scattered electron beam. After amplification, the image is displayed on a fluorescent screen. The advantage of STEM is that it can observe thicker or lower contrast samples for high-resolution analysis and imaging.

Micro-area diffraction can also be achieved. Moreover, STEM can collect and process elastic scattering and inelastic scattering electrons.

The TEM family helps us to fundamentally understand the relationship between material properties and microstructure, which is of great significance for promoting the development of multiple fields such as physics, chemistry, and materials science.

3.4 Magnetic and electrical transport measurements

As the focus of this thesis is on the spin Hall magnetotransport of FMI/HM systems, the performance of the system (includes magnetic and magnetotransport measurements) were characterized. The following section briefly introduces the basic principles of vibration sample magnetometer (VSM) and physical property measurement system (PPMS).

3.4.1 Vibrating sample magnetometer

VSM can be used to measure magnetic materials in different forms (bulk samples, powder, liquid, and thin films). The basic structure of a VSM is shown in Fig. 3.12. VSM functions based on the principle of electromagnetic induction. It can detect the magnetic moment through vibrating a sample at a fixed frequency and amplitude about the center of the pick-up coil. If the sample vibrates along the *z*-axis at a specific position, a small coil with an axial direction parallel to the *x*-axis will generate an induced voltage:

$$E_g = G\omega\delta \cos \omega t = km, \qquad (3-4)$$

where G is the geometric factor of the coil, ω and δ are the vibration frequency and the amplitude, and m is the magnetic moment of the sample. By obtaining the proportionality coefficient k, the magnetic moment of the sample can be obtained through E_g. The k value is typically obtained by calibration against a standard nickel ball with known magnetization signal.

VSM measurement does not impose strict requirements on the geometry of the sample. For sufficiently small samples, the induced voltage generated by vibration in

the detection coil is proportional to the magnetic moment of the sample. By measuring this voltage through a lock-in amplifier, the magnetic moment of the sample can be calculated.

A Lakeshore-VSM was used to measure the *M-H* loops of garnet thin films in the thesis. The instrument has a stable and reliable vibration system, and the magnetic field source is digitally controlled. Its maximum measured magnetic field is ± 2 T, and the theoretical operating temperature is between 15 K-300 K.

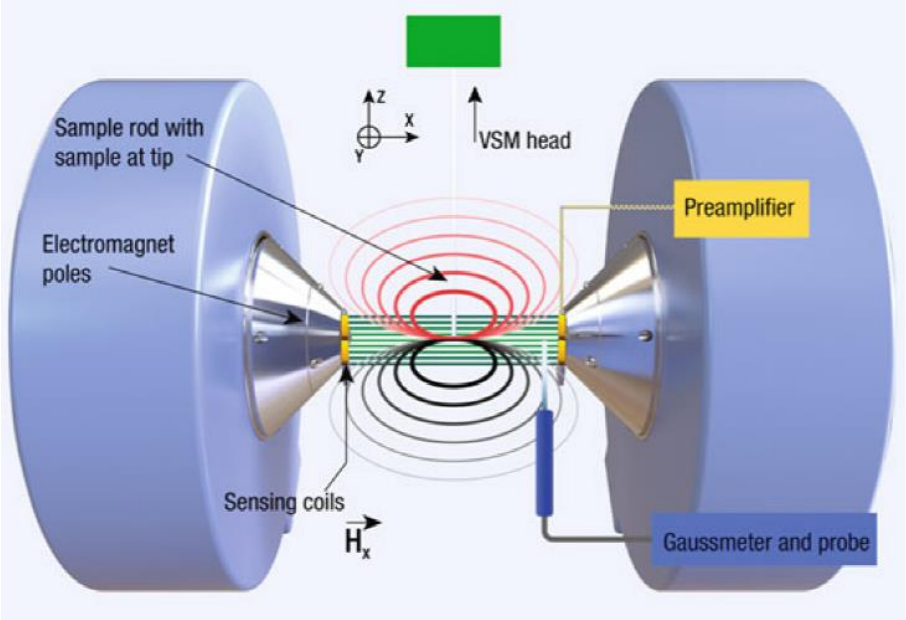

Fig. 3.12 Schematic diagram of a VSM system [20].

3.4.2 Physical property measurement system

PPMS can be used for measuring various physical properties such as resistivity, magnetic resistance, Hall coefficient, hysteresis loop, Seebeck coefficient, and thermal conductivity, etc. The spin Hall transport of Hall devices in this project requires the use of the AC transport measurement module of PPMS.

Fig. 3.13(a) exhibits the PPMS system (Dynacool 9, Quantum Design) used in this thesis. The AC transport property measurement module can perform 4-wire measurements of DC resistivity, AC resistivity, 4-wire or 5-wire connections Hall

effect measurements, and I-V characteristics measurements. The sample installation and connection are convenient, and multiple samples can be measured in one single run. The maximum working magnetic field of PPMS can reach 9 T, with a temperature range of 1.9 K-400 K.

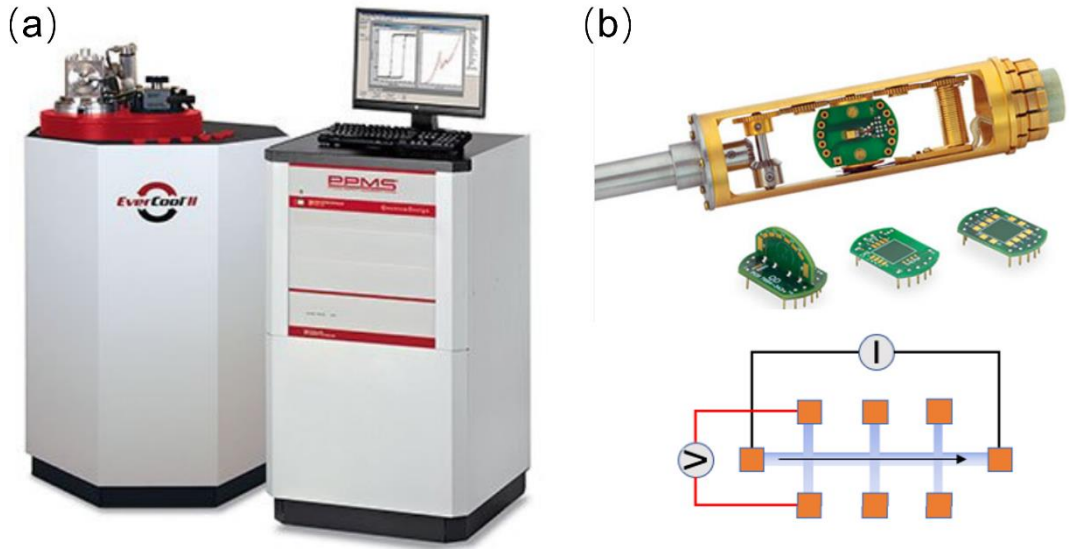

Fig. 3.13 (a) PPMS system used in this thesis. (b) Sample rod and holder used for Hall device measurement, and a schematic diagram of the current and voltage directions in the Hall transport measurement. The direction of the external magnetic field is always along the direction of the sample rod.

Fig. 3.13(b) shows the current and voltage wiring method in Hall measurement. Although the sample holder of PPMS can rotate 360 degrees, it should be noted that its internal magnetic field is along the vertical direction. To achieve angular-dependent measurement of magnetoresistance in the three axes, it is necessary to choose a suitable sample holder and wiring method.

References for Chapter 3

[1] A. Biswas, C.-H. Yang, R. Ramesh, Y.H. Jeong, Atomically flat single terminated oxide substrate surfaces, Prog. Surf. Sci. 92 (2017) 117-141.

[2] M. Kawasaki, K. Takahashi, T. Maeda, R. Tsuchiya, M. Shinohara, O. H. Ishiyama, Koinuma, Atomic control of the $SrTiO_3$ crystal surface, Science 266 (1994) 1540-1542.

[3] G. Koster, B.L. Kropman, G.J.H.M. Rijnders, D.H.A. Blank, H. Rogalla, Quasi-ideal strontium titanate crystal surfaces through formation of strontium hydroxide, Appl. Phys. Lett. 73 (1998) 2920-2922.

[4] Y.K. Liu, H.F. Wong, K.K. Lam, K.H. Chan, C.L. Mak, C.W. Leung, Anomalous Hall effect in Pt/$Tb_3Fe_5O_{12}$ heterostructure: Effect of compensation point, J. Magn. Magn. Mater. 468 (2018) 235-240.

[5] J. E. Crowell, Chemical methods of thin film deposition: Chemical vapor deposition, atomic layer deposition, and related technologies. J. Vac. Sci. Technol. A 21 (2003) S88-S95.

[6] P. Panjan, A. Drnovšek, P. Gselman, M. Čekada, M. Panjan, Review of growth defects in thin films prepared by PVD techniques, Coatings 10 (2020) 1-40.

[7] J. A.Greer, History and current status of commercial pulsed laser deposition equipment. J. Phys. D: Appl. Phys. 47 (2013) 034005.

[8] D. Dijkkamp, T. Venkatesan, X.D. Wu, S.A. Shaheen, N. Jisrawi, Y.H. Min-Lee, W.L. McLean, M. Croft, Preparation of Y-Ba-Cu oxide superconductor thin films using pulsed laser evaporation from high T_c bulk material, Appl. Phys. Lett. 51 (1987) 619-621.

[9] R. Dietsch, T. Holz, H. Mai, M. Panzner, S. Völlmar, Pulsed laser deposition (PLD)—An advanced state for technical applications. Opt. Quant. Electron. 27 (1995) 1385-1396.

[10] H.-U. Krebs, M. Weisheit, J. Faupel, E. Süske, T. Scharf, C. Fuhse, M. Störmer, K. Sturm, M. Seibt, H. Kijewski, Pulsed laser deposition (PLD)--a versatile thin

film technique, Adv. solid state phys. 43 (2003) 505-518.

[11] F. Wang, H. Zhao, J. Liang, T. Li, Y. Luo, S. Lu, X. Shi, B. Zheng, J. Du, X. Sun, Magnetron sputtering enabled synthesis of nanostructured materials for electrochemical energy storage, J. Mater. Chem. A8 (2020) 20260-20285.

[12] P. J. Kelly, R. D. Arnell, Magnetron sputtering: a review of recent developments and applications. Vacuum 56 (2000) 159-172.

[13] Y. Nishimura, K. Yano, M. Itoh, M. Ito, Photolithography, Flat Panel Disp. Manuf. (2018) 287-310.

[14] R.P. Seisyan, Nanolithography in microelectronics: A review, Tech. Phys. 56 (2011) 1061-1073.

[15] R. Guo, L. Qi, L. Xu, H. Zou, Fabrication of sub-50 nm nanochannel array by an angle forming lift-off method, J. Manuf. Processes 75 (2022) 584-592.

[16] C. G. Pope, X-ray diffraction and the Bragg equation. J. Chem. Educ. 74 (1997) 129-131.

[17] S. Daniš, Z. Matěj, L. Matějová, M. Krupka, Determination of the thickness of polycrystalline thin films by using X-ray methods, Thin Solid Films 591 (2015) 215-218.

[18] M.C. Onbasli, A. Kehlberger, D.H. Kim, G. Jakob, M. Kläui, A.V. Chumak, B. Hillebrands, C.A. Ross, Pulsed laser deposition of epitaxial yttrium iron garnet films with low Gilbert damping and bulk-like magnetization, APL Mater. 2 (2014) 106102.

[19] C.Y. Tang, Z. Yang, Transmission electron microscopy (TEM), Membrane Characterization (2017) 145-159.

[20] B. Dodrill, J. R. Lindemuth, Vibrating sample magnetometry, Magnetic measurement techniques for materials characterization (2021) 15-37.

Chapter 4 Impact of ultrathin garnet spacers on the magnetotransport in $Tb_3Fe_5O_{12}$/Pt bilayers

The FMI/HM interface plays an important role in spin Hall magnetotransport, as both MPE and SHE at the interface are affected by the interface exchange coupling, which provides the possibility of regulating spin transport through interface engineering methods. In this Chapter, the TbIG/Pt heterostructure is studied to investigate impact of interface modification on the magnetic and electrical transport behavior of the system. Ultrathin garnet spacers (YAG and GGG) are inserted at the TbIG/Pt interface to study the effect of spacers on spin Hall transport, exploring the possibility of magnetotransport behavior regulation via interface modifications.

4.1 Introduction

Spintronic devices have been actively researched in recent years due to its low energy dissipation and information storage ability. One example of such devices can be found in the FMI/HM system [1-4]. The spin magnetotransport in FMI/HM heterostructures originates from the interfacial exchange coupling between FMI and HM. For example, when a charge current flows into the heavy metal Pt, spin accumulation occurs at the Pt interface because of the strong spin orbit coupling. Under the influence of the adjacent ferromagnetic layer, the spin current will be reflected or absorbed at the FMI/HM interface, which is determined by the magnetization direction. Then, the spin current would be converted into a charge current under the action of ISHE, which can be detected through changes in resistance or voltage [5, 6]. This interfacial transport is closely related to two interface effects, namely spin Hall effect and magnetic proximity effect [7]. The competitive relationship between them would affect the intensity and direction of spin current.

The two interface effects (MPE and SHE) have recently attracted much attention. Different spin phenomena including spin pumping [8, 9], SSE [10, 11], SHE, and ISHE

[7, 12] are extensively studied. The physical mechanisms of these two interface effects have been deeply explored by advanced techniques such as polarized neutron reflectometry and X-ray magnetic circular dichroism. These technologies help researchers to reveal the trade-off relationship between MPE and SHE. However, there is little research on how to regulate these two interface effects. Controlling spin transport through interface engineering is worth exploring.

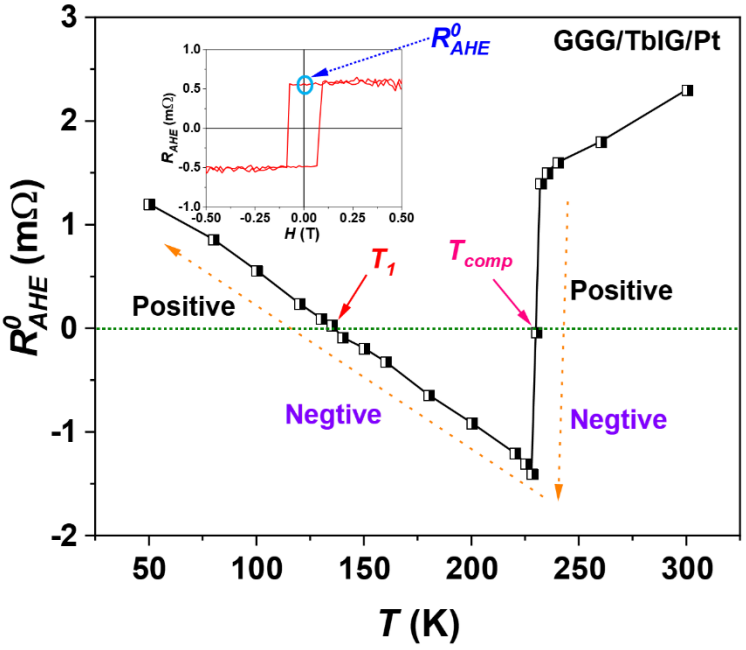

Fig. 4.1 AHE resistance at zero field (R^0_{AHE}) of TbIG/Pt, as extracted from a R_{AHE}-H loop (inset image).

Pt is widely used in spin transport study of FMI/HM systems due to strong SOC [13, 14]. The most popular FMI is YIG due to its low damping, and its combination with Pt helps the observation of the SHE behavior [6, 15, 16]. In similar FMI/HM system such as TbIG/Pt, the R^0_{AHE} exhibits a strong temperature dependence, with R^0_{AHE} showing two sign flips as temperature goes down from 300 K [17, 18]. A sign flip of R^0_{AHE} is defined as the event at which R^0_{AHE} sign changes with varying temperature (Fig. 4.1, yellow dashed arrows). As shown in the Fig. 4.1, there are two intersections between the R^0_{AHE} plot and the temperature axis; the x-intercepts are termed the "cross-over points" in this thesis.

In Fig. 4.1, the first cross-over point coincides with the T_{comp} of TbIG, at which the magnetization of Tb^{3+} and Fe^{3+} sublattices completely cancel out and the net magnetization becomes zero [17, 19, 20]. This sign cross-over is attributed to antiferromagnetically-coupled Tb^{3+} and Fe^{3+} in the garnet, such that their magnetization exhibits different temperature dependences and finally results in the R_{AHE}^{0} sign reversal. Similar sign-flip phenomena has been discussed in DyIG/Pt [21] and GdIG/Pt [22, 23] systems.

The second sign cross-over of R_{AHE}^{0} (here defined as T_1) is considered to arise from the competition between MPE and SHE at FMI/HM interface [18, 20, 24, 25]. On one hand, the imaginary part (G_i) of spin mixing conductance is strongly related to the AHE, which is induced by the interfacial SHE and decreases with the temperature goes down. On the other hand, the MPE in Pt also contributes to AHE. Due to the gradual increase of MPE with decreasing temperature and its competitive relationship with SHE, T_1 appears when MPE-induced AHE completely cancels out SHE-induced AHE. The special relationship between these two interface effects makes it possible to control T_1 through interface modifications, such as through the insertion of spacers [26]. Therefore, choosing appropriate materials to coordinate the relationship between MPE and SHE to achieve the goal of regulating T_1 is worth exploring.

In this Chapter, the impact of a spacer on the spin transport in TbIG/Pt heterostructure is studied. YAG and GGG are selected as the spacer material to ensure the similarity of interface crystallinity and quality. Non-magnetic YAG has a garnet structure and a lattice constant (12.003 Å) [27] similar to TbIG (12.436 Å) [28]. The use of ultrathin YAG spacers suggests that stress-relaxation issue can be ignored, and it is possible to achieve coherent film growth on TbIG film [27, 29]. Similarly, paramagnetic GGG (12.383 Å) also has a garnet structure similar to TbIG [30] and is very suitable as an alternative spacer to observe changes in magnetotransport behavior. The lattice mismatch α between the substrate and film materials can be calculated as:

$$\alpha = \frac{A - B}{B} \times 100\%, \qquad (4-1)$$

where A and B represent lattice constants of REIGs and substrate materials, respectively. According to formula (4-1), the mismatch of TbIG/YAG is 3.48 %, while TbIG/GGG is 0.43 %. Another noteworthy point is that GGG exhibits strong paramagnetism just below room temperature, indicating that GGG has certain spin transport ability [31].

The temperature-dependent R_{AHE} was measured for TbIG/spacer/Pt devices. The test results showed that under ultrathin YAG intervention, T_{comp} of TbIG did not show obvious changes, but the amplitude of R_{AHE} showed significant dependence on YAG thickness. Besides, the appearance of YAG resulted in a substantial decrease in the second cross-over point T_1, which also showed thickness dependence. Moreover, the intervention of ultrathin GGG spacer exhibits stronger suppression of spin transport at the interface. Possible explanations are discussed in Section 4.3.

4.2 Experimental details

TbIG (30 nm)/YAG (0 nm, 0.5 nm, 1 nm, and 2 nm) and TbIG (30 nm)/GGG (0.5 nm and 1 nm) samples were prepared by PLD on GGG (111) substrates with an excimer laser of λ = 248 nm. To achieve a smoother interface, the laser frequencies for depositing TbIG and YAG were chosen to be 2 Hz and 1 Hz, respectively. The working oxygen pressure in the chamber was 100 mTorr, and the substrate temperature was selected as 710 ºC. The substrates were pre-processed to reconstruct the surface before being placed into the chamber [17]. The thin film deposition rates were calibrated by a calibration sample. Fig. 4.2 shows the XRR of GGG (111)/TbIG and GGG (111)/YAG. The depositing rates of calibration films can be calculated by curve fitting (red and blue curves). Table 4-1 summarizes the specific deposition rates, calculated as 43.27 s/nm for TbIG and 68.97 s/nm for YAG. It was noticed that TbIG did not show significant XRR oscillations; therefore, the TbIG thickness calculated by XRR can only be used as a reference. To confirm the accuracy of film thickness, cross-sectional STEM analysis was conducted to confirm the calibration results. Specific discussions are presented in Section 4.3.

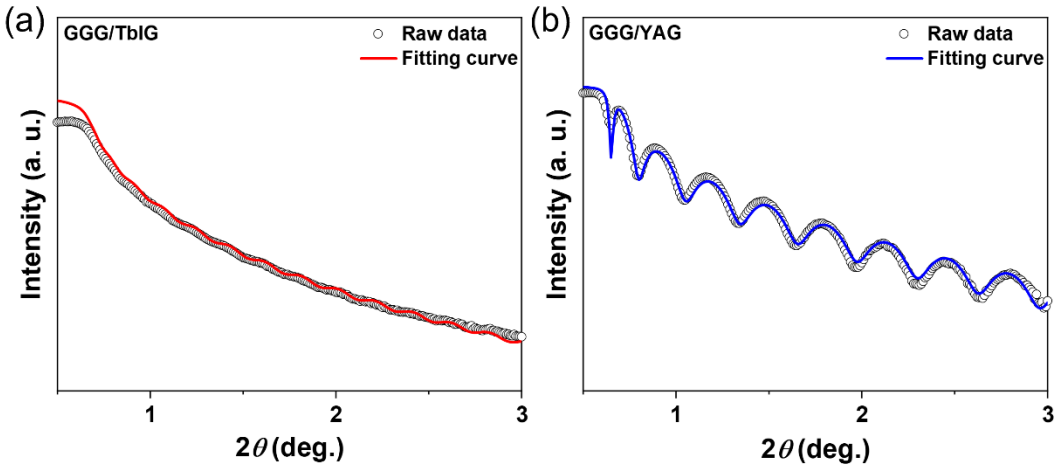

Fig. 4.2 XRR plots for calibration samples of TbIG (a) and YAG (b) on GGG(111) substrates.

Table 4-1 Deposition thickness and rate of calibration samples

Calibration sample	deposition time/ laser repetition rate	Thickness (nm)	Deposition rates (s/nm)
TbIG	30 min/2 Hz	41.6	43.27
YAG	30 min/1 Hz	26.1	68.97

After deposition, the films were annealed in the chamber with 10 Torr of oxygen for 10 min. Then, 5 nm of Pt was capped on the garnet film surface by magnetron sputtering (base pressure $< 10^{-6}$ Torr). Hall bar patterns were defined by photolithography and subsequent Ar ion beam etching. Finally, Ti/Au electrodes were deposited on the Hall bar. The schematic diagram of the Hall device is shown in Fig. 4.3. Hall bar channel length/width is 100×50 μm.

XRD and XRR measurements were conducted using a high-resolution X-ray diffractometer (Rigaku SmartLab). AFM (Asylum 3D infinity) was used to characterize the roughness of the film surfaces. STEM and energy-dispersive X-ray spectroscopy (EDX) imaging were captured by spherical aberration-corrected transmission electron microscopy (AC-TEM) to analyze the microstructure of the samples. MOKE (EvicoMagnetics GmbH) was used to analyze the magnetic properties of the samples,

and R_{AHE}-H plots were captured using PPMS (Quantum Design). As mentioned in Chapter 2, PMA is present when TbIG is deposited on GGG (111) [17, 32]. Therefore, an external magnetic field was applied along the direction of normal to the films during R_{AHE}-H measurements (shown in Fig. 4.3).

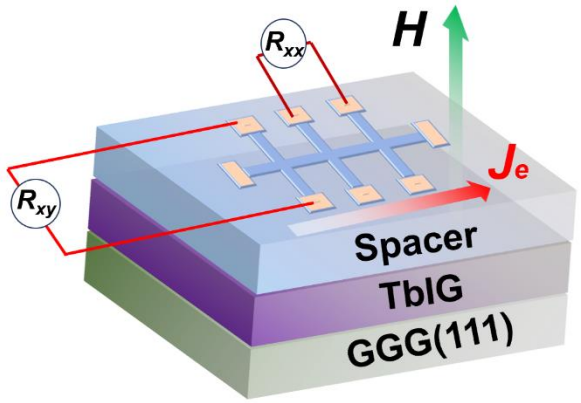

Fig. 4.3 Schematic Hall device. J_e and H represent the charge current and external magnetic field, respectively.

4.3 Results and discussions

4.3.1 Structural characterization

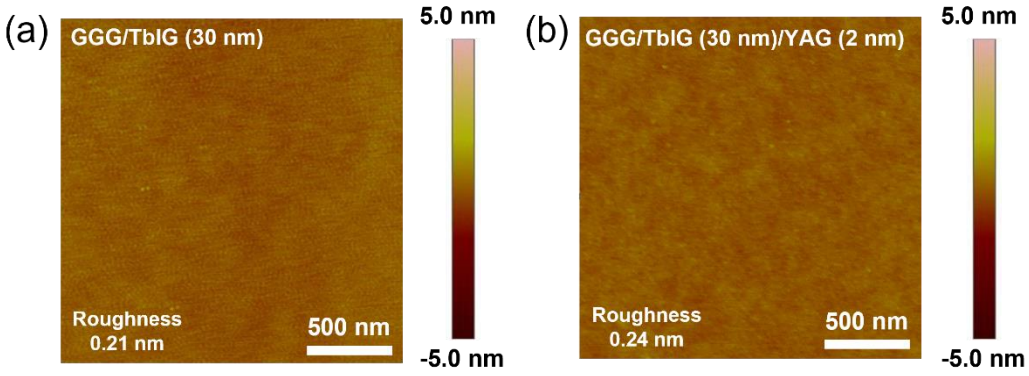

Fig. 4.4 AFM images for (a) GGG/TbIG (30 nm) and (b) GGG/TbIG (30 nm)/YAG (2 nm) samples.

Fig. 4.4 compares the AFM images of GGG/TbIG (30 nm) and GGG/TbIG (30

nm)/YAG (2 nm) samples, both of which show minimal root-mean-square roughness (0.21 nm and 0.24 nm, respectively), indicating atomically smooth surfaces can be achieved in this series of samples.

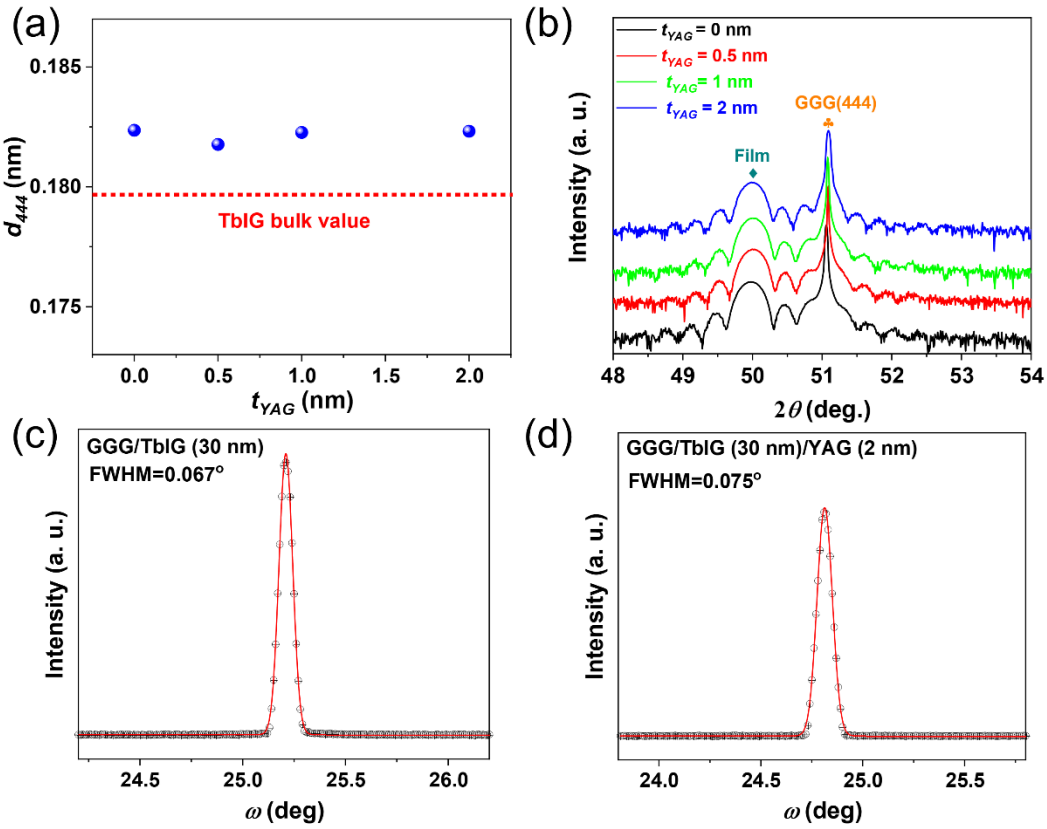

Fig. 4.5 (a) XRD of TbIG (30 nm)/YAG (t nm) bilayers with different spacer thicknesses. (b) Lattice spacing d_{444} as a function of YAG thickness t_{YAG}. (c) and (d) show the rocking curves for GGG/TbIG (30 nm) and GGG/TbIG (30 nm)/YAG (2 nm) samples, respectively.

To confirm the epitaxy of these films, XRD of the samples were measured. Fig. 4.5(a) shows the comparison of 2θ scans for GGG/TbIG/YAG films with different YAG thickness. The main peaks of GGG (444) are highlighted by yellow club, and the epitaxial film peaks (marked by green diamond) appear at the left side of GGG (444) peaks. It can be noticed that as YAG thickness increases, there is no significant change in the film peak position. The lattice spacing values are extracted from Fig. 4.5(a) and are shown in Fig. 4.5(b). The d_{444} of GGG/TbIG (30 nm) sample is 0.182 nm, indicating

a *c*-axis expansion as compared with bulk TbIG (~ 0.1795 nm). Samples with spacers do not show significant d_{444} fluctuations, indicating the ultrathin YAG does not affect the stress and maintains good epitaxial growth in all samples. This good epitaxial quality is also evidenced through the Laue oscillations in Fig. 4.5(a).

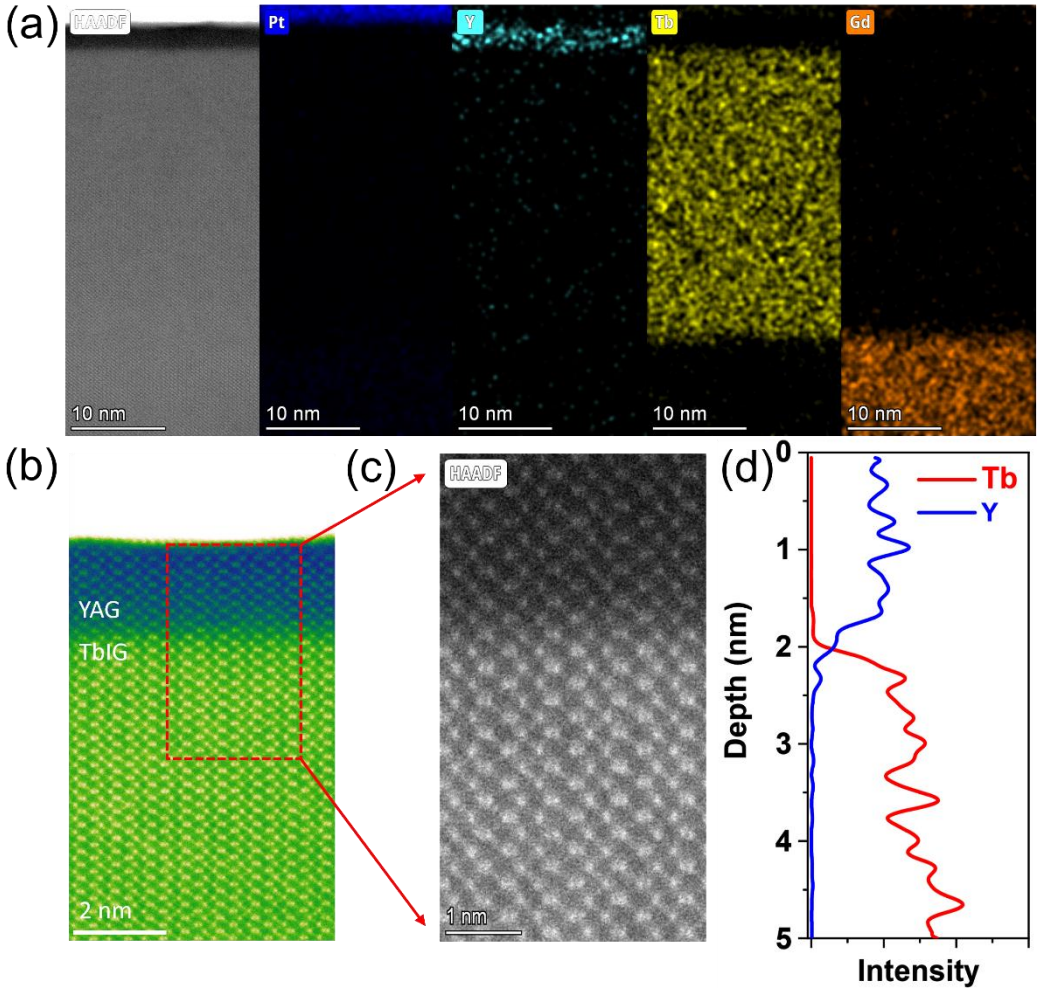

Fig. 4.6 (a) TEM image of GGG/TbIG (30 nm)/YAG (2 nm) specimen (leftmost panel). Gd, Tb, Y and Pt elements can be identified by different colors using EDX as shown in the other panels. (b) TEM image of the cross-sectional TbIG/YAG film. (c) An enlarged atomic structure image focusing on the TbIG/YAG interface range extracted from (b). (d) Line scan of Tb and Y elements from (c).

Fig. 4.5(c) and (d) compare the rocking curves of GGG/TbIG (30 nm) and GGG/TbIG (30 nm)/YAG (2 nm) samples. The similar values (0.067° and 0.075°,

respectively) of full-width at half-maximum (FWHM) indicate comparable mosaic spread and confirm the structural consistency of all samples.

To deeply explore the microstructure of the epitaxial film and confirm the spacer thickness, TEM specimen of GGG/TbIG (30 nm)/YAG (2 nm) was prepared by focused ion beam (FIB) etching. As shown in Fig. 4.6(a), the specific thickness of YAG spacer can be measured through the cross-sectional EDX elements mapping, which is close to ~2 nm. Besides, a minor interface diffusion can also be observed in EDX mapping image. Interdiffusion across garnet interfaces is a common phenomenon and is often observed in literatures [33, 34]. Fig. 4.6(b-c) exhibits a coherent atomic stacking of TbIG/YAG film. Although the lattice mismatch of TbIG/YAG reaches to 3.48 %, no obvious defect is observed at the TbIG/YAG interface, indicating the high epitaxy quality of the sample.

Fig. 4.6(d) shows the result of line scan extracted from Fig. 4.6(c). It is noticed that the thickness of diffusion layer is less than 0.5 nm, which is much smaller than the overall TbIG thickness (30 nm). Also, it proves that TbIG does not have direct contact with Pt, and can form a control experiment with the spin transport of GGG/TbIG/Pt sample.

4.3.2 Magnetic characterization

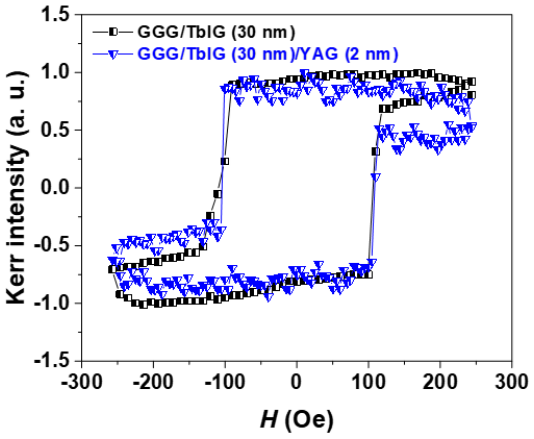

Fig. 4.7 Comparisons of polar MOKE hysteresis loops for GGG/TbIG (30 nm) and GGG/TbIG (30 nm)/YAG (2 nm) samples.

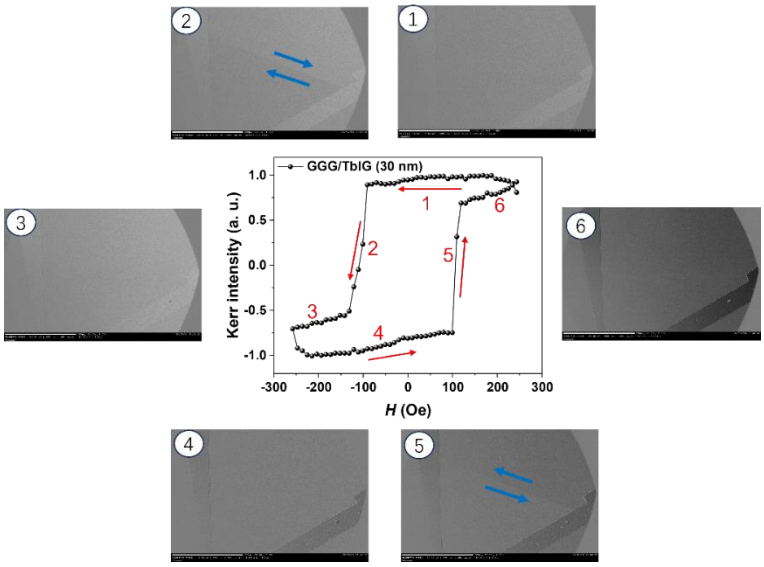

Fig. 4.8 Domain images for GGG/TbIG (30 nm) sample. Numbers in the central *M-H* loop plot correspond to the surrounding MOKE images. The blue arrows in steps 2 and 5 indicate the position of the domain wall. The external field is normal to the film surface.

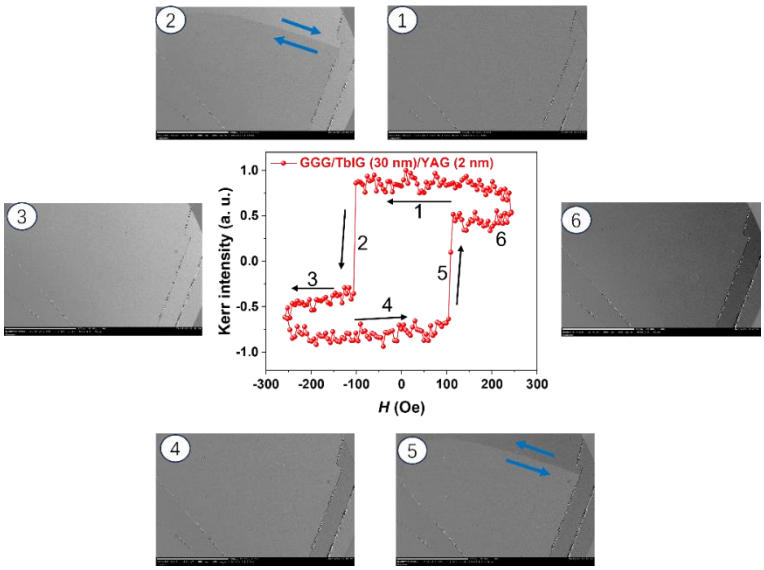

Fig. 4.9 Domain images for GGG/TbIG (30 nm)/YAG (2 nm) sample. Numbers in the central *M-H* loop plot correspond to the surrounding MOKE images. The blue arrows in steps 2 and 5 indicate the position of the domain wall.

For magnetic characterization, Kerr hysteresis loops were measured at room

temperature through polar magneto-optical Kerr microscope (i.e., the Kerr effect that occurs when the magnetization is perpendicular to the surface of the film). Fig. 4.7 shows sharp hysteresis loops with similar coercivity (H_c), indicating that the ultrathin YAG has almost no effect on the anisotropy. The sharp loops also indicate that the easy axis of all samples lies along out-of-plane direction, which can be attributed to the positive magnetostriction coefficient and *c*-axis tensile strain.

To analyze the magnetization reversal process of TbIG/YAG samples, the domain structure at various stages of the *M-H* loops at room temperature was imaged by MOKE and are shown in Fig. 4.8 and Fig. 4.9. In step 1, the film is in a state of magnetization saturation, which means that the internal magnetic domain structures are aligned along the direction of the external field, displayed as a homogenous optical contrast in the MOKE image. However, in step 2, the film undergoes rapid magnetization reversal under the action of a non-zero external field, with an obvious magnetic domain boundary can be observed, consistent with the sharp MOKE signal switching. The blue arrows in step two indicate the alignment of magnetic domains are undergoing a flipping process.

When the magnetization of the film reaches saturation again under a negative field, the magnetic domain disappears. Comparing steps 1 and 3, the difference in magneto-optical contrast can be clearly observed, indicating that the magnetization direction in step 3 is opposite to that in step 1. Similarly, step 4 starts the reversal process and displays the inverse optical contrast compared with the previous three steps.

It is noticed that no obvious nucleation process can be observed in the MOKE images. This may be attributed to the nucleation speed being too fast or having too few defects. However, it does not affect the determination of the variation in the magnetic domains by the change in the contrast of the MOKE images.

4.3.3 Magnetotransport characterization

For GGG (111)/TbIG systems with PMA structure, the strong paramagnetic background of GGG strongly interferes with magnetic signals obtained by VSM or

PPMS. To this end, AHE measurement becomes an effective means to study spin transport and compensation behavior.

Fig. 4.10(a) exhibits the temperature dependent resistance of Pt at room temperature, indicating obvious metallic characteristics. The Pt resistance drops linearly with temperature and slows down at around 10 K, originating from the electron localization [35].

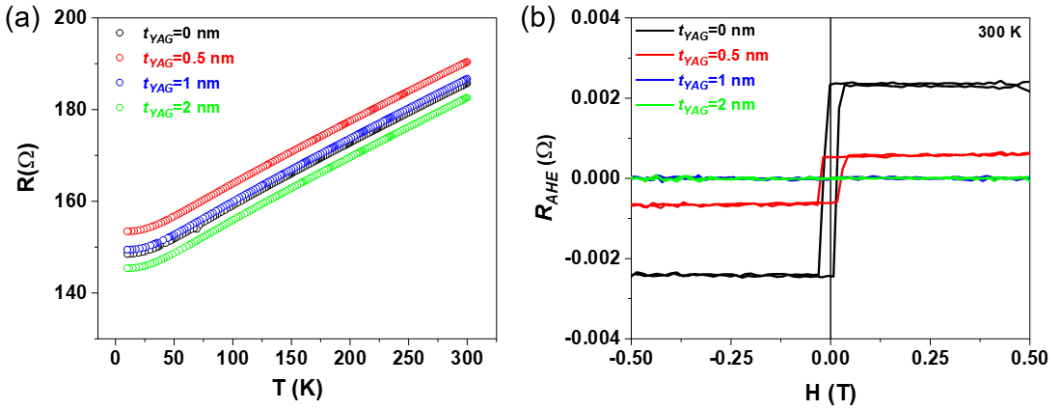

Fig. 4.10 (a) Temperature dependent resistance of Pt for all samples. (b) R_{AHE}-H loops (after subtracting the background signals) at 300 K for all samples.

Although early studies have demonstrated the contribution of internal sublattices to the compensation behavior of TbIG [17, 36, 37], whether varying the interface coupling will affect T_{comp} and T_1 still needs to be explored. In this work, the coupling between TbIG and Pt is regulated by YAG spacers with different thicknesses. Fig. 4.10(b) exhibits the comparisons of R_{AHE}-H loops at 300 K. It is obvious that the amplitude of R_{AHE} decreases sharply with the increase of YAG thickness, and the loop almost disappears when the YAG thickness is 1 nm.

To further analyze the YAG thickness-dependence of R_{AHE}, temperature-dependent R_{AHE} of all samples were measured between 10 K and 300 K. As shown in Fig. 4.11(a), when YAG is absent, the first sign reversal of R_{AHE} appears at ~230 K as temperature goes down, which is consistent with T_{comp}. Interestingly, as displayed in Fig. 4.11(b-c), this sign reversal temperature is almost the same for samples with YAG spacers and the control sample (without YAG), implying that T_{comp} has not changed.

Fig. 4.11(d) shows that when YAG is 2 nm, the AHE signal is too weak to get specific values, indicating that the non-magnetic YAG has blocked the spin Hall transport at the TbIG/Pt interface.

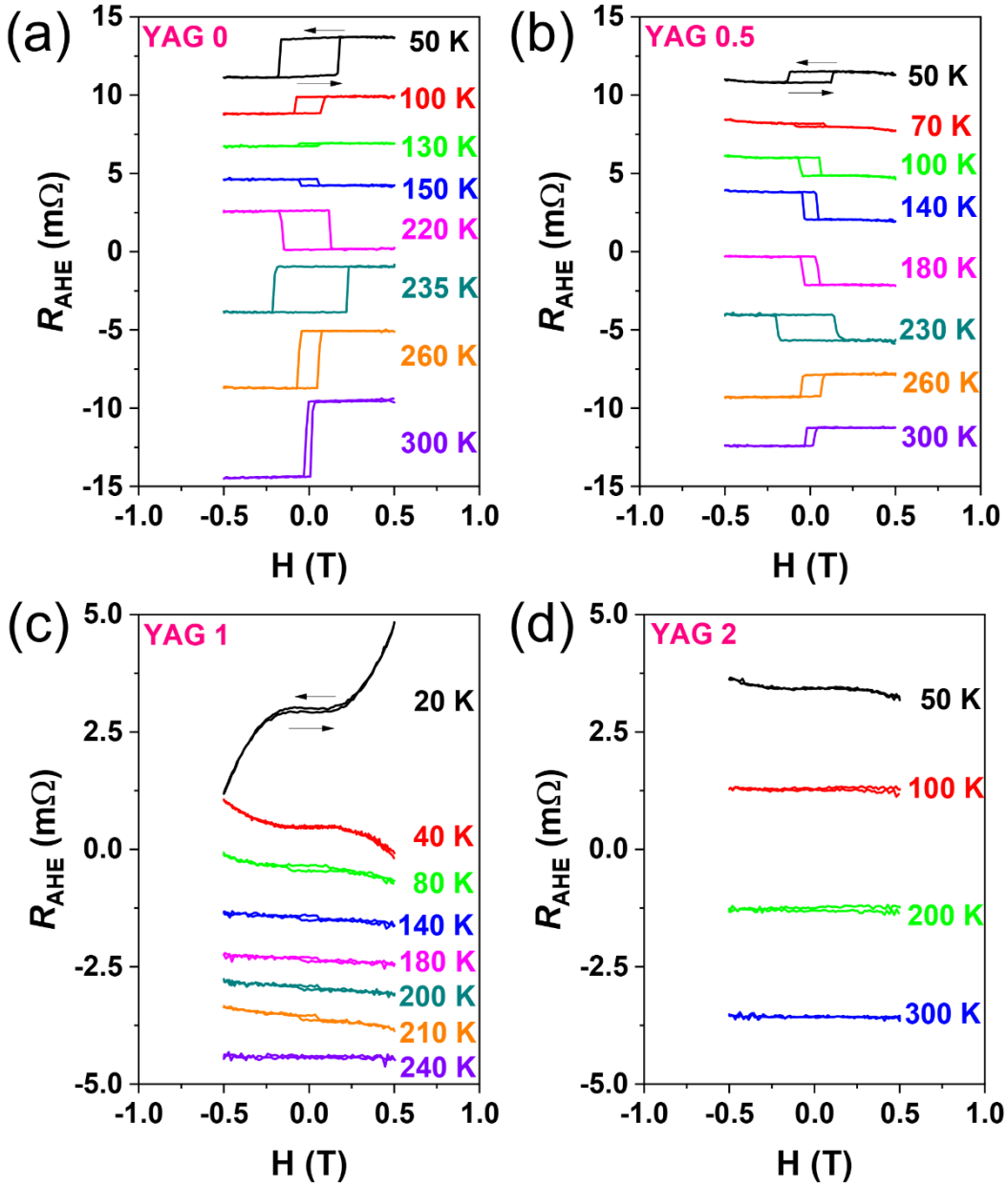

Fig. 4.11 Temperature dependent R_{AHE}-H loops of all YAG spacer samples with different t_{YAG}: (a) 0 nm, (b) 0.5 nm, (c) 1 nm, and (d) 2 nm.

As temperature crosses T_{comp} and continues to decrease, a second R_{AHE} sign flip occurs, generally called the T_1 point. In GGG/TbIG/Pt sample, the T_1 point is at ~135 K, while the insertion of YAG caused a strong suppression of T_1. When t_{YAG} = 0.5 nm,

T_1 is about ~65 K, and is decreased to ~34 K when t_{YAG} = 1 nm. Finally, T_1 disappears at t_{YAG} = 2 nm. The sharp decrease in T_1 indicates that the spin transport at the TbIG/Pt interface is strongly influenced by the YAG spacer.

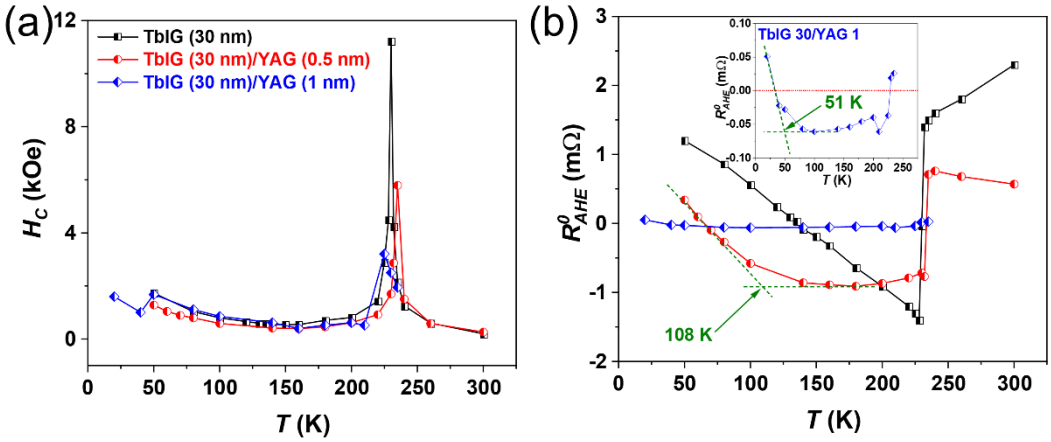

Fig. 4.12 Temperature dependent H_c (a) and R^0_{AHE} (b) for GGG/TbIG/YAG samples with different YAG thickness. Green dashed lines indicate the determination of transition point for MPE dominance. Inset in (b) shows the enlarged $R^0_{AHE} - T$ plot for t_{YAG} = 1 nm.

To intuitively compare and analyze the variations in R_{AHE} for this series of samples, the temperature-dependent H_c and R^0_{AHE} are extracted and plotted in Fig. 4.12. Considering the weak R_{AHE} signals of the t_{YAG} = 2 nm sample, the corresponding data for this sample is not included in Fig. 4.12.

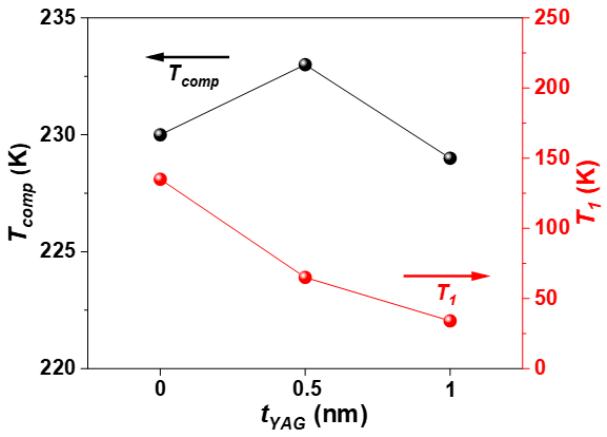

Fig. 4.13 YAG thickness dependent T_{comp} and T_1.

The H_c-T plots for samples of different YAG thickness are shown in Fig. 4.12(a). It is noticed that the divergence of H_c is close to 230 K for all three samples, implying the appearance of T_{comp} as the net magnetization of TbIG vanishes at this temperature. Fig. 4.13 shows the YAG thickness-dependent T_{comp}. Although there is a slight fluctuation in T_{comp}, within the error range of measurement the T_{comp} can be regarded as unchanged for the three samples.

As mentioned earlier, the magnetization compensation behavior in REIG like GdIG [38] and DyIG [21] is strongly related to the competition between different sublattices. The antiparallel alignment of RE and Fe moments results in the appearance of T_{comp} [17]. At above T_{comp}, the Tb^{3+} moment of dodecahedral sites (*c*-site) is weaker than that of Fe^{3+} in octahedral sites (*d*-site). Although the Fe^{3+} at the tetrahedral site (*a*-site) and *d*-site are antiparallel coupled, as well as *c*-site Tb^{3+} and *d*-site Fe^{3+}, the net magnetic moment is dominated by *d*-site Fe^{3+} at above T_{comp}. However, due to the stronger temperature dependence of Tb^{3+} moment as compared with Fe^{3+}, the net moment becomes zero (here at 230 K) and T_{comp} occurs. As the temperature decreases, the net magnetic moment is dominated by Tb^{3+}. T_{comp} detected by AHE can be reflected through the divergence of H_c. As shown in Fig. 4.12, the temperature point where divergent H_c behavior occurs of all samples are almost the same, and is accompanied by the sudden sign flipping of R_{AHE}^0. The two phenomena indicate that the insertion of YAG does not alter the internal coupling of Tb^{3+} and Fe^{3+}, proving the intrinsic nature of T_{comp} that is independent of interface transport.

Meanwhile, T_1 shows a strong thickness dependence of the spacer. Fig. 4.12(b) shows the temperature dependent R_{AHE}^0 of all samples. It is noticed that the temperature of the second cross-over point T_1 decreases with the increases of YAG thickness. The values of T_1 are summarized in Fig. 4.13, with T_1 dropping drastically from 135 K (without YAG) to about 35 K (t_{YAG} = 1 nm). Besides, Fig. 4.12(b) exhibits a significant drop of R_{AHE}^0 amplitude with rising YAG thickness. Interestingly, no divergent H_c happens at T_1, indicating the existence of a physical mechanism different from T_{comp} which causes the drop of T_1.

As previously mentioned, T_1 is related to interface properties at TbIG/Pt. It is known that both MPE and SHE contribute to AHE [24]. MPE-induced AHE is attributed to the induced magnetization in the Pt layer close to the TbIG/Pt interface, while SHE-induced AHE results from the spin accumulation at TbIG/Pt interface. The two effects show competitive relationship [20, 24]. However, MPE is more effective at low temperatures, while SHE dominates the AHE at higher temperatures [39], as indicated in previous studies [20, 21]. For example, in GGG/TbIG/Pt, a balance is reached at around 135 K due to the competition between MPE and SHE, resulting in the existence of T_1 accompanied by the R_{AHE}^0 sign flips.

The insertion of YAG disrupts this balance, as spin information needs to pass through the YAG spacer and the coupling between TbIG and Pt is therefore weakened. The induced magnetization of TbIG in the Pt layer would decrease sharply due to deteriorated interface coupling. As shown in Fig. 4.12(b), the magnitude of R_{AHE}^0 becomes much weaker than control sample (without YAG) even when the non-magnetic YAG is as thin as 0.5 nm. In the case where YAG can block coupling, weak AHE signals might be attributed to the tunneling effect. Similar effect was observed in YIG/Pt heterostructures [40, 41].

Besides, the slope of R_{AHE}^0 plots were studied to analyze the temperature dependence of SHE and MPE. As shown in Fig. 12(b), the R_{AHE}^0 plot without YAG spacer shows a constant slope between T_{comp} and T_1, indicating the linear relationship of AHE intensity with temperature. As mentioned above, MPE competes with SHE and dominates the overall AHE at low temperatures. It is speculated that the dominant position of MPE begins with T_{comp}, and the lower the temperature the stronger is such a dominant effect.

When YAG spacers interfere with TbIG/Pt interface coupling, it is evident that as the thickness of YAG increases, this linear R_{AHE}^0-T relationship at low temperature appears in a narrower temperature range. Moreover, the amplitude of R_{AHE}^0 plots is quite stable, being close to a horizontal line between T_{comp} and T_1. Assuming that MPE begins to dominate the overall AHE at the transition point with a slope of zero, such

transition temperature decreases from ~108 K (t_{YAG} = 0.5 nm) to ~ 51 K (t_{YAG} = 1 nm). The variations in R_{AHE}^0-T slope indicate that the temperature dependence of MPE is affected by the spacer thickness: the thicker the YAG spacer, the more significant inhibition on MPE-induced AHE.

As shown in Fig. 4.12(b), the amplitude of R_{AHE}^0 drops rapidly from 1.5 mΩ (without YAG) to 0.03 mΩ (t_{YAG} = 1 nm) at 235 K and disappears for t_{YAG} = 2 nm. To calculate the decay length of Pt in the GGG/TbIG system, the normalized R_{AHE}^0 of all samples are extracted and presented in Fig. 4.14. An obvious exponential decay of R_{AHE}^0 with YAG thickness is noticed. The attenuation fitting in the Figure follows the equation:

$$\frac{R_{AHE}^0}{R_{AHE}^0(t=0)} = e^{\frac{-t_{YAG}}{\lambda}} \qquad (4-2)$$

where λ is the spin decay length. The decay length of Pt in the TbIG/Pt system was calculated as $\lambda = 0.26\ nm$. This explains the observation that that 2 nm of YAG would evade the observation of magnetotransport at the TbIG/Pt interface.

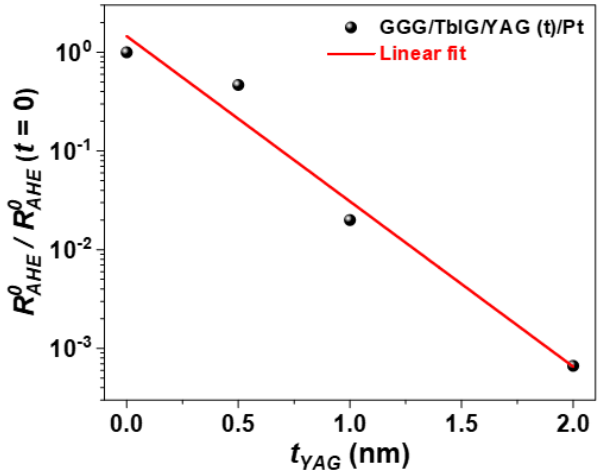

Fig. 4.14 YAG thickness dependence of R_{AHE}^0, normalized with R_{AHE}^0 without YAG spacer (t_{YAG} = 0). The fitting curve indicates the decay length of GGG/TbIG/YAG/Pt system is $\lambda = 0.26\ nm$.

To investigate the sensitivity of interfacial spin transport to different spacers, paramagnetic GGG films was chosen as an alternative spacer material between TbIG

and Pt. GGG possesses a garnet structure similar to TbIG and YAG, which ensures the coherent growth and similar interface situation as compared with TbIG/YAG/Pt structure. A significant difference between YAG and GGG is that the sublattices of YAG does not provide any magnetism as a spacer, while paramagnetic Gd^{3+} ions in GGG has strong magnetization contribution, especially at temperatures below its Curie point (292 K) [42], which may affect the spin transport of TbIG/Pt.

Fig. 4.15 shows the comparison of R_{AHE}-H loops for GGG and YAG spacers with the same thickness of 0.5 nm. It is obvious that R_{AHE} still exists in GGG/TbIG/YAG/Pt, but no AHE signal is observed if YAG spacer is replaced by GGG, even when the spacer is as thin as 0.5 nm.

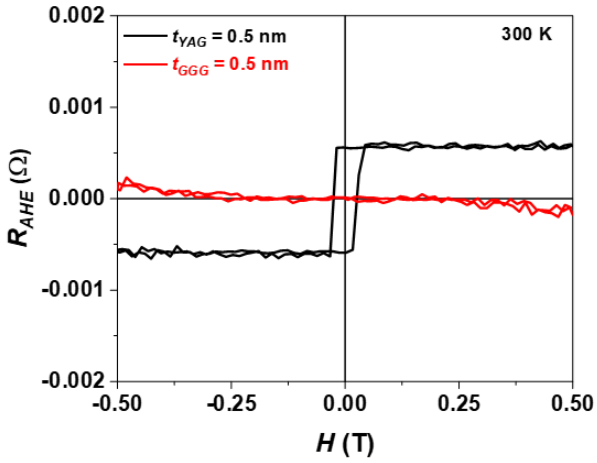

Fig. 4.15 Comparisons of R_{AHE}-H loops for GGG and YAG spacers with the same thickness of 0.5 nm.

Fig. 4.16 shows the temperature-dependent R_{AHE}-H for GGG spacer samples (t_{GGG} = 0.5 and 1 nm). No hysteretic behavior can be observed in these two samples, and they display the same shape of R_{AHE}-H loops across the whole temperature range measured. In fact, the observed signal appears to have contributed from GGG spacer instead of TbIG. The results show significant differences compared to YAG spacer samples, as the signal attenuation of GGG samples is much stronger.

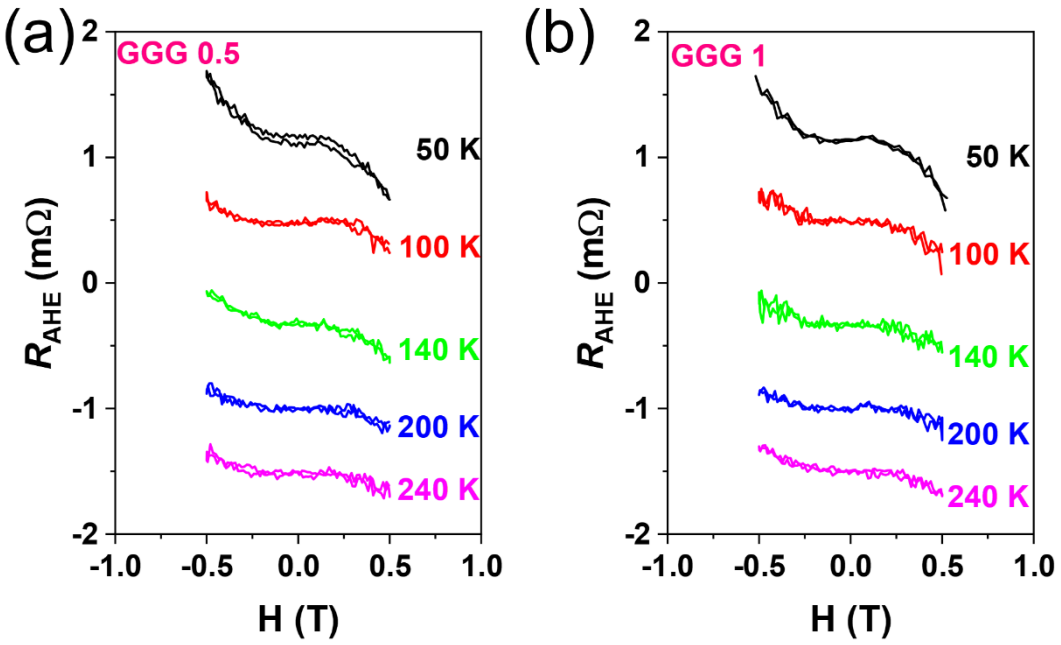

Fig. 4.16 Temperature dependent R_{AHE}-H loops of GGG spacer samples, with (a) t_{GGG} = 0.5 nm and (b) 1 nm.

To analyze the attenuation ability of GGG and YAG on spin transport, a tunneling transmission coefficient D_{ttc} is introduced for quantitative analysis, which can be expressed as $D_{ttc} \propto exp\left[-2t\sqrt{2m\emptyset_{sc}}/\hbar\right]$, where $\emptyset_{sc}$, $,m$ and $\hbar$ are the Schottky barrier, effective electron mass and Planck's constant, respectively [40]. It can be deduced from the formula that the tunneling ability of spin-polarized electron is inversely proportional to the spacer thickness and D_{ttc}.

According to previous work, $\emptyset_{sc}$ can be considered as half of the bandgap value [40]. The bandgap of GGG and YAG are 5.66 eV and 6.5 eV, respectively [43, 44]. As stated in the above formula, the larger the bandgap, the smaller the D_{ttc} value, and the lower ability of spin tunneling. Therefore, the spin tunneling ability of Pt in YAG spacer is expected to be lower than that of GGG spacer. However, the R_{AHE}-H signal of different spacers with the same thickness (0.5 nm) shows opposite results, indicating the size of the bandgap is not the only factor that influences the spin transport capability.

It is known that spin magnetotransport in REIG/Pt system depends on magnon

propagation within REIG [45], but this propagation pathway may be disrupted, especially when encountering magnon with different anisotropy. As mentioned before, GGG is paramagnetic below 292 K, and the 4f-shell of Gd^{3+} contributes a strong magnetism throughout the entire testing temperature range [46]. This could be a contributing factor for the enhanced attenuation of the R_{AHE} signals in TbIG/Pt with GGG as the spacer. This study of spacers with different magnetism should contribute to the design of FMI/HM heterostructures and interface for further spintronic applications.

4.4 Conclusion

In this Chapter, the impact of different garnet spacers on the R_{AHE} behavior of TbIG/Pt system was studied. The main results are highlighted below:

(1) The R_{AHE}^{0} sign in TbIG/YAG/Pt systems show two cross-over points, of which the T_{comp} of all samples has not changed, indicating that changes in the interface do not affect the internal magnetism of TbIG.

(2) The second cross-over point T_1 is influenced by the presence of a spacer between TbIG and Pt. As the YAG thickness increases, the competition between MPE and SHE at the TbIG/Pt interface is significantly affected, causing T_1 to drop drastically from 135 K (without YAG) to about 35 K (t_{YAG} = 1 nm).

(3) YAG spacer shows the stronger spin tunnelling ability in spin magnetotransport than GGG spacer, which is attributed to strong Gd^{3+} moment disturbance below the Curie temperature of Gd.

References for Chapter 4

[1] S. Meyer, M. Althammer, S. Geprägs, M. Opel, R. Gross, S.T.B. Goennenwein, Temperature dependent spin transport properties of platinum inferred from spin Hall magnetoresistance measurements, Appl. Phys. Lett. 104 (2014) 242411.

[2] C. Tang, P. Sellappan, Y. Liu, Y. Xu, J.E. Garay, J. Shi, Anomalous Hall hysteresis in$Tm_3Fe_5O_{12}$/Pt with strain-induced perpendicular magnetic anisotropy, Phys. Rev. B 94 (2016) 140403.

[3] S. Meyer, R. Schlitz, S. Geprägs, M. Opel, H. Huebl, R. Gross, S.T.B. Goennenwein, Anomalous Hall effect in YIG|Pt bilayers, Appl. Phys. Lett. 106 (2015) 132402.

[4] S. Shimizu, K.S. Takahashi, T. Hatano, M. Kawasaki, Y. Tokura, Y. Iwasa, Electrically tunable anomalous Hall effect in Pt thin films, Phys. Rev. Lett. 111 (2013) 216803.

[5] J. Sinova, S.O. Valenzuela, J. Wunderlich, C.H. Back, T. Jungwirth, Spin Hall effects, Rev. Mod. Phys. 87 (2015) 1213-1260.

[6] M. Althammer, S. Meyer, H. Nakayama, M. Schreier, S. Altmannshofer, M. Weiler, H. Huebl, S. Geprägs, M. Opel, R. Gross, D. Meier, C. Klewe, T. Kuschel, J.-M. Schmalhorst, G. Reiss, L. Shen, A. Gupta, Y.-T. Chen, G.E.W. Bauer, E. Saitoh, S.T.B. Goennenwein, Quantitative study of the spin Hall magnetoresistance in ferromagnetic insulator/normal metal hybrids, Phys. Rev. B 87 (2013) 224401.

[7] H. Nakayama, M. Althammer, Y.T. Chen, K. Uchida, Y. Kajiwara, D. Kikuchi, T. Ohtani, S. Geprags, M. Opel, S. Takahashi, R. Gross, G.E. Bauer, S.T. Goennenwein, E. Saitoh, Spin Hall magnetoresistance induced by a nonequilibrium proximity effect, Phys. Rev. Lett. 110 (2013) 206601.

[8] M.V. Costache, M. Sladkov, S.M. Watts, C.H. van der Wal, B.J. van Wees, Electrical detection of spin pumping due to the precessing magnetization of a single ferromagnet, Phys. Rev. Lett. 97 (2006) 216603.

[9] O. Mosendz, J.E. Pearson, F.Y. Fradin, G.E. Bauer, S.D. Bader, A. Hoffmann, Quantifying spin Hall angles from spin pumping: experiments and theory, Phys.

Rev. Lett. 104 (2010) 046601.

[10] S.M. Wu, W. Zhang, A. Kc, P. Borisov, J.E. Pearson, J.S. Jiang, D. Lederman, A. Hoffmann, A. Bhattacharya, Antiferromagnetic spin Seebeck effect, Phys. Rev. Lett. 116 (2016) 097204.

[11] Z. Jiang, C.Z. Chang, M.R. Masir, C. Tang, Y. Xu, J.S. Moodera, A.H. MacDonald, J. Shi, Enhanced spin Seebeck effect signal due to spin-momentum locked topological surface states, Nat. Commun. 7 (2016) 11458.

[12] B.F. Miao, S.Y. Huang, D. Qu, C.L. Chien, Inverse spin Hall effect in a ferromagnetic metal, Phys. Rev. Lett. 111 (2013) 066602.

[13] P. Blonski, S. Dennler, J. Hafner, Strong spin-orbit effects in small Pt clusters: geometric structure, magnetic isomers and anisotropy, J. Chem. Phys. 134 (2011) 034107.

[14] P.M. Haney, H.-W. Lee, K.-J. Lee, A. Manchon, M.D. Stiles, Current induced torques and interfacial spin-orbit coupling: Semiclassical modeling, Phys. Rev. B 87 (2013) 174411.

[15] H.L. Wang, C.H. Du, Y. Pu, R. Adur, P.C. Hammel, F.Y. Yang, Scaling of spin Hall angle in 3d, 4d, and 5d metals from $Y_3Fe_5O_{12}$/metal spin pumping, Phys. Rev. Lett. 112 (2014) 197201.

[16] Y.K. Liu, H.F. Wong, X. Guo, S.M. Ng, K.K. Lam, Y. Zhu, C.L. Mak, C.W. Leung, Enhanced anomalous Hall effect in Pt/CoO heterostructures by ferrimagnetic insulator gating, ACS Appl. Electron. 1 (2019) 1099-1104.

[17] Y.K. Liu, H.F. Wong, K.K. Lam, K.H. Chan, C.L. Mak, C.W. Leung, Anomalous Hall effect in Pt/$Tb_3Fe_5O_{12}$ heterostructure: Effect of compensation point, J. Magn. Magn. Mater. 468 (2018) 235-240.

[18] P.G. Li, J.M. Liang, S.M. Ng, H.F. Wong, Y. Zhou, L.J. Huang, K.W. Lin, Y.H. Tsang, C.L. Mak, C.W. Leung, Tunable compensation temperature through ferromagnetic coupling in perpendicular $Tb_3Fe_5O_{12}$/$Eu_3Fe_5O_{12}$ bilayer heterostructure, J. Magn. Magn. Mater. 592 (2024) 171785.

[19] S. Becker, Z. Ren, F. Fuhrmann, A. Ross, S. Lord, S. Ding, R. Wu, J. Yang, J.

Miao, M. Kläui, G. Jakob, Magnetic coupling in $Y_3Fe_5O_{12}/Gd_3Fe_5O_{12}$ heterostructures, Phys. Rev. Appl. 16 (2021) 014047.

[20] Q. Shao, A. Grutter, Y. Liu, G. Yu, C.-Y. Yang, D.A. Gilbert, E. Arenholz, P. Shafer, X. Che, C. Tang, M. Aldosary, A. Navabi, Q.L. He, B.J. Kirby, J. Shi, K.L. Wang, Exploring interfacial exchange coupling and sublattice effect in heavy metal/ferrimagnetic insulator heterostructures using Hall measurements, x-ray magnetic circular dichroism, and neutron reflectometry, Phys. Rev. B 99 (2019) 104401.

[21] J.J. Bauer, P. Quarterman, A.J. Grutter, B. Khurana, S. Kundu, K.A. Mkhoyan, J.A. Borchers, C.A. Ross, Magnetic proximity effect in magnetic-insulator/heavy-metal heterostructures across the compensation temperature, Phys. Rev. B 104 (2021) 094403.

[22] B.W. Dong, J. Cramer, K. Ganzhorn, H.Y. Yuan, E.J. Guo, S.T.B. Goennenwein, M. Klaui, Spin Hall magnetoresistance in the non-collinear ferrimagnet GdIG close to the compensation temperature, J. Phys. Condens. Matter. 30 (2018) 035802.

[23] L. Liu, Z. Fan, Z. Chen, Z. Chen, Z. Ye, H. Zheng, Q. Zeng, W. Jia, S. Li, N. Wang, J. Liu, L. Ma, T. Lin, M. Qiu, S. Li, P. Han, J. Shi, H. An, Spin–orbit torques in heavy metal/ferrimagnetic insulator bilayers near compensation, Appl. Phys. Lett. 119 (2021) 052401.

[24] W. Zhang, M.B. Jungfleisch, W. Jiang, Y. Liu, J.E. Pearson, S.G.E.t. Velthuis, A. Hoffmann, F. Freimuth, Y. Mokrousov, Reduced spin-Hall effects from magnetic proximity, Phys. Rev. B 91 (2015) 115316.

[25] S. Ding, Z. Liang, C. Yun, R. Wu, M. Xue, Z. Lin, A. Ross, S. Becker, W. Yang, X. Ma, D. Chen, K. Sun, G. Jakob, M. Kläui, J. Yang, Anomalous Hall effect in magnetic insulator heterostructures: Contributions from spin-Hall and magnetic-proximity effects, Phys. Rev. B 104 (2021) 224410.

[26] W. Amamou, I.V. Pinchuk, A.H. Trout, R.E.A. Williams, N. Antolin, A. Goad, D.J. O'Hara, A.S. Ahmed, W. Windl, D.W. McComb, R.K. Kawakami, Magnetic

proximity effect in Pt/CoFe2O4 bilayers, Phys. Rev. Mater. 2 (2018) 011401.

[27] Y.K. Liu, J.M. Liang, H.F. Wong, S.M. Ng, C.L. Mak, C.W. Leung, Strain dependent structure and anomalous Hall effect in Pt/$Tb_3Fe_5O_{12}$/$Ga_3Gd_5O_{12}$ heterostructure grown on $Y_3Al_5O_{12}$ substrates, J. Magn. Magn. Mater. 536 (2021).

[28] H. Fuess, G. Bassi, M. Bonnet, A. Delapalme, Neutron scattering length of terbium structure refinement and magnetic moments of terbium iron garnet, Solid State Commun. 18 (1976) 557-562.

[29] J.M. Liang, X.W. Zhao, S.M. Ng, H.F. Wong, Y.K. Liu, C.L. Mak, C.W. Leung, Observation of interfacial antiferromagnetic coupling between ferrimagnetic garnet thin films, IEEE Trans. Magn. 58 (2022) 1-5.

[30] S. Mokarian Zanjani, M.C. Onbaşlı, Predicting new iron garnet thin films with perpendicular magnetic anisotropy, J. Magn. Magn. Mater. 499 (2020) 166108.

[31] S.M. Wu, J.E. Pearson, A. Bhattacharya, Paramagnetic spin seebeck effect, Phys. Rev. Lett. 114 (2015) 186602.

[32] V.H. Ortiz, M. Aldosary, J. Li, Y. Xu, M.I. Lohmann, P. Sellappan, Y. Kodera, J.E. Garay, J. Shi, Systematic control of strain-induced perpendicular magnetic anisotropy in epitaxial europium and terbium iron garnet thin films, APL Mater. 6 (2018) 121113.

[33] R. Yadav, A. Bake, W.T. Lee, Y.-K. Liu, D.R.G. Mitchell, X.-R. Yang, D.L. Cortie, K.-W. Lin, C.W. Leung, Interfacial spin structures in Pt/$Tb_3Fe_5O_{12}$ bilayer films on $Gd_3Ga_5O_{12}$ substrates, Phys. Rev. Mater. 7 (2023) 124407.

[34] A. Mitra, O. Cespedes, Q. Ramasse, M. Ali, S. Marmion, M. Ward, R.M.D. Brydson, C.J. Kinane, J.F.K. Cooper, S. Langridge, B.J. Hickey, Interfacial origin of the magnetisation suppression of thin film yttrium iron garnet, Sci. Rep. 7 (2017) 11774.

[35] Y.M. Lu, Y. Choi, C.M. Ortega, X.M. Cheng, J.W. Cai, S.Y. Huang, L. Sun, C.L. Chien, Pt magnetic polarization on $Y_3Fe_5O_{12}$ and magnetotransport characteristics, Phys. Rev. Lett. 110 (2013) 147207.

[36] H. Chen, D. Cheng, H. Yang, D. Wang, S. Zhou, Z. Shi, X. Qiu, Magnetization

switching induced by magnetic field and electric current in perpendicular TbIG/Pt bilayers, Appl. Phys. Lett. 116 (2020) 112401.

[37] Y.J. Hong, J.S. Kum, I.B. Shim, C.S. Kim, Spin rotation at compensation point studies of $Tb_3Fe_5O_{12}$ by Mössbauer spectroscopy, IEEE Trans. Magn. 40 (2004) 2808-2810.

[38] Y. Li, D. Zheng, C. Liu, C. Zhang, B. Fang, A. Chen, Y. Ma, A. Manchon, X. Zhang, Current-induced magnetization switching across a nearly room-temperature compensation point in an insulating compensated ferrimagnet, ACS Nano 16 (2022) 8181-8189.

[39] E.R. Rosenberg, L. Beran, C.O. Avci, C. Zeledon, B. Song, C. Gonzalez-Fuentes, J. Mendil, P. Gambardella, M. Veis, C. Garcia, G.S.D. Beach, C.A. Ross, Magnetism and spin transport in rare-earth-rich epitaxial terbium and europium iron garnet films, Phys. Rev. Mater. 2 (2018) 094405.

[40] C.H. Du, H.L. Wang, Y. Pu, T.L. Meyer, P.M. Woodward, F.Y. Yang, P.C. Hammel, Probing the spin pumping mechanism: exchange coupling with exponential decay in $Y_3Fe_5O_{12}$/barrier/Pt heterostructures, Phys. Rev. Lett. 111 (2013) 247202.

[41] W. Chen, M. Sigrist, D. Manske, Spin Hall effect induced spin transfer through an insulator, Phys. Rev. B 94 (2016) 104412.

[42] S.M. Benford, G.V. Brown, T-S diagram for gadolinium near the Curie temperature, J. Appl. Phys. 52 (1981) 2110-2112.

[43] A. Kumar, R. Kumar, N. Verma, A.V. Anupama, H.K. Choudhary, R. Philip, B. Sahoo, Effect of the band gap and the defect states present within band gap on the non-linear optical absorption behaviour of yttrium aluminium iron garnets, Opt. Mater. 108 (2020) 110163.

[44] K. Ghimire, H.F. Haneef, R.W. Collins, N.J. Podraza, Optical properties of single-crystal $Gd_3Ga_5O_{12}$ from the infrared to ultraviolet, Phys. Status Solidi B 252 (2015) 2191-2198.

[45] Q. Shao, C. Tang, G. Yu, A. Navabi, H. Wu, C. He, J. Li, P. Upadhyaya, P. Zhang,

S.A. Razavi, Q.L. He, Y. Liu, P. Yang, S.K. Kim, C. Zheng, Y. Liu, L. Pan, R.K. Lake, X. Han, Y. Tserkovnyak, J. Shi, K.L. Wang, Role of dimensional crossover on spin-orbit torque efficiency in magnetic insulator thin films, Nat. Commun. 9 (2018) 1-7.

[46] M.J. Roos, P. Quarterman, J. Ding, M. Wu, B.J. Kirby, B.L. Zink, [1] S. Meyer, M. Althammer, S. Geprägs, M. Opel, R. Gross, S.T.B. Goennenwein, Temperature dependent spin transport properties of platinum inferred from spin Hall magnetoresistance measurements, Appl. Phys. Lett. 104 (2014) 242411.

Chapter 5 Tunable magnetization compensation in TbIG/EuIG bilayer system

In REIG/HM systems with magnetization compensation, spin magnetotransport control can be achieved not only through interface modifications, but also by adjusting the T_{comp}. In this Chapter, a bilayer REIGs system is constructed to regulate T_{comp} of the bulk TbIG, and the importance of compensation temperature on spin transport is explored.

5.1 Introduction

The spin magnetotransport behavior of REIG/HM systems have been widely studied especially for YIG [1-5], because the low damping in YIG is very suitable for exploring spin phenomena like SHE, ISHE, SSE, etc. [1, 6-13]. A significant difference between TbIG (as well as DyIG and GdIG) and YIG is that the former materials exhibit magnetization compensation behavior [14-19], which provides additional options for regulating the spin transport of the REIG/HM system.

As mentioned in Chapter 2, the magnetization compensation behavior of REIG is due to the competition of magnetic moments between RE and Fe. Breaking this competitive balance means that the T_{comp} can be controlled and that controllable spin transport behavior can be achieved.

Recently, the magnetization compensation behavior of REIGs with PMA have been observed through R_{AHE}-H loops and analyzed by polarized neutron reflectometry (PNR) [16, 20-22]. AHE studies have also found that the stress of single-layer REIG varies with thickness, which could lead to variations in T_{comp} [23].

As discussed in Chapter 4, two R_{AHE}^{0} sign-flipping events have been observed in TbIG/Pt system [14, 24, 25], and such a phenomenon is common in other REIG/HM systems with compensation behavior [18, 26]. As explained before, one of the R_{AHE}^{0} sign-flipping events corresponds to T_{comp}, and another is related to competing interface

effects (MPE and AHE) [20, 27, 28].

Previous studies on the AHE behavior of REIGs were predominantly based on single-layer garnet films, including the regulation of magnetization compensation. Less attention has been paid to the impact of films composed of multiple REIGs on spin transport. Although some previous studies have attempted to study spin Hall magnetotransport using the magnon valve structure such as YIG/NiO/YIG [29, 30], there is a huge lattice mismatch between antiferromagnetic NiO and YIG, which would lead to poor crystal quality of the upper garnet and potentially suppressed spin transport. For a multilayered structure composed of REIGs with similar crystal structures, it is possible to achieve regulation of compensation behavior under high crystal quality, which is worth exploring.

To achieve controllable magnetization compensation behavior, TbIG is used in this Chapter as the basis and is combined with another REIG (EuIG) to construct a bilayer system for AHE analysis. In this bilayer system, the thickness of EuIG is changed while the TbIG thickness is fixed, in order to investigate the EuIG thickness-dependence of spin transport behavior.

Table 5-1 Lattice constants and T_{comp} of materials used in the study

Garnet	Lattice parameter (Å)	T_{comp} (K)
TbIG	12.436	246
EuIG	12.500	/
GGG	12.376	/

The selection of EuIG is based on the following considerations. First, lattice matching is an important criterion in the selection of film material. Table 5-1 shows the basic structural properties of GGG, EuIG, and TbIG. All these materials have a garnet structure, with the lattice constant of EuIG (12.500 Å) [31] close to TbIG (12.436 Å) [32]. The small lattice mismatch between them implies good epitaxial quality of the resultant films. Besides, the bilayer system needs to maintain consistent anisotropy

direction to ensure stable magnon transport [33]. Previous work suggested that both EuIG and TbIG can maintain PMA upon epitaxial growth on GGG (111) [34]. Moreover, EuIG has no T_{comp} [35], which helps the observation in changes of compensation behavior in the TbIG/EuIG system.

5.2 Experimental details

For film deposition, a series of GGG (111)/TbIG (30 nm)/EuIG (5-20 nm) samples were prepared by PLD. Fig. 5.1 shows the specific deposition sequence of GGG/TbIG/EuIG heterostructures. Besides, single layers of TbIG and EuIG were also deposited as control samples. Specific experimental parameters can refer to the descriptions in Chapter 4, which include substrate pre-treatment for smooth surfaces, thin film deposition procedures in PLD chamber, *ex-situ* Pt deposition by magnetron sputtering and subsequent Hall bar etching process. Among these, the deposition parameters of EuIG are identical with those of TbIG.

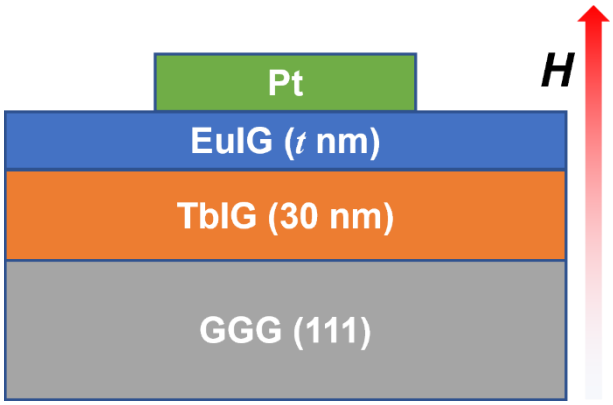

Fig. 5.1 Schematic diagram of deposition sequence of the Hall device.

For structural characterization, XRD (Rigaku SmartLab) was used to study the crystallinity and epitaxy quality of this series of samples. The surface roughness was analyzed through AFM (Asylum 3D infinity). The structural arrangement at the atomic level, including element distribution and interplanar spacing, was characterized by TEM (JEM-F200). Magnetic and electrical properties, as well as transport measurements, were performed using VSM (Lakeshore) and PPMS (Quantum Design).

5.3 Results and discussions

5.3.1 Structural characterization

Fig. 5.2(a) shows the surface morphology of the TbIG (30 nm)/EuIG (10 nm) bilayer by AFM. A roughness of about 0.34 nm implies that the bilayer growth maintains atomic-level flatness. The XRD 2θ scan of the series TbIG (30 nm)/EuIG (5, 10, 15, 20 nm) samples are presented in Fig. 5.2. Due to the proximity of the (444) peaks of EuIG and TbIG, their 2θ peaks partially overlap at around 50°, making it difficult to distinguish the specific peak positions of different layers. However, it is evident that as the thickness of EuIG layer increases, the peak width of the bilayer films also gradually increases, which can be attributed to the increase in EuIG thickness causing a change in stress between TbIG and EuIG, making the stress on TbIG more complex.

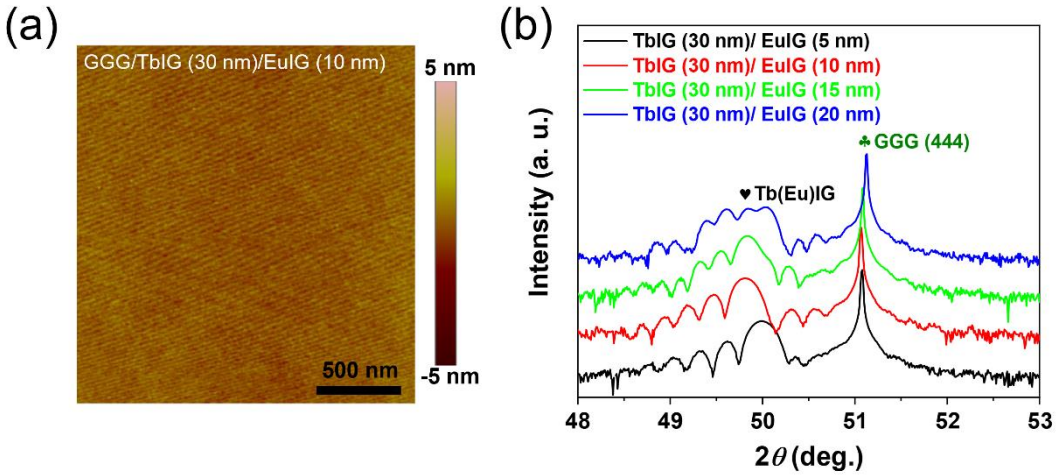

Fig. 5.2 (a) AFM image of bilayer film TbIG (30 nm)/EuIG (10 nm). (b) XRD of TbIG (30 nm)/EuIG sample series.

Single layers of TbIG and EuIG were also prepared as control. Fig. 5.3(a) shows the rocking curves of TbIG (30 nm) and EuIG (10 nm) samples. The FWHM for single-layer thin films are 0.071° and 0.082°, respectively, indicating that both garnet materials have similar crystalline quality with low mosaic spread on GGG substrates. Fig. 5.3(c) presents the XRD of TbIG (30 nm) and EuIG (10 nm), as well as the corresponding

TbIG (30 nm)/EuIG (10 nm) bilayer. The 2θ peaks of single-layer TbIG and EuIG are 49.9° and 49.61° respectively, and the 2θ value of the bilayer film TbIG (30 nm)/EuIG (10 nm) falls between them (combined 2θ peak is 49.8°). The epitaxial relation of bilayer thin films with substrates can be determined by ϕ scan as presented in Fig. 5.3(d). The (642) peaks of the bilayer film and substrate show consistent six-fold symmetry, indicating that the bilayer film attains good epitaxial relation with the substrate.

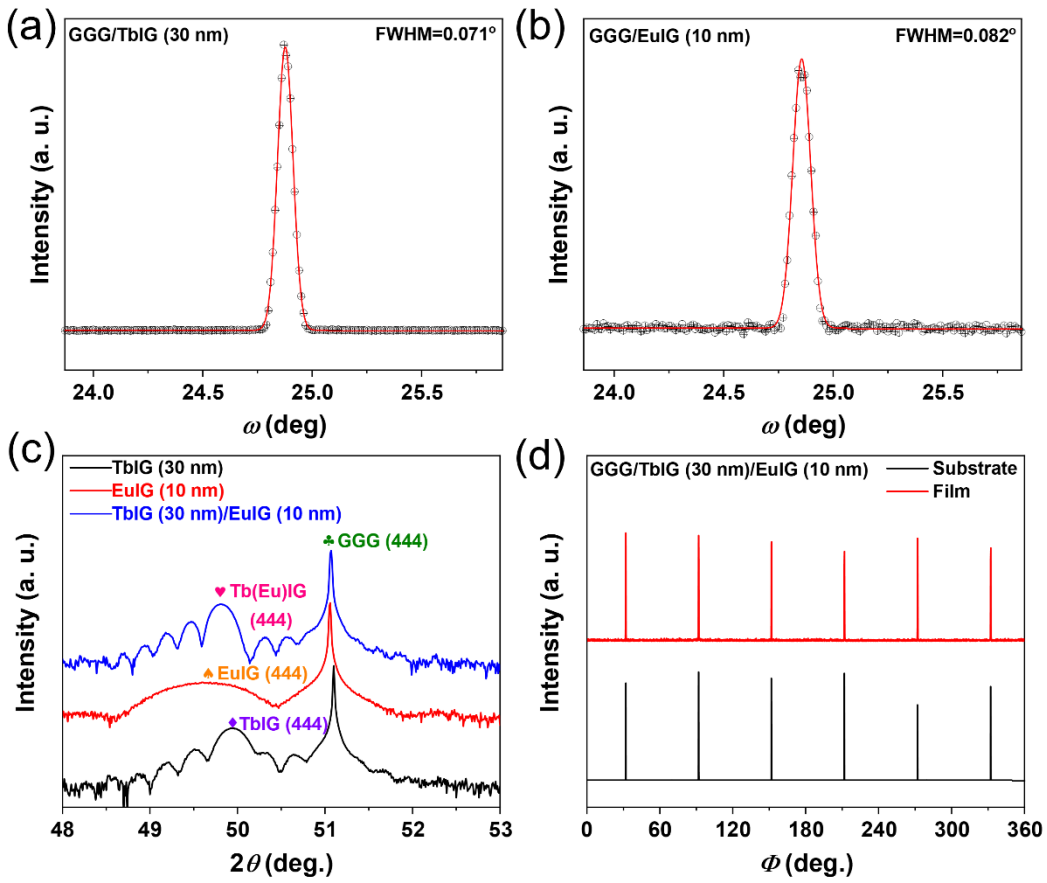

Fig. 5.3 (a) Rocking curve of TbIG (30 nm) and (b) EuIG (10 nm) samples. (c) Comparison of XRD for single-layer TbIG (30 nm), EuIG (10 nm), and bilayer TbIG (30 nm)/EuIG (10 nm) samples. (d) Comparison of ϕ scan between substrate and bilayer film (642) peaks.

The actual thickness values of the bilayer films were confirmed by STEM images and is presented in Fig. 5.4(a). Measurement confirms that the thickness of TbIG and EuIG in sample TbIG (30 nm)/EuIG (10 nm)/Pt meets expectations, indicating the

stability of the film growth process by PLD. Good epitaxial growth was also confirmed through atomic arrangement in Fig. 5.4(b), with no obvious dislocation observed throughout the whole range, consistent with the ϕ scan results.

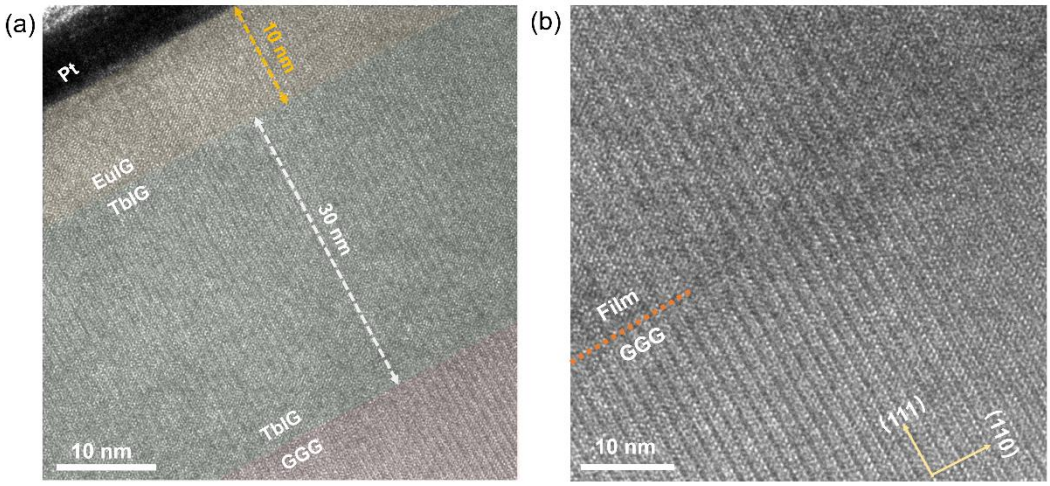

Fig. 5.4 (a) Cross-sectional STEM of TbIG (30 nm)/EuIG (10 nm)/Pt. Different colors are used to distinguish different layers. (b) Cross-sectional image of substrate/TbIG interface.

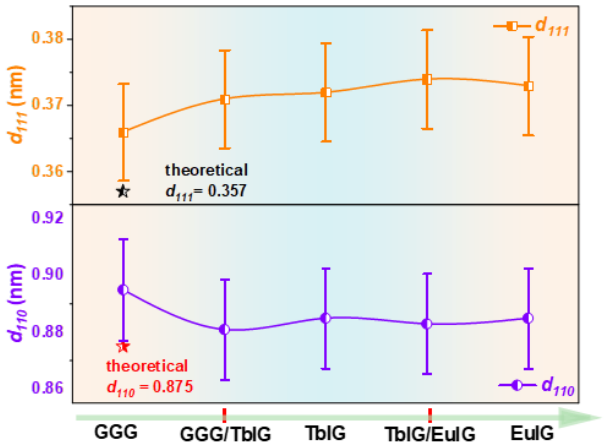

Fig. 5.5 Lattice plane spacing value from GGG to EuIG as extracted from the Fig.5.4(a). The d_{111} and d_{110} are highlighted in yellow and purple plots, respectively. The green arrow represents the sequence from the substrate (GGG) to the top film (EuIG), and the red line represents the interfaces.

The stress changes caused by lattice mismatch are reflected through the interplanar

spacing. Fig. 5.5 shows the variation of lattice plane spacing in the (111) (out-of-plane) and (110) (in-plane) directions from the substrate to the EuIG layer, as extracted from Fig. 5.4. The minor mismatch between the substrate and the film results in insignificant changes in d_{111} and d_{110}, both of which are close to the bulk values of GGG substrate (0.357 nm and 0.875 nm, respectively). Although there is a possibility of interdiffusion at the GGG/TbIG and TbIG/EuIG interface, the variations in d_{111} and d_{110} are very small. The impact of mismatch on the overall crystal structure seems to be negligible within the error range, which means that the films maintain good epitaxial growth.

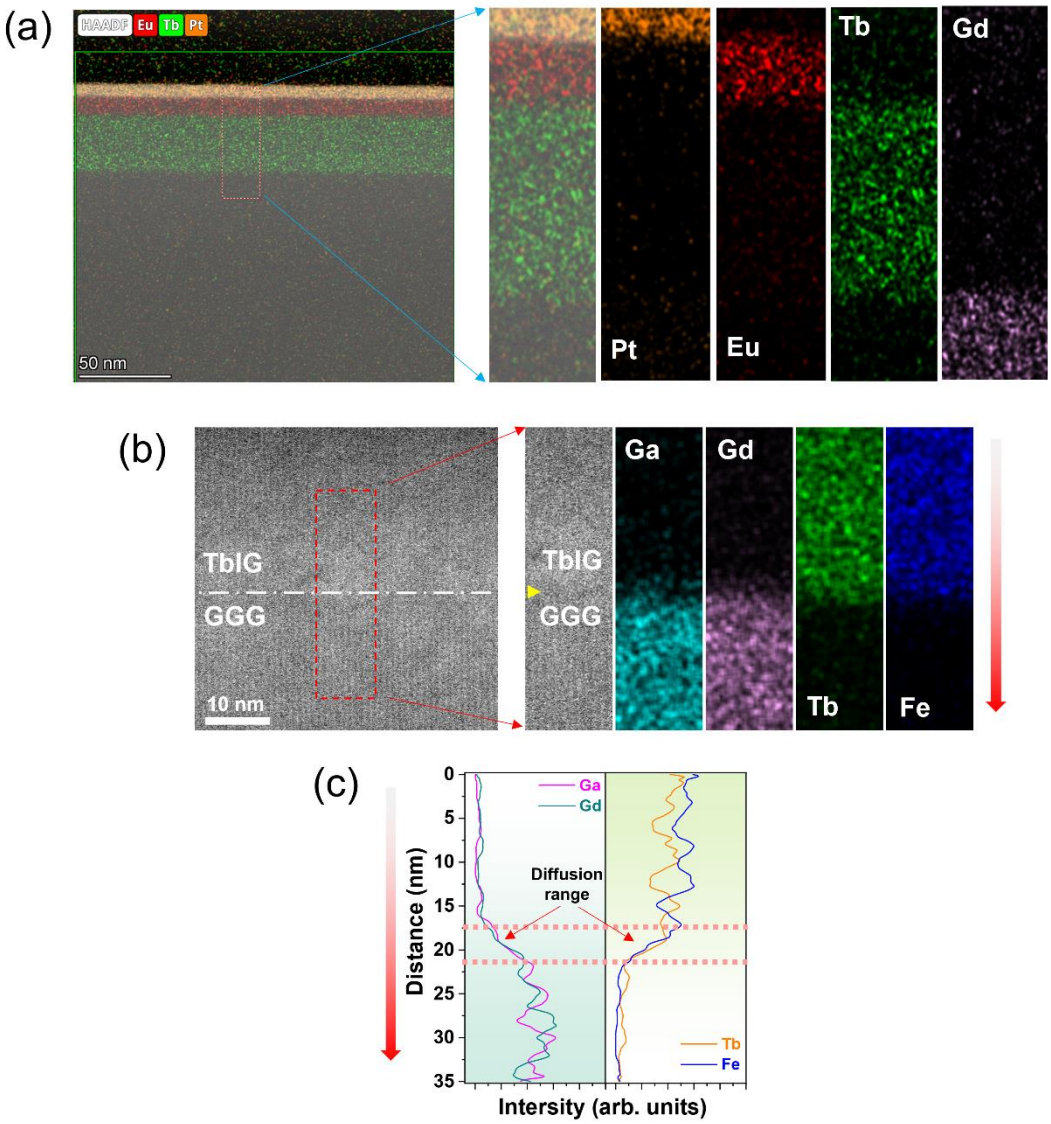

Fig. 5.6 (a) EDX mapping of overall and individual elements for TbIG (30 nm)/EuIG (10 nm)/Pt specimen. (b) STEM image of the substrate/film interface. The enlarged

range was extracted for EDX analysis. (c) Line scan indicates the variation of intensity for different elements with the distance from the sample top surface to substrate. Diffusion range refers to the region of interfacial mutual diffusion between TbIG and EuIG films.

As REIG deposition occurs at high-temperatures, interface diffusion has become a common issue in PLD epitaxial growth [36-38]. Fig. 5.6(a) shows EDX mapping of overall and individual elements for the TbIG (30 nm)/EuIG (10 nm)/Pt specimen. The boundary of each interface (GGG/TbIG, TbIG/EuIG, and EuIG/Pt interface) can be easily distinguished through EDX scanning. Mapping of individual element distribution indicates the presence of chemical diffusion rather than sharp interfaces, and the phenomena is similar with the work reported by others [37, 39].

The cross-sectional STEM in Fig. 5.6(b) shows the boundary between the substrate and the film. The red dashed rectangle in the left image is selected to observe the interfacial diffusion of different elements, and the line scan results are shown in Fig. 5.6(c). The interdiffusion range across the GGG/TbIG interface is approximately 4 nm. Such interdiffusion is expected to occur in all samples of the series. Considering that the thickness of TbIG (30 nm) is much larger than the diffusion distance, interfacial diffusion is not expected to affect the observation of changes in spin transport and magnetic compensation behavior in the REIG bilayer structure.

5.3.2 Magnetic transport characterization

In previous studies, researchers observed that TbIG and EuIG epitaxially grown on GGG substrates exhibit PMA [14, 40, 41]. The PMA, as an effective means of observing certain special phenomena such as SOT and AHE [24, 42], is equally important in this study. To verify the out-of-plane magnetization easy axis is maintained in the TbIG/EuIG bilayers, external magnetic fields parallel to and perpendicular to the TbIG/EuIG sample are applied to obtain hysteresis loops. Fig. 5.7 compares the magnetization curves measured in two directions at 300 K. The normalized *M-H* plots

show square and hysteretic behavior with the field applied perpendicular to the sample surface, indicating that PMA is maintained in the bilayer structure.

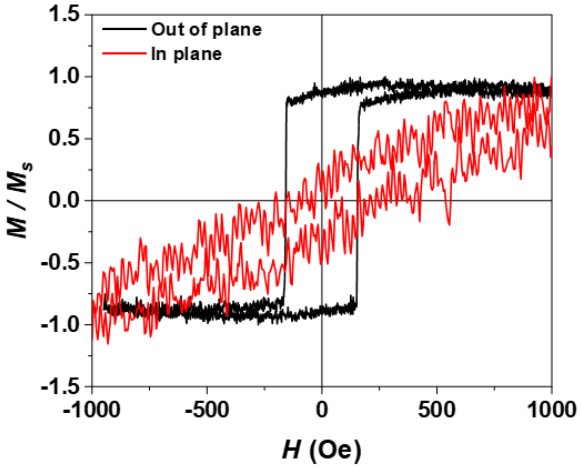

Fig. 5.7 Comparisons of *M*-*H* loops of TbIG (30 nm)/EuIG (10 nm) sample under in-plane and out-of-plane external fields at room temperature.

5.3.3 Magnetotransport in single-layer TbIG and EuIG

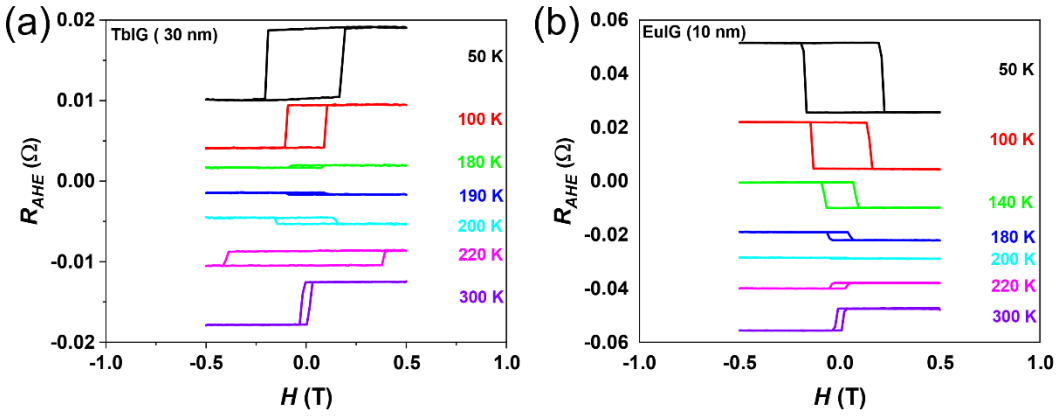

Fig. 5.8 Temperature dependent R_{AHE}-*H* loops of (a) TbIG (30 nm)/Pt and (b) EuIG (10 nm)/Pt.

The R_{AHE}-*H* loops of single-layer TbIG (30 nm)/Pt and GGG/EuIG (10 nm)/Pt samples are first analyzed. Fig. 5.8 shows sharp square loops in both samples under an out-of-plane field. Notice that the R_{AHE} signal undergoes two sign flips in the sample

TbIG (30 nm)/Pt, the first at around 200-220 K and the second one between 180-190 K. Meanwhile, only one R_{AHE} sign flip occurs in EuIG (10 nm)/Pt at around 200-220 K. For clear comparison of the two single-layer samples, temperature-dependent H_c and R_{AHE}^0 are extracted from R_{AHE}-H loops and are shown in Fig. 5.9.

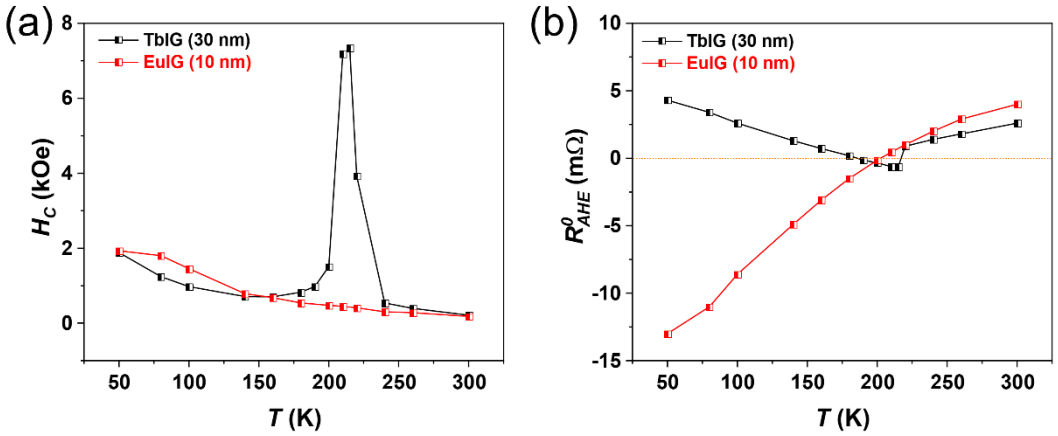

Fig. 5.9 Comparisons of H_c (a) and R_{AHE}^0 (b) between TbIG (30 nm)/Pt and EuIG (10 nm)/Pt.

Fig. 5.9 shows a divergent H_c in TbIG (30 nm)/Pt sample at ~218 K. As mentioned in Chapter 4, the divergent behavior of H_c indicates the occurrence of T_{comp}. Also, the R_{AHE}^0 signal undergoes its first sign flip at the same temperature. As temperature goes below T_{comp}, H_c of TbIG (30 nm)/Pt is gradually reduced before climbing up again. At the same time, the sign of R_{AHE}^0 flips again at ~185 K. For sample GGG/EuIG (10 nm)/Pt, the H_c and R_{AHE}^0 changes are completely different, with no divergence of H_c observed and only one R_{AHE}^0 sign-flip event at around 200 K.

As interpreted in Chapter 4, the divergent behavior of H_c in TbIG/Pt is attributed to the antiparallel alignment of Tb^{3+} and Fe^{3+} moments. The magnetic moments with different temperature dependencies are completely cancelled at T_{comp} [23, 43], resulting in a sudden drop in Zeeman energy and accompanied by a divergent H_c [44]. For the first cross-over point (T_{comp}) in R_{AHE}^0, the sign reversal of R_{AHE}^0 takes places in an abrupt manner. This is because the spin Hall transport at the TbIG/Pt interface is dominated by Fe/Pt coupling. As the temperature decreases and crosses T_{comp}, the magnetization direction of Fe^{3+} is switched, resulting in a sudden decrease in R_{AHE}^0 to

a negative value.

Meanwhile, the second R_{AHE}^{0} sign cross-over at T_1 takes place with a gradual variation of R_{AHE}^{0} magnitude, and it is attributed to the competition between interfacial SHE and MPE at TbIG/Pt interface [20, 28]. The MPE-induced AHE, which has a stronger temperature dependence, gradually dominates the interfacial spin Hall transport as temperature drops, until the AHE completely cancels out with SHE-induced AHE at 185 K and R_{AHE}^{0} sign reversal occurs.

The reason for the absence of divergent H_c behavior in single-layer EuIG (10 nm)/Pt can be attributed to the lack of magnetization compensation in EuIG. Eu^{3+} has an angular momentum $J = 0$ at the ground state, which hardly contributes to the magnetic moments [35, 45]. It means that the net magnetic moment is dominated by Fe^{3+} throughout the whole temperature range, excluding the possibility of T_{comp}. But the flipping of R_{AHE}^{0} in EuIG/Pt around T_1 is similar to that in TbIG/Pt, as in both cases the variation of R_{AHE}^{0} is gradual and is attributed to the competitive mechanisms of MPE and SHE.

Interface-dominated R_{AHE} can also be reflected through SMR. Fig. 5.10 demonstrates the testing method of SMR. In the SMR geometry, the current is applied along x axis, while the field H rotates along y-z plane. β is defined as the angle between H and z, with $\beta = 0^o$ indicates that H is pointing towards the positive z-axis.

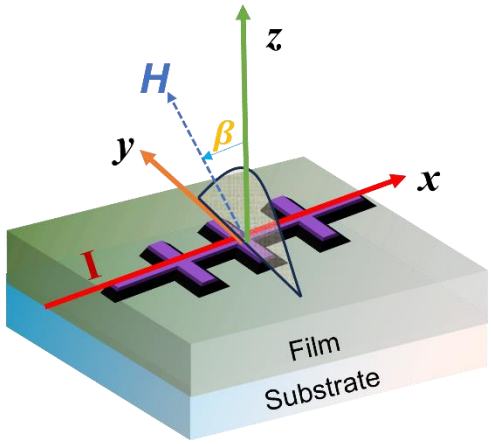

Fig. 5.10 Schematic diagram of SMR measurement. With β changes along the y-z plane.

As mentioned earlier, SMR reflects the relationship between spin polarization and magnetization, and the interaction between the two determines the ability of interfacial spin conduction [2]. The SMR ratio is defined as:

$$SMR = \frac{\Delta R_{xx}}{R_0} = \frac{R_{xx}(\beta) - R_{xx}(\beta = 0)}{R_0} \qquad (5-1)$$

where ΔR_{xx} is the longitudinal resistance difference between $R_{xx}(\beta)$ and $R_{xx}(\beta = 0)$, and R_0 represents the Pt resistance at zero field.

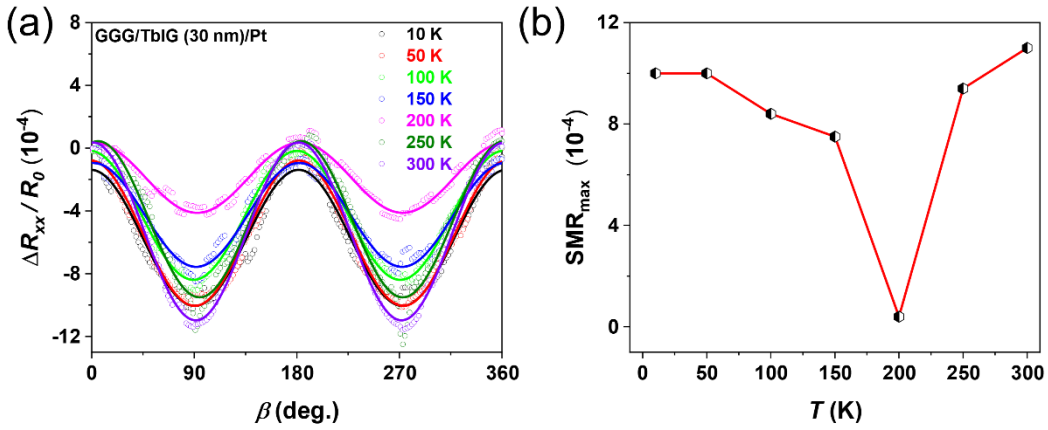

Fig. 5.11 (a) SMR ratio plots of TbIG(30 nm)/Pt at various temperatures. (b) Temperature-dependent SMR amplitude as extracted from (a). The amplitude is defined as the absolute value of $R_{xx}(\beta = 90) - R_{xx}(\beta = 0)$.

Fig. 5.11(a) shows the temperature dependent $\frac{\Delta R_{xx}}{R_0}$ plots of TbIG/Pt, which can be fitted through the correlation function $cos^2\beta$. To analyze the variation of SMR with temperature, the SMR amplitudes in Fig. 5.11(a) are extracted and plotted in Fig. 5.11(b). As the temperature decreases from 300 K to 10 K, the SMR amplitude decreases from 300 K to 200 K and then gradually increases again. The dip of SMR amplitude is close to T_{comp}, once again confirming that the magnetization compensation behavior of sublattices affects the spin transport at the TbIG/Pt interface.

Fig. 5.12 compares the SMR of EuIG/Pt and TbIG/Pt at 10 K and 300 K. The SMR of the two samples shows significant differences at 10 K, but the corresponding SMR behavior at 300 K is similar for the two samples, which is consistent with R_{AHE}^0 results in Fig. 5.9(b). This is because thermal disturbances at elevated temperatures result in

negligible MPE, and the magnetotransport is largely related to SHE-generated spin current within Pt. The minor difference can be attributed to the different thickness between TbIG and EuIG.

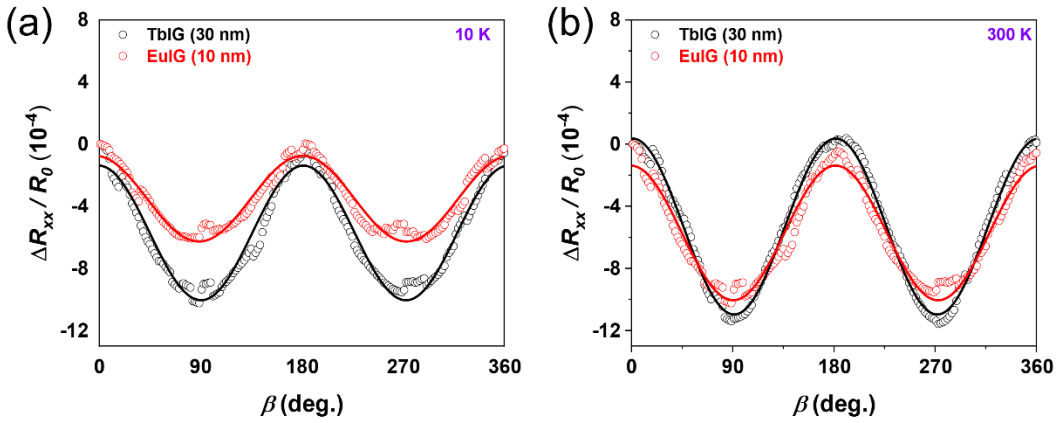

Fig. 5.12 Comparison SMR between TbIG (30 nm)/Pt and EuIG(10 nm)/Pt at 10 K (a) and 300 K(b). All measurements were conducted under an external field of 9 T and current of 0.5 mA.

The significant amplitude differences of SMR at 10 K can be attributed to two effects. One is the different MPE intensity of the two samples. As mentioned in Chapter 4, MPE would dominate the overall spin transport. The situation is comparable with the R_{AHE}^{0} at 10 K [Fig. 5.9 (b)], which also exhibits an obvious difference in amplitude between the two samples. Another factor is related to the temperature dependent spin Hall angle and spin diffusion length [46]. According to the spin-mixing conductance theory in Chapter 2, the spin Hall angle and diffusion length are strongly related to the SMR. Due to the spin Hall angle and diffusion length of Pt are affected by the adjacent ferromagnetic layer, and the magnetic moment difference at 10 K is greater than at 300 K between EuIG and TbIG. Therefore, SMR shows a significant difference at 10 K.

5.3.4 Magnetotransport in bilayer TbIG/EuIG samples

In Chapter 4, MPE and SHE are shown to be affected by the interface quality through the insertion of YAG spacers (Chapter 4), and it was found that the non-

magnetic YAG would affect T_1 but not T_{comp}. In this Chapter, different thicknesses of EuIG are placed on the top of TbIG (fixed 30 nm) to explore the effect of a magnetic spacer between TbIG and Pt.

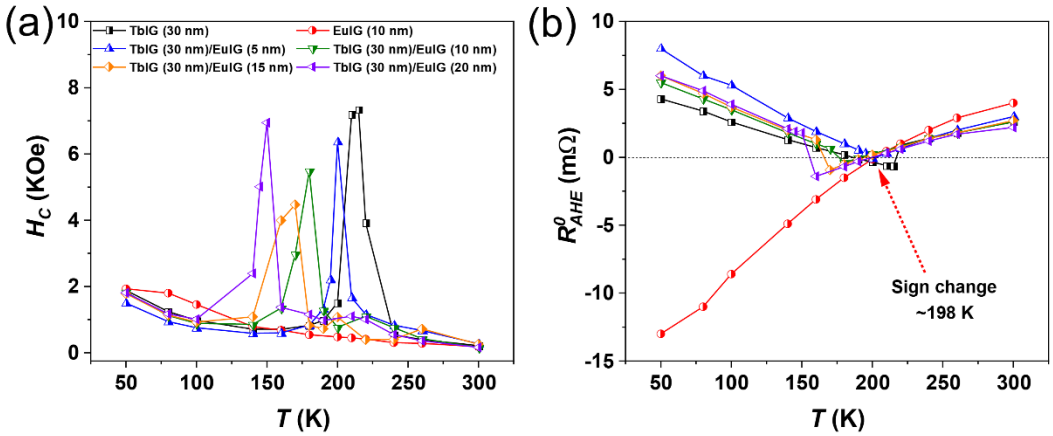

Fig. 5.13 Temperature dependent H_c (a) and R^0_{AHE} (b) for single-layer and bilayer samples.

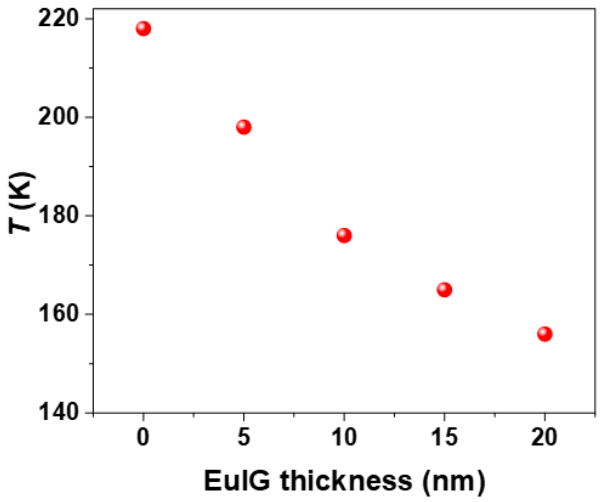

Fig. 5.14 T_{comp} as a function of EuIG thickness in GGG/TbIG (30 nm)/EuIG (t nm)/Pt system.

R_{AHE}-H loops of all bilayer samples were measured, and the corresponding H_c and R^0_{AHE} are extracted. Fig. 5.13 compares the temperature-dependent H_c and R^0_{AHE} of all single and bilayer samples. It can be observed that H_c divergence occurs in all TbIG (30 nm)/EuIG (t nm)/Pt samples, and the divergent temperature of H_c exhibits

significant thickness dependence. The corresponding R_{AHE}^{0} also undergoes an abrupt sign flip at the same temperature as H_c divergence, indicating that all bilayer samples exhibit compensation behavior like single-layer TbIG/Pt, and the T_{comp} is regulated by the thickness of EuIG. The EuIG thickness dependent T_{comp} in GGG/TbIG (30 nm)/EuIG (t nm)/Pt samples are extracted from Fig. 5.13 and is presented in Fig. 5.14. As the thickness of EuIG increases, T_{comp} decreases from ~218 K (without EuIG) to ~156 K (t_{EuIG} = 20 nm), indicating a significant EuIG thickness dependence of T_{comp}.

In addition to the abrupt sign cross-over in R_{AHE}^{0} [Fig. 5.13(b)], another R_{AHE}^{0} sign flip with a more gradual change appears in all bilayer samples, which is attributed to the competition between SHE and MPE. This mechanism has been analyzed in single-layer samples. Interestingly, the second cross-over point T_1 of all bilayer samples is approximately 198 K [Fig. 5.13(b)].

The above results indicate that under the same EuIG/Pt interface, there is no obvious change in the exchange energy of the EuIG/Pt interface. Hence, the MPE and SHE of the interface are almost unaffected. However, T_{comp} of TbIG is modulated by adjacent EuIG, which could be attributed to the coupling between TbIG and EuIG.

To analyze the mechanism of T_{comp} variation in the bilayer samples, two possible TbIG/EuIG coupling models are proposed. Fig. 5.15(a) and (b) displays two of the possible sublattice arrangements in the TbIG/EuIG sample. For the convenience of analyzing the coupling effect, only parallel or antiparallel magnetic moments alignment situations are considered. Due to the antiparallel relationship between *a*-site and *d*-site Fe moments, they cancel each other and results in a net magnetic moment of Fe. Therefore, only the net moment of Fe in each REIG layer is considered. Fig. 5.15(a) assumes that Fe ions in TbIG and EuIG (define as Fe_{TbIG} and Fe_{EuIG}) are ferromagnetic coupled, i.e. the moments of Fe_{TbIG} and Fe_{EuIG} are aligned in the same direction, while Fig. 5.15(b) assumes that Fe_{TbIG} and Fe_{EuIG} exhibit antiferromagnetic alignment.

To analyze the specific coupling situation, the internal magnetization variation of the bilayer sample with temperature is analyzed. As shown in Fig. 5.13(b), all GGG/TbIG (30 nm)/EuIG (t nm)/Pt samples exhibit positive R_{AHE}^{0} at temperatures

above T_{comp}. At this point, the magnetizations of TbIG and EuIG are both dominated by *d*-site Fe^{3+}, and the net magnetization of each layer follows the direction of the external field [Fig. 5.15 (c)]. The similar R_{AHE}^{0} for both single-layer TbIG/Pt and bilayer TbIG/EuIG/Pt samples above T_{comp} confirms this interpretation.

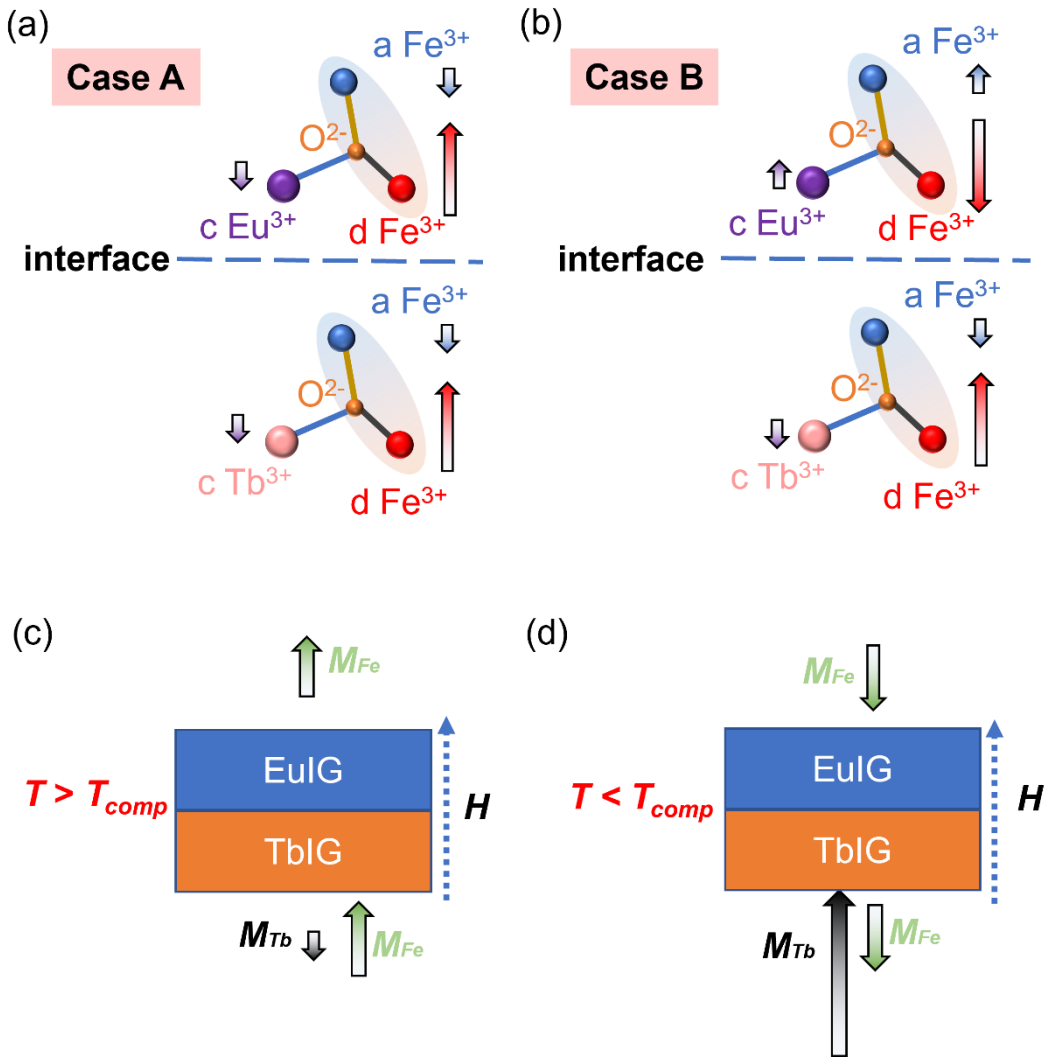

Fig. 5.15 Schematic diagram of possible interface coupling between Fe in TbIG/ EuIG interface: (a) ferromagnetic coupling; and (b) antiferromagnetic coupling. The model explains the direction of magnetic moments in each layer below (c) and above (d) T_{comp} in bilayer samples.

As the temperature goes down and crosses T_{comp}, although the second R_{AHE}^{0} cross-over appears in all TbIG (30 nm)/EuIG (*t* nm)/Pt samples, the overall magnetization in

each layer is different. As mentioned earlier, the *d*-site Fe^{3+} dominates the EuIG magnetization over the whole temperature range. When T_{comp} occurs in the bilayer films, the Fe^{3+} magnetic moments reorient, indicating a reversal of the net magnetization direction of EuIG layer [Fig. 5.15(c-d)]. However, the Tb^{3+} sublattice in TbIG layer dominates below T_{comp}. As the sublattice is reoriented, the total magnetization of the TbIG layer points in the opposite direction with the EuIG layer.

From the above analysis, it can be concluded that when Case A [Fig. 5.15 (a)] occurs, the ferromagnetically-coupled Fe_{TbIG}-Fe_{EuIG} point in the same direction, indicating a larger Tb^{3+} sublattice moment (M_{Tb}) is needed to offset the additional Fe^{3+} moment arising from the EuIG layer. A lower temperature is required to achieve complete cancellation of M_{Tb} and M_{Fe} in TbIG/EuIG bilayer system, resulting in a decrease in T_{comp}. This implies an increase in the thickness of EuIG will lead to a decrease in the T_{comp} of the bilayer system. The results in Fig. 5.14 support this explanation. Moreover, Fig. 5.15 (a) shows the Fe_{TbIG} and Fe_{EuIG} are parallel, consistent with the magnetization direction of sublattices described in Fig. 5.15 (c-d). This indicates that case A is reasonable.

On the other hand, if case B [Fig. 5.15 (b)] were true, the antiparallel Fe_{TbIG}-Fe_{EuIG} will cause the magnetization of TbIG layer and EuIG layer show opposite alignment at above T_{comp}. This is inconsistent with the descriptions in Fig. 5.14 and Fig. 5.15(b).

From the above discussion, it can be suggested that the ferromagnetic coupling of Fe ions in TbIG and EuIG leads to the regulation of T_{comp} with varying EuIG thickness in TbIG/EuIG/Pt system. Similar exchange coupling of bilayer system was also observed in YIG/GdIG with in-plane easy axis [47], which proves the validity of the hypothesis (Case A).

The ferromagnetic coupling between TbIG and EuIG is only inferred based on AHE results and theoretical models. To verify the authenticity of TbIG/EuIG coupling, a non-magnetic insulator between the TbIG and EuIG layers (i.e. TbIG/spacer/EuIG structure) is considered. As mentioned in Chapter 4, an ultrathin non-magnetic YAG can completely block the spin transport between TbIG and Pt. Therefore, a 2-nm YAG

spacer is inserted between TbIG and EuIG (i.e. TbIG/YAG/EuIG) to verify the existence of ferromagnetic coupling in the TbIG/EuIG bilayer films.

5.3.5 The effect of YAG spacer on TbIG/EuIG exchange coupling

As mentioned above, another sample with YAG insertion layer was prepared. Fig. 5.16(a) illustrates the non-magnetic YAG as inserted at the TbIG/EuIG interface, avoiding direct contact between TbIG and EuIG. The corresponding temperature dependent R_{AHE}-H loops of GGG/TbIG (30 nm)/YAG (2 nm)/EuIG (10 nm)/Pt sample are shown in Fig. 5.16(b). It is evident that the square loops are still maintained, indicating that the ultrathin YAG does not affect the overall PMA. Interestingly, only one R_{AHE}^{0} sign flipping is observed with changing temperature, which is similar to the R_{AHE}^{0} of single-layer EuIG/Pt samples.

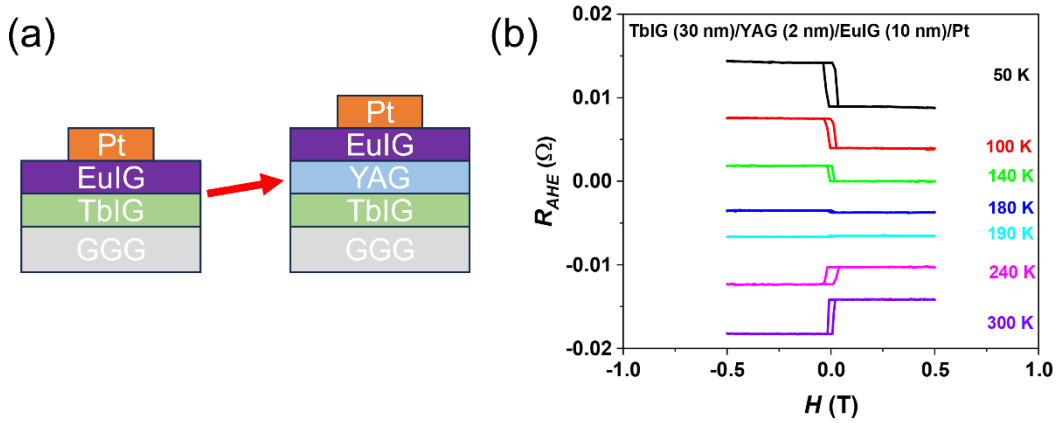

Fig. 5.16 (a) Schematic showing the YAG insert layer between EuIG and TbIG. (b) Temperature-dependent R_{AHE}-H loops of TbIG/YAG/EuIG/Pt sample.

H_c and R_{AHE}^{0} of GGG/TbIG (30 nm)/YAG (2 nm)/EuIG (10 nm)/Pt sample are extracted from Fig. 5.16(b) and compared with GGG/EuIG (10 nm)/Pt and GGG/TbIG (30 nm)/EuIG (10 nm)/Pt samples. As shown in Fig. 5.17 (a), only bilayer sample shows divergent H_c, indicating that with the YAG insertion the magnetization contribution from bottom TbIG was suppressed by the non-magnetic YAG spacer. Due to the lack of effective coupling between TbIG and EuIG, T_{comp} disappears from the H_c

vs. *T* plot.

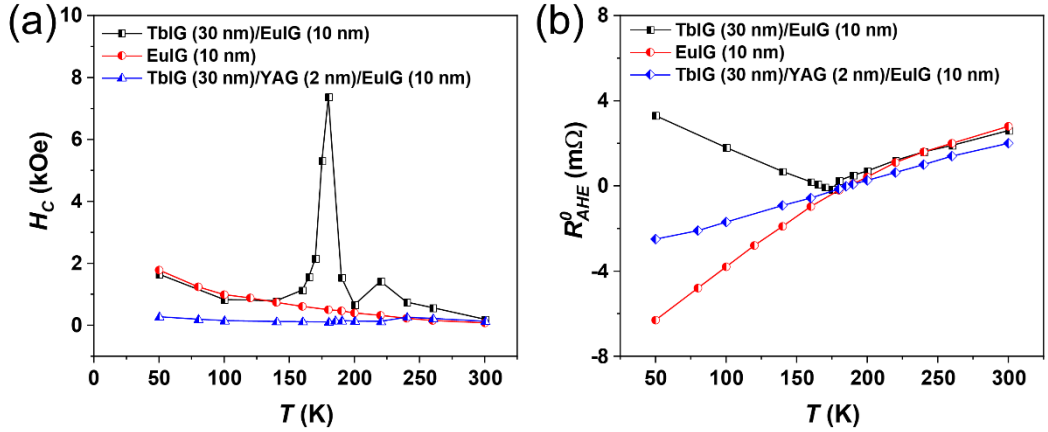

Fig. 5.17 Temperature dependence of H_c (a) and R^0_{AHE} (b) for EuIG/Pt (red circle), TbIG/EuIG/Pt (black square), and TbIG/YAG/EuIG/Pt (blue triangle) samples.

Another noteworthy point is that samples with YAG spacer exhibit the same trend as single-layer EuIG/Pt, including the same cross-over of R^0_{AHE} [Fig. 5.15 (b)]. This indicates that the TbIG at the bottom layer cannot affect the EuIG at the top of the trilayer sample, as the exchange coupling between TbIG and EuIG is disrupted. The difference in R^0_{AHE} amplitude between GGG/TbIG (30 nm)/YAG (2 nm)/EuIG (10 nm)/Pt and GGG/EuIG (10 nm)/Pt samples may be attributed to the slight lattice mismatch between YAG and EuIG, resulting in inconsistent quality at EuIG/Pt interface. However, the minor difference does not affect the overall trend of in R^0_{AHE} variations. The insertion of YAG at the TbIG/EuIG interface indicates that the coupling between TbIG and EuIG exists, and the exchange coupling can be tuned by an ultrathin spacer.

5.3.6 R_{AHE}-H loops of TbIG/EuIG films at 10 K

Interestingly, it was also found that the coupling of TbIG/EuIG is not stable, but exhibits complex coupling at very low temperatures. Fig. 5.18 compares the R_{AHE}-H loop of the four TbIG (30 nm)/EuIG (*t* nm)/Pt samples. The test was conducted at 10 K with an external field of 2 T. It is noticed that R_{AHE} at 10 K exhibits multiple loop

behavior when a sufficiently large field is applied, especially in EuIG samples with thickness above 10 nm [Fig. 5.18(b)]. All the samples show virtually identical R_{AHE} loops around the field range of ± 0.5 T. However, when the external field increases to 2 T, two additional symmetric loops appear as the EuIG thickness reaches 15 nm. The offset of these loops from zero field is about 12000 Oe for the sample with EuIG (15 nm), which gradually shifts to 8000 Oe for EuIG (20 nm).

The pair of offset loops may arise from the formation of interfacial Fe_{TbIG}-Fe_{EuIG} antiferromagnetic coupling. Under specific conditions, the ferromagnetic coupling between EuIG and TbIG can be decoupled and reversed. With a sufficiently large external field and at low temperatures, the top EuIG layer can overcome the interface exchange coupling energy and gradually dominates the whole R_{AHE} sign switching. The inverse relation between the offset field and EuIG thickness provides partial support for such speculation.

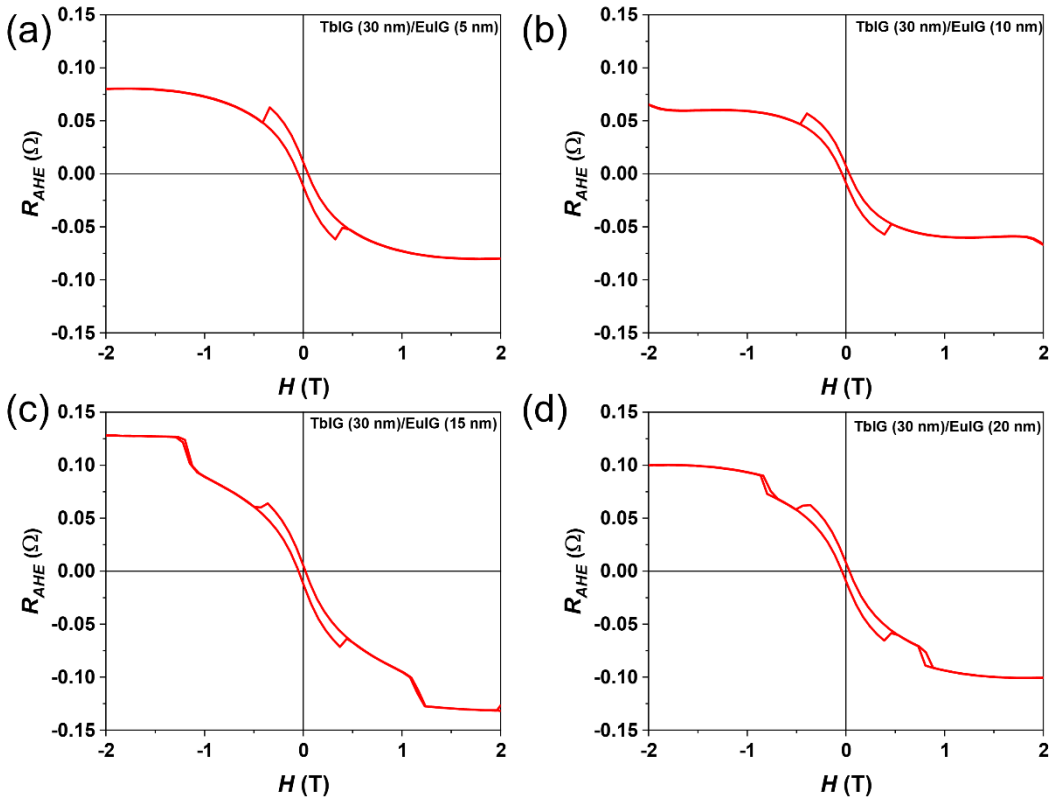

Fig. 5.18 The external field dependence of R_{AHE} at 10 K for TbIG/EuIG samples with different EuIG thicknesses (a) 5 nm, (b) 10 nm, (c) 15 nm, and (d) 20 nm.

The gradually disappearing offset loops may be explained by the interface exchange energy formula: $J_k = H_{ex} * M_s * t_{film}$ [48, 49], where H_{ex} represents the exchange coupling field, M_s and t_{film} are saturation magnetization and thickness of EuIG, respectively. Assuming the exchange coupling of TbIG/EuIG remains the same, increasing the EuIG thickness will lead to a reduced exchange bias field. Besides, as shown in Fig. 5.9(b), the sign of R_{AHE}^0 in the pure EuIG and TbIG layers are opposite at low temperatures. When the external field is large enough, the top EuIG layer begins to dominate and realize R_{AHE} sign switching.

The results of this work provide insights into the influence of interface coupling between different magnetic layers on spin transport, which helps design controllable spin transport in multilayer garnet heterostructures like magnon valves devices [50].

5.4 Conclusion

In summary, the modulation of T_{comp} in TbIG by constructing REIG bilayers composed of two different REIGs (EuIG and TbIG) was studied. The main results are highlighted below:

(1) Bilayer garnets (EuIG and TbIG) with similar structures can maintain the PMA when deposited on GGG (111) substrate, because there was no significant stress change compared with single-layer TbIG and EuIG.

(2) The R_{AHE}^0-T plots in all GGG/TbIG (30 nm)/EuIG (t nm)/Pt samples showed two R_{AHE}^0 sign flipping events [Fig. 13(b)]. The abrupt R_{AHE}^0 reversal was accompanied by a divergent H_c, which was related to T_{comp} and showed a strong EuIG thickness dependence. This indicates that the regulation of spin Hall magnetotransport in TbIG can be achieved through additional REIG layer.

(3) The tunable T_{comp} in GGG/TbIG (30 nm)/EuIG (t nm)/Pt bilayer system can be attributed to the ferromagnetic coupling of Fe sublattices in the two REIG layers. At low temperatures and sufficiently large external field, antiferromagnetic coupling behavior at the TbIG/EuIG interface was observed, as reflected by the multiple loops in R_{AHE}-H plots. When the external field was sufficiently large at low temperatures, the

top EuIG layer began to dominate and realize R_{AHE} sign switching, i.e., TbIG/EuIG exhibited antiferromagnetic coupling under sufficient external field.

References for Chapter 5

[1] C. Hahn, G. de Loubens, O. Klein, M. Viret, V.V. Naletov, J. Ben Youssef, Comparative measurements of inverse spin Hall effects and magnetoresistance in YIG/Pt and YIG/Ta, Phys. Rev. B 87 (2013) 174417.

[2] H. Nakayama, M. Althammer, Y.T. Chen, K. Uchida, Y. Kajiwara, D. Kikuchi, T. Ohtani, S. Geprags, M. Opel, S. Takahashi, R. Gross, G.E. Bauer, S.T. Goennenwein, E. Saitoh, Spin Hall magnetoresistance induced by a nonequilibrium proximity effect, Phys. Rev. Lett. 110 (2013) 206601.

[3] X. Liang, G. Shi, L. Deng, F. Huang, J. Qin, T. Tang, C. Wang, B. Peng, C. Song, L. Bi, Magnetic proximity effect and anomalous Hall effect in Pt/$Y_3Fe_{5-x}Al_xO_{12}$ heterostructures, Phys. Rev. Appl. 10 (2018) 024051.

[4] S. Meyer, M. Althammer, S. Geprägs, M. Opel, R. Gross, S.T.B. Goennenwein, Temperature dependent spin transport properties of platinum inferred from spin Hall magnetoresistance measurements, Appl. Phys. Lett. 104 (2014) 242411.

[5] A.Z. Arsad, A.W.M. Zuhdi, N.B.y. Ibrahim, M.A. Hannan, Recent advances in yttrium iron garnet films: Methodologies, characterization, properties, applications, and bibliometric analysis for future research directions, Appl. Sci. 13 (2023) 1218-1253.

[6] C.H. Du, H.L. Wang, Y. Pu, T.L. Meyer, P.M. Woodward, F.Y. Yang, P.C. Hammel, Probing the spin pumping mechanism: exchange coupling with exponential decay in $Y_3Fe_5O_{12}$/barrier/Pt heterostructures, Phys. Rev. Lett. 111 (2013) 247202.

[7] F. Yang, P. Chris Hammel, FMR-driven spin pumping in $Y_3Fe_5O_{12}$-based structures, J. Phys. D 51 (2018) 253001.

[8] W. Chen, M. Sigrist, D. Manske, Spin Hall effect induced spin transfer through an insulator, Phys. Rev. B 94 (2016) 104412.

[9] S. Vélez, A. Bedoya-Pinto, W. Yan, L.E. Hueso, F. Casanova, Competing effects at Pt/YIG interfaces: Spin Hall magnetoresistance, magnon excitations, and

magnetic frustration, Phys. Rev. B 94 (2016) 174405.

[10] X. Zhou, L. Ma, Z. Shi, W.J. Fan, J.-G. Zheng, R.F.L. Evans, S.M. Zhou, Magnetotransport in metal/insulating-ferromagnet heterostructures: Spin Hall magnetoresistance or magnetic proximity effect, Phys. Rev. B 92 (2015) 060402.

[11] M. Li, L. Jin, Z. Zhong, X. Tang, Q. Yang, L. Zhang, H. Zhang, Impact of interfacial chemical state on spin pumping and inverse spin Hall effect in YIG/Pt hybrids, Phys. Rev. B 102 (2020) 174435.

[12] R. Das, V. Kalappattil, R. Geng, H. Luong, M. Pham, T. Nguyen, T. Liu, M. Wu, M.H. Phan, H. Srikanth, Enhanced room-temperature spin Seebeck effect in a YIG/C_{60}/Pt layered heterostructure, AIP Adv. 8 (2018) 055906.

[13] N. Okuma, M.R. Masir, A.H. MacDonald, Theory of the spin-Seebeck effect at a topological-insulator/ferromagnetic-insulator interface, Phys. Rev. B 95 (2017) 165418.

[14] Y.K. Liu, H.F. Wong, K.K. Lam, K.H. Chan, C.L. Mak, C.W. Leung, Anomalous Hall effect in Pt/$Tb_3Fe_5O_{12}$ heterostructure: Effect of compensation point, J. Magn. Magn. Mater. 468 (2018) 235-240.

[15] Y.J. Hong, J.S. Kum, I.B. Shim, C.S. Kim, Spin rotation at compensation point studies of $Tb_3Fe_5O_{12}$ by Mössbauer spectroscopy, IEEE Trans. Magn. 40 (2004) 2808-2810.

[16] L. Liu, Z. Fan, Z. Chen, Z. Chen, Z. Ye, H. Zheng, Q. Zeng, W. Jia, S. Li, N. Wang, J. Liu, L. Ma, T. Lin, M. Qiu, S. Li, P. Han, J. Shi, H. An, Spin–orbit torques in heavy metal/ferrimagnetic insulator bilayers near compensation, Appl. Phys. Lett. 119 (2021) 052401.

[17] Y. Li, D. Zheng, C. Liu, C. Zhang, B. Fang, A. Chen, Y. Ma, A. Manchon, X. Zhang, Current-induced magnetization switching across a nearly room-temperature compensation point in an insulating compensated ferrimagnet, ACS Nano 16 (2022) 8181-8189.

[18] J.J. Bauer, P. Quarterman, A.J. Grutter, B. Khurana, S. Kundu, K.A. Mkhoyan, J.A. Borchers, C.A. Ross, Magnetic proximity effect in magnetic-insulator/heavy-

metal heterostructures across the compensation temperature, Phys. Rev. B 104 (2021) 094403.

[19] M. Kuila, Z. Hussain, V.R. Reddy, MOKE study of magnetic compensation in polycrystalline gadolinium iron garnet thin film, J. Magn. Magn. Mater. 473 (2019) 458-463.

[20] Q. Shao, A. Grutter, Y. Liu, G. Yu, C.-Y. Yang, D.A. Gilbert, E. Arenholz, P. Shafer, X. Che, C. Tang, M. Aldosary, A. Navabi, Q.L. He, B.J. Kirby, J. Shi, K.L. Wang, Exploring interfacial exchange coupling and sublattice effect in heavy metal/ferrimagnetic insulator heterostructures using Hall measurements, x-ray magnetic circular dichroism, and neutron reflectometry, Phys. Rev. B 99 (2019) 104401.

[21] S. Geprags, A. Kehlberger, F.D. Coletta, Z. Qiu, E.J. Guo, T. Schulz, C. Mix, S. Meyer, A. Kamra, M. Althammer, H. Huebl, G. Jakob, Y. Ohnuma, H. Adachi, J. Barker, S. Maekawa, G.E.W. Bauer, E. Saitoh, R. Gross, S.T.B. Goennenwein, M. Klaui, Origin of the spin Seebeck effect in compensated ferrimagnets, Nat. Commun. 7 (2016) 10452-10457.

[22] A. Chanda, N. Schulz, C. Holzmann, J. Seyd, M. Albrecht, M.-H. Phan, H. Srikanth, Thermal generation of spin current and magnon propagation length in compensated ferrimagnetic $Gd_3Fe_5O_{12}$ Thin Films, IEEE Trans. Magn. 58 (2022) 1-5.

[23] J.M. Liang, X.W. Zhao, Y.K. Liu, P.G. Li, S.M. Ng, H.F. Wong, W.F. Cheng, Y. Zhou, J.Y. Dai, C.L. Mak, C.W. Leung, The thickness effect on the compensation temperature of rare-earth garnet thin films, Appl. Phys. Lett. 122 (2023) 242401.

[24] H. Chen, D. Cheng, H. Yang, D. Wang, S. Zhou, Z. Shi, X. Qiu, Magnetization switching induced by magnetic field and electric current in perpendicular TbIG/Pt bilayers, Appl. Phys. Lett. 116 (2020) 112401.

[25] J.M. Liang, X.W. Zhao, S.M. Ng, H.F. Wong, Y.K. Liu, C.L. Mak, C.W. Leung, Observation of interfacial antiferromagnetic coupling between ferrimagnetic garnet thin films, IEEE Trans. Magn. 58 (2022) 1-5.

[26] B.W. Dong, J. Cramer, K. Ganzhorn, H.Y. Yuan, E.J. Guo, S.T.B. Goennenwein, M. Klaui, Spin Hall magnetoresistance in the non-collinear ferrimagnet GdIG close to the compensation temperature, J. Phys. Condens. Matter. 30 (2018) 035802.

[27] W. Zhang, M.B. Jungfleisch, W. Jiang, Y. Liu, J.E. Pearson, S.G.E.t. Velthuis, A. Hoffmann, F. Freimuth, Y. Mokrousov, Reduced spin-Hall effects from magnetic proximity, Phys. Rev. B 91 (2015) 115316.

[28] S. Ding, Z. Liang, C. Yun, R. Wu, M. Xue, Z. Lin, A. Ross, S. Becker, W. Yang, X. Ma, D. Chen, K. Sun, G. Jakob, M. Kläui, J. Yang, Anomalous Hall effect in magnetic insulator heterostructures: Contributions from spin-Hall and magnetic-proximity effects, Phys. Rev. B 104 (2021) 224410.

[29] C.Y. Guo, C.H. Wan, X. Wang, C. Fang, P. Tang, W.J. Kong, M.K. Zhao, L.N. Jiang, B.S. Tao, G.Q. Yu, X.F. Han, Magnon valves based on YIG/NiO/YIG all-insulating magnon junctions, Phys. Rev. B 98 (2018) 134426.

[30] Y. Chen, E. Cogulu, D. Roy, J. Ding, J.B. Mohammadi, P.G. Kotula, N.A. Missert, M. Wu, A.D. Kent, Spin transport in an insulating ferrimagnetic-antiferromagnetic-ferrimagnetic trilayer as a function of temperature, AIP Adv. 9 (2019) 105319.

[31] S. Mokarian Zanjani, M.C. Onbaşlı, Predicting new iron garnet thin films with perpendicular magnetic anisotropy, J. Magn. Magn. Mater. 499 (2020) 166108.

[32] H. Fuess, G. Bassi, M. Bonnet, A. Delapalme, Neutron scattering length of terbium structure refinement and magnetic moments of terbium iron garnet, Solid State Commun. 18 (1976) 557-562.

[33] T. Fakhrul, B. Khurana, B.H. Lee, S. Huang, H.T. Nembach, G.S.D. Beach, C.A. Ross, Damping and interfacial dzyaloshinskii-moriya interaction in thulium iron garnet/bismuth-substituted yttrium iron garnet bilayers, ACS Appl. Mater. Interfaces 16 (2024) 2489-2496.

[34] V.H. Ortiz, M. Aldosary, J. Li, Y. Xu, M.I. Lohmann, P. Sellappan, Y. Kodera, J.E. Garay, J. Shi, Systematic control of strain-induced perpendicular magnetic

anisotropy in epitaxial europium and terbium iron garnet thin films, APL Mater. 6 (2018) 121113.

[35] V.H. Ortiz, B. Arkook, J. Li, M. Aldosary, M. Biggerstaff, W. Yuan, C. Warren, Y. Kodera, J.E. Garay, I. Barsukov, J. Shi, First- and second-order magnetic anisotropy and damping of europium iron garnet under high strain, Phys. Rev. Mater. 5 (2021) 124414.

[36] S.M. Suturin, A.M. Korovin, V.E. Bursian, L.V. Lutsev, V. Bourobina, N.L. Yakovlev, M. Montecchi, L. Pasquali, V. Ukleev, A. Vorobiev, A. Devishvili, N.S. Sokolov, Role of gallium diffusion in the formation of a magnetically dead layer at the $Y_3Fe_5O_{12}/Gd_3Ga_5O_{12}$ epitaxial interface, Phys. Rev. Mater. 2 (2018) 104404.

[37] J.M. Gomez-Perez, S. Vélez, L. McKenzie-Sell, M. Amado, J. Herrero-Martín, J. López-López, S. Blanco-Canosa, L.E. Hueso, A. Chuvilin, J.W.A. Robinson, F. Casanova, Synthetic antiferromagnetic coupling between ultrathin insulating garnets, Phys. Rev. Appl. 10 (2018) 044046.

[38] R. Kumar, S.N. Sarangi, D. Samal, Z. Hossain, Positive exchange bias and inverted hysteresis loop in $Y_3Fe_5O_{12}/Gd_3Ga_5O_{12}$, Phys. Rev. B 103 (2021) 064421.

[39] A. Mitra, O. Cespedes, Q. Ramasse, M. Ali, S. Marmion, M. Ward, R.M.D. Brydson, C.J. Kinane, J.F.K. Cooper, S. Langridge, B.J. Hickey, Interfacial origin of the magnetisation suppression of thin film yttrium iron garnet, Sci. Rep. 7 (2017) 11774-11781.

[40] J.J. Bauer, E.R. Rosenberg, C.A. Ross, Perpendicular magnetic anisotropy and spin mixing conductance in polycrystalline europium iron garnet thin films, Appl. Phys. Lett. 114 (2019) 052403.

[41] E.R. Rosenberg, L. Beran, C.O. Avci, C. Zeledon, B. Song, C. Gonzalez-Fuentes, J. Mendil, P. Gambardella, M. Veis, C. Garcia, G.S.D. Beach, C.A. Ross, Magnetism and spin transport in rare-earth-rich epitaxial terbium and europium iron garnet films, Phys. Rev. Mater. 2 (2018) 094405.

[42] C. Tang, P. Sellappan, Y. Liu, Y. Xu, J.E. Garay, J. Shi, Anomalous Hall hysteresis

in $Tm_3Fe_5O_{12}$/Pt with strain-induced perpendicular magnetic anisotropy, Phys. Rev. B 94 (2016) 140403.

[43] M. Uemura, T. Yamagishi, S. Ebisu, S. Chikazawa, S. Nagata, A double peak of the coercive force near the compensation temperature in the rare earth iron garnets, Nat. Mater. 88 (2008) 209-228.

[44] K.J. Kim, S.K. Kim, Y. Hirata, S.H. Oh, T. Tono, D.H. Kim, T. Okuno, W.S. Ham, S. Kim, G. Go, Y. Tserkovnyak, A. Tsukamoto, T. Moriyama, K.J. Lee, T. Ono, Fast domain wall motion in the vicinity of the angular momentum compensation temperature of ferrimagnets, Nat. Mater. 16 (2017) 1187-1192.

[45] W.P. Wolf, J.H. Van Vleck, Magnetism of Europium Garnet, Phys. Rev. 118 (1960) 1490-1492.

[46] M. Isasa, E. Villamor, L.E. Hueso, M. Gradhand, F. Casanova, Temperature dependence of spin diffusion length and spin Hall angle in Au and Pt, Phys. Rev. B 91 (2015) 024402.

[47] S. Becker, Z. Ren, F. Fuhrmann, A. Ross, S. Lord, S. Ding, R. Wu, J. Yang, J. Miao, M. Kläui, G. Jakob, Magnetic coupling in $Y_3Fe_5O_{12}/Gd_3Fe_5O_{12}$ heterostructures, Phys. Rev. Appl. 16 (2021) 014047.

[48] D. Spenato, J.B. Youssef, H. Le Gall, J. Ostoró, From ferromagnetic – ferromagnetic to ferromagnetic – antiferromagnetic exchange coupling in NiFe/MnNi bilayers, J. Appl. Phys. 89 (2001) 6898-6900.

[49] C.-C. Lin, C.-H. Lai, R.-F. Jiang, H.-P.D. Shieh, High interfacial exchange energy in TbFeCo exchange-bias films, J. Appl. Phys. 93 (2003) 6832-6834.

[50] Z. Li, X. Zhang, D. Zhang, B. Liu, H. Meng, J. Xu, Z. Zhong, X. Tang, H. Zhang, L. Jin, Magnetization dynamics in the YIG/Au/YIG magnon valve, APL Mater. 10 (2022) 021101.

Chapter 6 Spin magnetotransport in REIG/Pt: effects of modulated bulk and REIG/Pt interfaces

In Chapter 5, I demonstrated controllable T_{comp} by changing the EuIG layer thickness in TbIG/EuIG bilayer systems, through the use of the coupling relationship between EuIG and TbIG. The results indicated the influence of REIG thickness on spin transport. In this Chapter, a REIG sandwich structure was constructed based on the study of TbIG/EuIG bilayer system. By keeping the total thickness of the REIG layers in the stack fixed, the effects of layer stacking order on spin Hall transport are explored.

6.1 Introduction

Previous studies on REIGs with T_{comp} mainly focused on single-layer structures, in which the magnetic moments of different sublattices follow the same competitive mechanism (i.e., the direction of RE and Fe moments are in antiparallel alignment) [1-5]. Iron garnets that have been widely studied include TbIG [6], DyIG [7, 8], and GdIG [9, 10]. The temperature-dependent magnetism of single-layer REIG, and the impact of magnetization compensation phenomena on interface effects such as SSE [11, 12], AHE [13, 14], and SHE [15, 16], were analyzed.

It was found that T_{comp} can be tuned by regulating the film stress, which can be achieved in various ways. For example, Li *et al.* successfully altered the stress of single-layer TbIG films using different substrates, thereby achieving T_{comp} regulation from 196 K to 160 K [17]. Besides, varying the thickness of the films can also lead to stress changes and consequently affects T_{comp} [6]. These studies have shown enormous potential for wide temperature range applications of REIGs in fast information storage, and have provided experimental ideas for designing complex garnet systems.

As is well known, the RE:Fe ratio within the REIG bulk has a significant impact on T_{comp} [18, 19]. With the continuous exploration of REIG, research interest has shifted from single layers to multilayered structures. For bilayer REIG films, additional

consideration is needed for the coupling between different REIG layers [20]. In Chapter 5, I utilized the coupling effect in REIG bilayers to successfully achieve variable T_{comp} in TbIG.

However, it is worth noting that previous studies on the regulation of REIG bulk were mainly focused on thickness dependence, including bilayer systems like YIG/GdIG films with in-plane anisotropy [20]. Little attention has been paid to the impact of stacking order on spin Hall transport of multi-layered systems. Especially for the TbIG/Pt system, its R_{AHE}-H signal shows the phenomenon of R_{AHE}^{0} double sign-flipping, making it attractive to construct REIG multilayers based on TbIG.

T_1 and T_{comp} are the main features of the TbIG/Pt structure. As mentioned earlier, T_1 is related to the competition between SHE and MPE [13, 21, 22], while T_{comp} is attributed to the antiparallel alignment of RE and Fe sublattices; these have been discussed in similar studies [3, 23, 24]. The thickness dependence of T_{comp} in TbIG/EuIG bilayer system has been analyzed. However, the impact on T_{comp} in a multilayer REIG stack with fixed total thickness but modulated composition along the thickness direction is seldom reported. Two critical issues could be explored: one is the contribution of the REIG bulk on sign reversal due to additional interfaces generated by multiple REIG layer stacking, and another is the impact of different REIG/Pt interfaces caused by varying topmost REIG layer. The relative contribution of modulated REIG bulk and REIG/Pt interface on the spin magnetotransport is worth exploring.

In this Chapter, while the research is still based on TbIG/Pt, I modulate the TbIG bulk by inserting a different REIG with fixed thickness at different positions along the film growth direction. To minimize the impact of mismatch on this study and not interfere with the observation of intrinsic T_{comp} of TbIG, EuIG was chosen as the intercalation layer. The similar lattice constants of TbIG (12.436 Å) [25] and EuIG (12.5 Å) [26] permits their epitaxial growth on GGG (12.376 Å) substrates [26]. Besides, EuIG does not exhibit magnetization compensation [27], avoiding the possibility of multiple compensation points in the systems. Moreover, the epitaxial

growth of EuIG and TbIG on GGG (111) exhibits PMA [28], which is beneficial for R_{AHE} measurements.

When modulating the multi-layer REIG bulk, EuIG with fixed thickness is moved from the bottom to the top of the layer, i.e., the REIG/Pt interface will eventually change from TbIG/Pt to EuIG/Pt. The REIG bulk will undergo variations from a bilayer to a sandwich structure, and finally back to the bilayer structure. The overall thickness of the REIG stack remains constant throughout the entire process. The fixed TbIG and EuIG thicknesses ensure a constant total magnetization, which helps to eliminate the impact caused by thickness variations.

T_{comp} of the stacked REIG is observed through R_{AHE}-H loop measurements. Temperature dependent R_{AHE} loops would show the impact of stacking sequence, as well as the presence of additional TbIG/EuIG interfaces.

6.2 Experimental Details

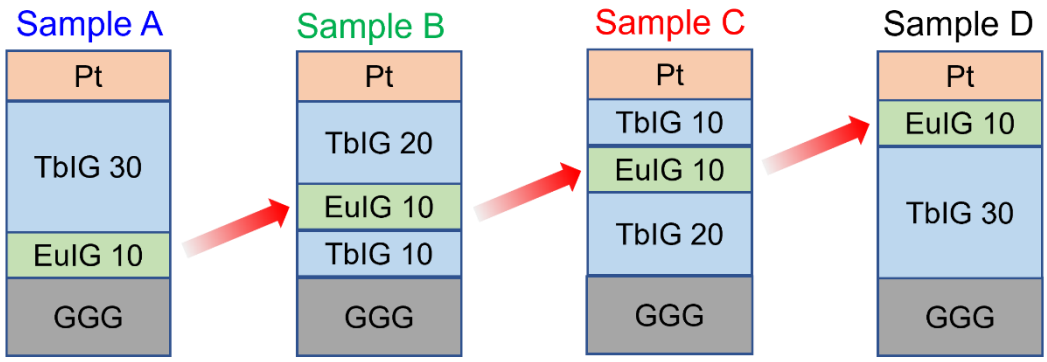

Fig. 6.1 Schematic diagram of deposition sequence for multilayer samples.

As shown in Fig. 6.1, four different stacks of TbIG (t nm)/EuIG (10 nm)/TbIG (30-t nm)/Pt films (namely Samples A, B, C, and D) are deposited on GGG (111) using PLD. From Sample A to Sample D, the EuIG (10 nm) gradually approaches Pt from the bottom and eventually becomes the top layer in contact with Pt. During the process of changing the deposition position of EuIG, a sandwich structure is formed (Samples B and C). Additionally, one should notice that the four samples maintain the same total thickness of 40 nm, with a fixed EuIG of 10 nm. The relative thickness of the two TbIG

layers is modulated, but the total TbIG thickness remains at 30 nm. Moreover, Samples A, B, and C maintain the TbIG/Pt interface, which contrasts with the EuIG/Pt interface of Sample D; this is beneficial for studying the influence of different interfaces on spin transport. The specific deposition parameters and Hall device fabrication process are the same as those described in Chapter 4.

6.3 Results and Discussions

6.3.1 Structural characterization

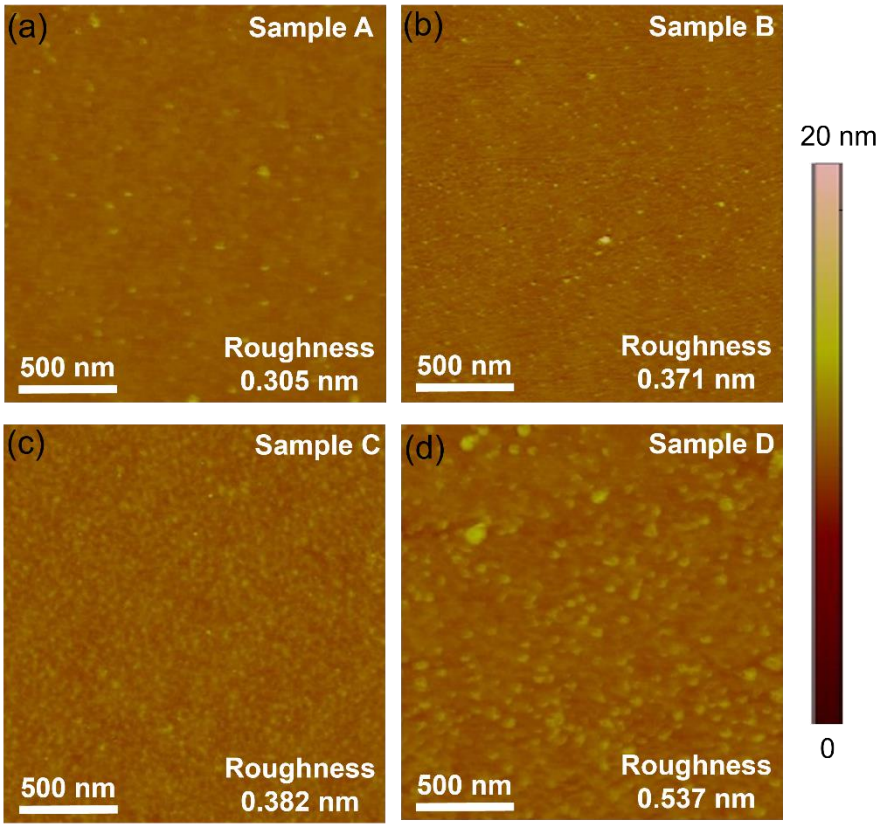

Fig. 6.2 AFM images of all samples. The roughness was obtained from the top REIG surface.

Fig. 6.2 compares the interface morphology of all Samples. In Sample A with a bilayer structure, the surface roughness is the smallest (root-mean-squared value of 0.305 nm). Samples B and C with a sandwich structure have slightly increased

roughness (0.371 nm and 0.382 nm, respectively). When EuIG moves to the topmost layer, the roughness reaches its maximum (0.537 nm). The difference in roughness would lead to inconsistent interface quality in REIG/Pt contact. Nevertheless, the roughness of all samples is within a reasonable range, indicating good epitaxial quality of the multilayer samples.

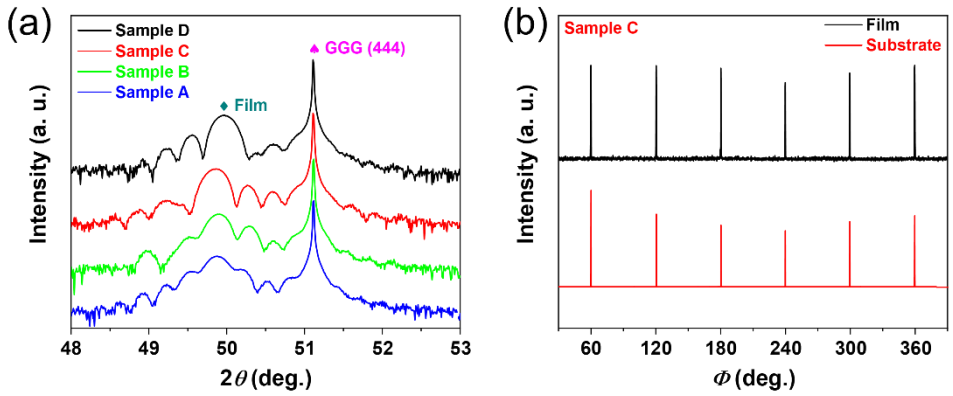

Fig. 6.3 (a) XRD profile of the sample series. (b) φ scan of Sample C recorded at (642) reflection, indicating six-fold symmetry and epitaxial relation between TbIG/EuIG/TbIG film and GGG substrate.

Fig. 6.3(a) shows the XRD profiles of the samples. Due to the minute difference in lattice constants among GGG, EuIG, and TbIG [25, 26], it is obvious that the mixed film peaks of Samples A, B, and C are relatively close. Still, there is a sizable shift in the peak position of Sample D. The 2θ value of film peaks shift from 48.86° (Sample A) to 49.96° (Sample D).

The difference in mixed film peak positions can be attributed to a change in the stress state after the complete exchange of positions between EuIG and TbIG. The lattice mismatch η follows the formula $\eta = |\frac{A_{sub}-B_{REIG}}{B_{REIG}}|$ [29], where A_{sub} and B_{REIG} are the lattice constants of the substrate and REIG bulk, respectively. The calculated $\eta_{GGG/TbIG} = 0.48\%$ and $\eta_{GGG/EuIG} = 0.99\%$ indicate the variations in stress and both of single-layer REIG films show in-plane compressive strain. Therefore, PMA is expected in a multilayered system. Laue oscillation can be observed around

film peaks, indicating the high crystallinity of the samples.

To confirm the epitaxial relation between the film and the substrate, φ scan was measured for Sample C and is presented in Fig. 6.3(b). The six-fold symmetry between trilayer TbIG/EuIG/TbIG film and GGG (642) substrate peaks, and the matching positions between the film and substrate peaks in the φ scan, implies good epitaxial relationship between the film and the GGG substrate.

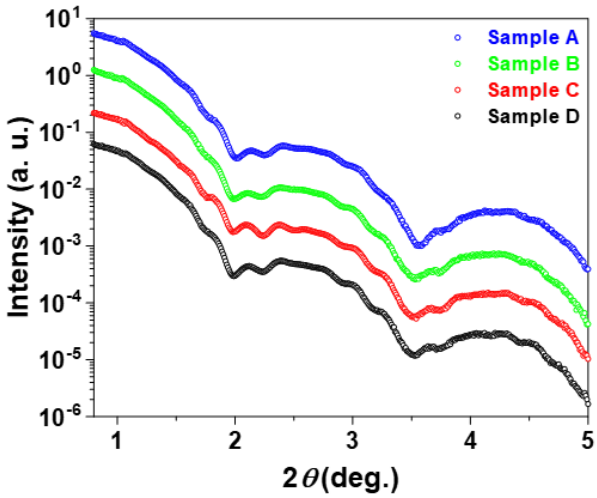

Fig. 6.4 XRR plots for all samples, with the plots being offset for clarity.

Table 6-1 The layer thickness for all samples estimated through XRR fitting, with error margins indicated in brackets.

	Sample A	Sample B	Sample C	Sample D
Pt (nm)	5.25 (5)	5.25 (7)	5.30 (8)	5.27 (2)
TbIG (nm)	29.78 (10)	20.13 (12)	10.73 (3)	/
EuIG (nm)	9.55 (14)	10.88 (17)	10.16 (4)	10.60 (11)
TbIG (nm)	/	11.0 (4)	19.87 (15)	30.50 (8)
Total thickness (nm)	39.33	42.01	40.76	41.10

The thicknesses of the four samples were measured using XRR, and the results are shown in Fig. 6.4. The total thickness of each sample, and the corresponding constituent layers, were obtained through fitting and are shown in Table 6-1. The results show that

the calculated thickness of the four samples agree well with the deposition rates estimated through the calibration samples.

To further confirm the thickness, Sample C was observed through the cross-sectional TEM. As shown in Fig. 6.5(a), the red dashed lines indicate the boundaries of each layer. The actual thickness obtained from measurement is close to the expected thickness of GGG/TbIG (20 nm)/EuIG (10 nm)/TbIG (10 nm).

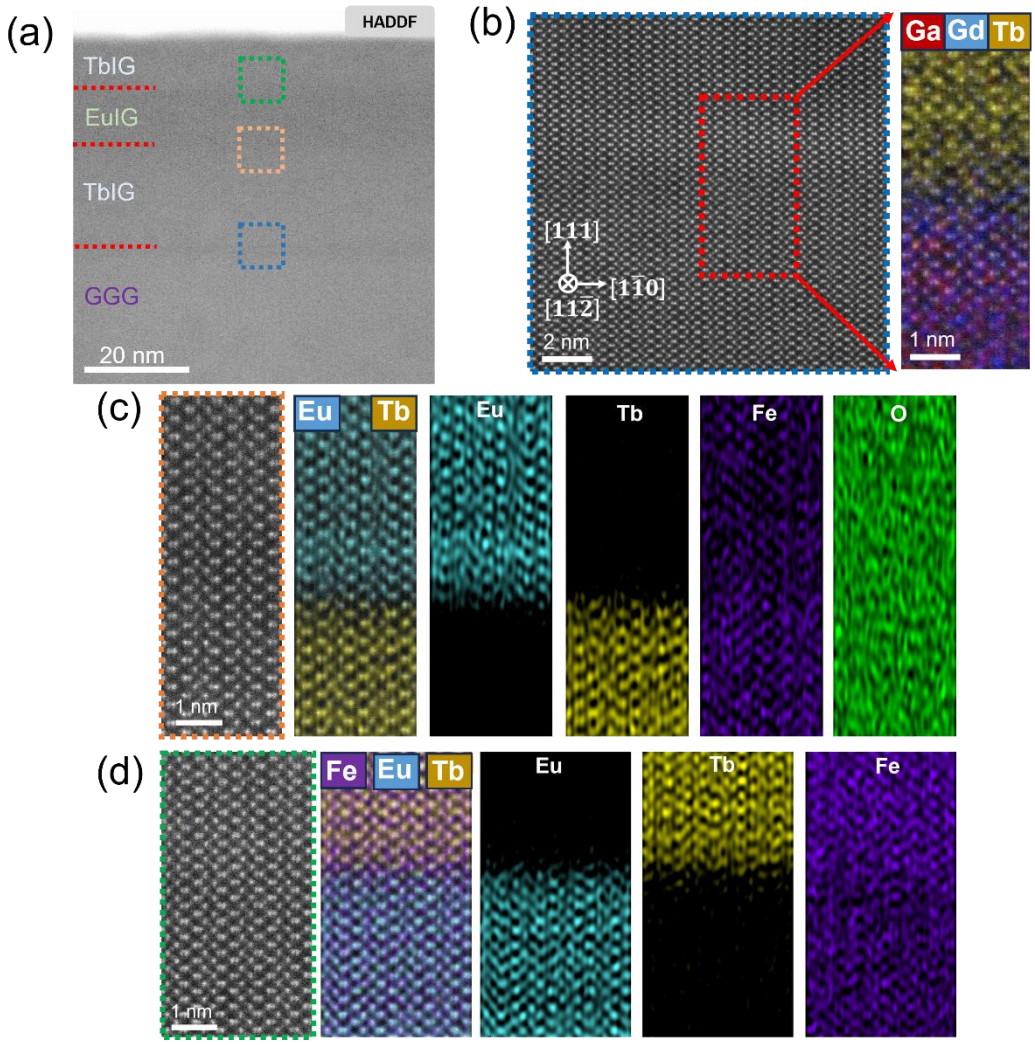

Fig. 6.5 (a) STEM image of Sample C, with the red dashed lines showing various interfaces. (b) Left panel: Magnified GGG/TbIG interface extracted from (a) (blue box). Right panel: A mixed EDX mapping shows element distribution, extracted from the enclosed region on the left panel. (c) EDX analysis at the TbIG/EuIG interface [yellow box in (a)]. (d) EDX analysis at the EuIG/TbIG interface [green box in (a)].

Element distribution analysis was also performed through EDX mapping. Due to multiple interfaces generated in the sandwich structure, the EDX images of three different interfaces in Sample C were analyzed. The blue, yellow, and green boxes in Fig. 6.5(a) are magnified and presented in Fig. 6.5(b) - (d). The GGG/TbIG interface in Fig. 6.5(b) shows a uniform atomic arrangement with no prominent vacancies or dislocations, as well as a high degree of epitaxy in TbIG because of the minute lattice mismatch with the substrate. The results are consistent with the XRD and φ scan analyses in Fig. 6.3(a). Additionally, it is evident that Gd and Tb have a trend of interdiffusion across the boundary, manifested as a mixed layer of Tb (yellow pixels) and Gd (blue pixels) in a thickness range of ~ 1-2 nm, which is generally called the transient layer and is common PLD film growth [10, 30-33]. Considering that EuIG and TbIG have the same growth conditions and fixed total thickness in this sample series, the properties and thickness of the transient layer between the substrate and film should be similar. In other words, the effect of the transient layer on all samples can be considered as constant. In this work, it is believed that the influence of the transient layer on T_1 and T_{comp} should be consistent, and it will not be discussed in the subsequent analysis as a variable factor.

Similarly, the yellow boxed region (internal TbIG/EuIG interface) and the green boxed region (internal EuIG/TbIG interfaces) in Fig. 6.5 (a) are examined, and the results are shown as Figs. 6.5(c) and (d). Both cases exhibit inevitable elements interdiffusion and the same atomic structure with the GGG substrate, indicating good crystallinity throughout the whole sandwich structure.

6.3.2 Magnetic transport characterization

As mentioned earlier, PMA would be maintained in GGG (111)/TbIG or GGG (111)/EuIG structures due to the positive magnetostriction coefficient and in-plane compressive strain [28, 34]. Fig 6.6 shows that the M_s are similar for all samples at room temperature. Considering there is ferromagnetic coupling between Fe in TbIG and EuIG, under the same sufficiently large extra field, only the antiparallel competition

of RE and Fe needs to be considered. If the thicknesses of these four samples are identical, theoretically, their M_S should be the same. The reason for the shift in M_S can be attributed to the difficulty in precise control of the thickness in all samples during the deposition process. The thickness error leads to the fluctuation of M_S. Within a modest range of thickness error (± 5%), the fluctuation is considered acceptable.

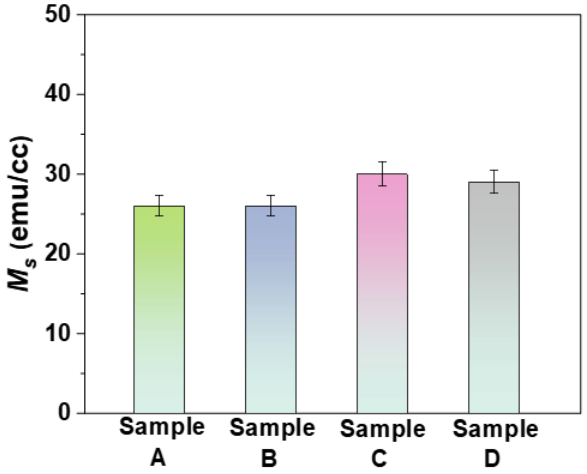

Fig. 6.6 Comparison of M_S for all samples. The error bar is about ± 5%.

6.3.3 Electrical transport characterization

Temperature-dependent R_{AHE}-H of all samples were measured at 50-300 K. As shown in Fig. 6.7, all samples display square loops, suggesting PMA behavior in both bilayer and trilayer samples, and all of them have undergone two R_{AHE}^0 sign flips.

To provide a more intuitive comparison of the temperature dependence of sample properties when EuIG gradually moves from the bottom layer to direct contact with Pt, H_c and R_{AHE}^0 are extracted from R_{AHE}-H loops in Fig. 6.7 and the results are shown in Fig. 6.8. A divergent H_c can be found in Fig. 6.8(a) for all samples. As mentioned earlier, the antiparallel moments of RE and Fe ions compete and completely cancel out at T_{comp}, as reflected in the H_c divergence due to near-zero net moments [2, 35, 36]. It is worth noting that the divergent H_c of all samples are concentrated at around 170 K.

In terms of R_{AHE}^0, Fig. 6.8(b) shows that first R_{AHE}^0 sign cross-over, accompanied by a sharp R_{AHE}^0 sign reversal, occurs at around 170 K, which can be attributed to the

reorientation of the magnetic moment direction of internal sublattices across T_{comp}. In short, the appearance of T_{comp} is accompanied by two features in AHE measurements, namely divergent H_c and an abrupt R_{AHE}^0 sign flip.

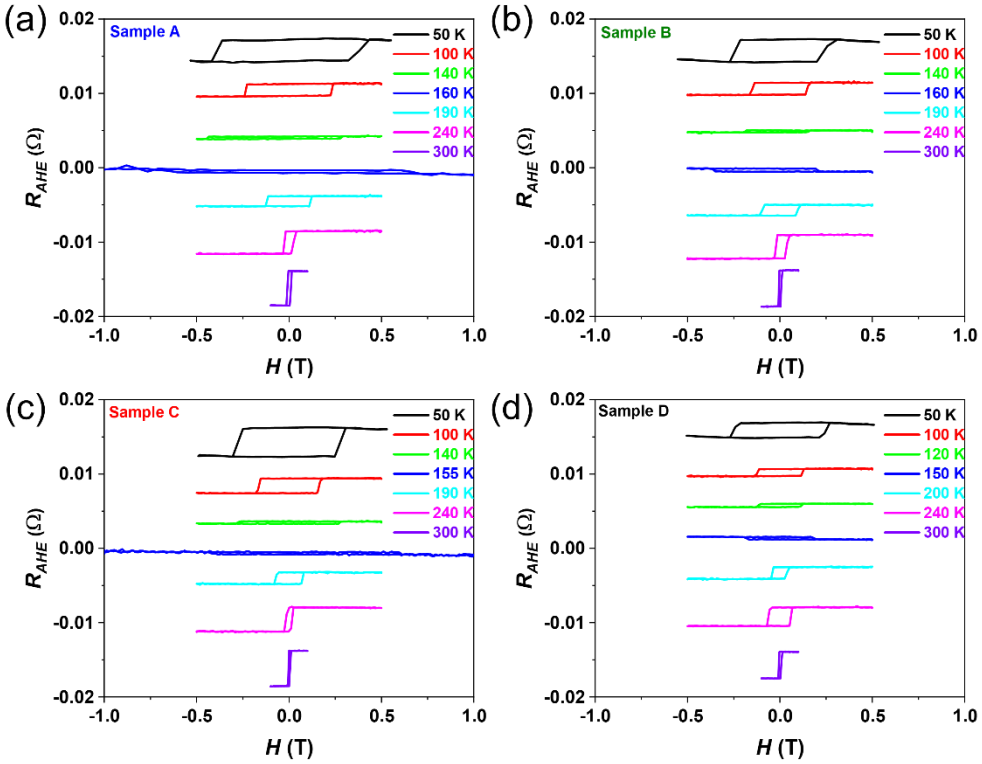

Fig. 6.7 Temperature dependent R_{AHE}-H loops of all samples.

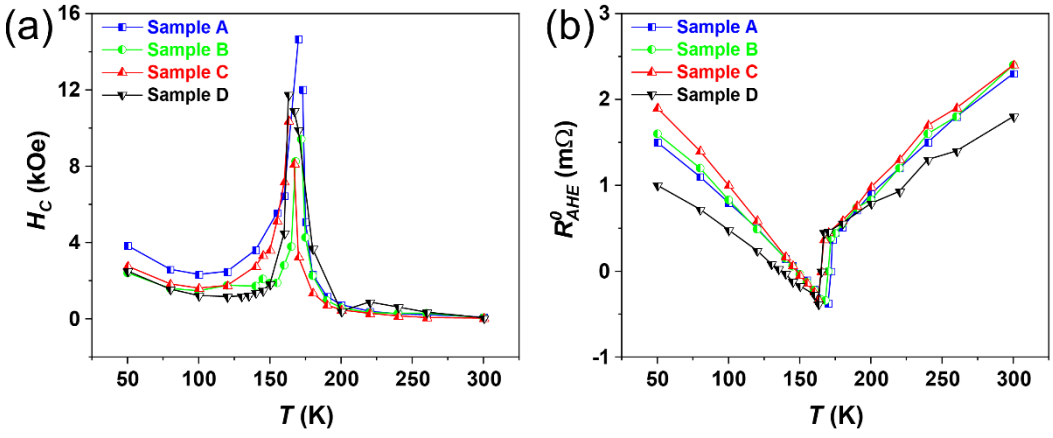

Fig. 6.8 Comparison of temperature-dependent H_c (a) and R_{AHE}^0 (b) for the sample series.

In addition to the R_{AHE}^{0} sign reversal around 170 K, Fig. 6.8(b) shows another sign flip T_1 as the temperature goes down. The T_1 significantly differs from the T_{comp} (~170 K) in two aspects. Firstly, compared to the abrupt sign flip near 170 K, T_1 is much more gradual. Secondly, the T_1 has an explicit interface dependency. When the interface is TbIG/Pt, the T_1 is 149 K; while when the interface is changed to EuIG/Pt, the flipping temperature decreases to 137 K.

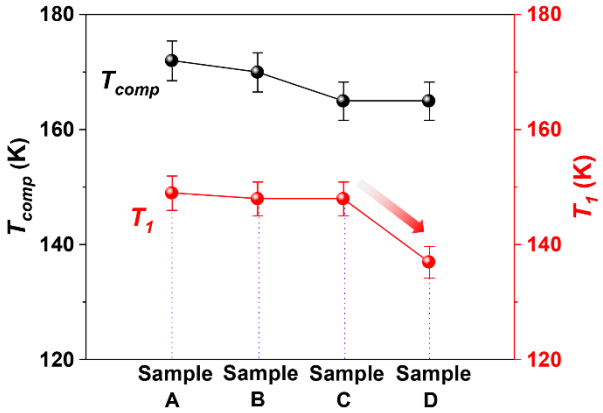

Fig. 6.9 Comparisons of T_{comp} and T_1 for all samples. The black plot represents T_{comp}, and the red plot represents T_1. The error bar is $\pm$ 2%.

To observe their variations more clearly, the two cross-over points in Fig. 6.8 are extracted and displayed in Fig. 6.9. Notice that as EuIG gradually moves close to the Pt, T_{comp} shows fluctuation between 165 K and 172 K. This could be related to the RE:Fe ratio, as variations in RE:Fe ratio can also lead to changes in T_{comp}. Previous reports have shown an enhancement of T_{comp} with either an excess in Tb or a deficit in Fe [35, 37].

However, these T_{comp} values in modulated REIG films are far lower than the bulk value (248 K) of TbIG [35]. There are some possibilities. Firstly, the stress state of epitaxial films is different from that of bulk samples. Previous work reported that T_{comp} exhibits significant stress dependence in the thin film form. T_{comp} decreases (from 196 K to 160 K) as the lattice constant of the substrates increases [from GGG (1.238 nm) to GSGG (1.257 nm)] [17]. The growth of thin films is influenced by the stress constraint of the substrate, while bulk samples are in a stress-free state. In this thesis, the multi-

layer films are under in-plane compressive strain of GGG substrates. Therefore, in addition to the competition of sublattice ions inside the REIG, the effect of stress should be considered.

Besides, the coupling among REIG materials in the multilayer is another key factor. The stacked TbIG and EuIG films have strong interface coupling through different sublattices. It is known that EuIG has no magnetization compensation behavior, as the ground state of Eu^{3+} is $J = 0$ [27, 38]. The moment contribution of Eu^{3+} can be ignored and the overall moment in EuIG is completely dominated by Fe^{3+}. The T_{comp} appearing in the sandwich sample should include the contribution of additional Fe moments from EuIG layer. Considering that the total thickness of TbIG is fixed at 30 nm for this sample series, the T_{comp} of single-layer TbIG (30 nm) was selected for comparison to distinguish the contribution of EuIG.

Previous work reported that T_{comp} of TbIG (30 nm) is ~220 K [24], which is much higher than that of the sandwich TbIG/EuIG/TbIG films. As mentioned above, the coupling between stacked layers is an essential factor to consider. Notice that the magnetizations of EuIG and TbIG are dominated by Fe^{3+} at above T_{comp}. Under sufficiently large external field, the magnetic moments of Fe^{3+} in each REIG layer are in the same direction, i.e., the EuIG and TbIG layers are ferromagnetically coupled. Meanwhile, the magnetic moment of Tb^{3+} has a different temperature dependence than Fe^{3+}. If Tb^{3+} is to completely dominate the net magnetic moment of the entire sandwich film, Tb^{3+} needs to compete with Fe^{3+} in both TbIG and EuIG layers. However, as TbIG is fixed at 30 nm, complete cancellation of antiparallel moments can only be achieved at lower temperatures when Tb^{3+} moment eventually balances that of Fe^{3+}, which is reflected in a decrease in T_{comp}.

Based on the above analysis, the strong interface coupling among each stacked layer is a vital factor for the sharp decrease in T_{comp} compared with single-layer TbIG (30 nm). This coupling phenomenon should to be expected, as previous study also reported the presence of ferromagnetic coupling in bilayer YIG/GdIG samples with in-plane easy axis, leading to a decrease in T_{comp} [20].

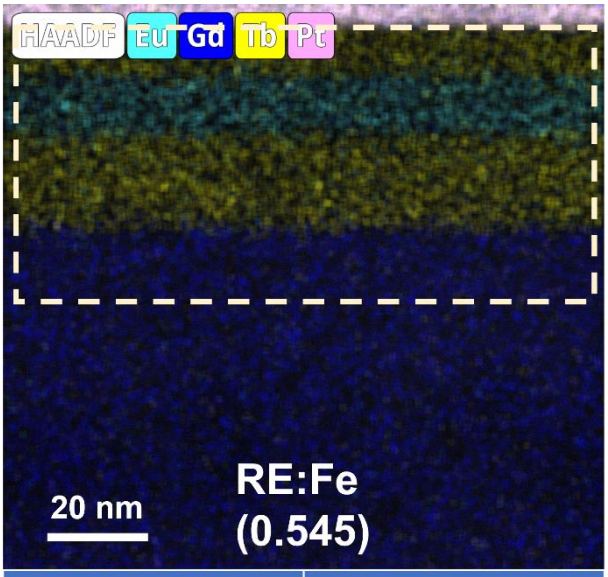

Element	Atomic Fraction (%)
Tb	6.75
Eu	3.54
Fe	18.94

Fig. 6.10 Mixed elements distribution across layers in Sample C through EDX mapping. Atomic fractions are extracted from the dashed rectangle. The ratio of the sample C is 0.545.

Theoretically, in a fixed-thickness REIG sample, the net magnetic moment of the REIG bulk should be constant, meaning that T_{comp} should be the same. The reason for this fluctuation of T_{comp} among the samples in the sandwich series could lie in the difficulty of precisely controlling the layer thickness among different runs. Besides, multi-layer stackings are prone to generate defects such as vacancies, and the RE:Fe ratio in REIGs may deviate from the expected value of 0.6.

To verify whether the RE:Fe ratio is normal, EDX of Sample C was analyzed. As shown in Fig. 6.10, the RE:Fe ratio of the whole structure is 0.545, which is lower than the stoichiometric RE:Fe value. The lower RE:Fe ratio means that Fe is excessive in Sample C. A stronger moment of Tb is required to completely cancel out the moment of Fe, which will be achieved at lower temperatures. Fig. 6.9 shows T_{comp} of Samples

C and D are the same, but Samples B and C with sandwich structures have different T_{comp}. No evident trend was observed in the T_{comp} changes, indicating stacking sequence may not be the determining factor causing T_{comp} fluctuations.

Furthermore, it is noted that both M_S and T_{comp} exhibit inevitable fluctuations. In addition to the difference in RE: Fe ratio, there may also be slight variations in thickness. Even though the growth conditions of PLD are entirely consistent, precise control of thickness is still challenging. The results of XRR reflect this situation. Therefore, the possibility that T_{comp} fluctuations is due to inconsistent thickness of sandwich structures cannot be excluded.

Based on the above analysis, I suggest that the fluctuations in M_S and T_{comp} of sandwich films can be attributed to stoichiometric imbalances caused by transient layers or slight fluctuations in thickness. However, within the allowable range of errors and with uniform growth conditions, the impact of stacking order on T_{comp} can be ignored.

Meanwhile, as shown in Fig. 6.9, the second cross-over point T_1 is accompanied by a gradual variation of R_{AHE}^0 from negative to positive value with decreasing temperatures, which differs from the abrupt change at T_{comp}. Previous work attributed the occurrence of T_1 to the competition between MPE and SHE [39]. The Pt at the REIG/Pt interface possesses a certain magnetic moment due to the adjacent magnetic layer through MPE, which means that part of the AHE contribution comes from MPE. At the same time, the charge current in the Pt layer would activate a spin current, and the transport of spin current at the REIG/Pt interface would generate SHE. The MPE and SHE-induced AHE compete with each other, finally leading to the emergence of T_1.

Interestingly, T_1 seems to be sensitive towards the garnet species at the REIG/Pt interface. As mentioned earlier, T_1 maintains the same value when the topmost layer is TbIG (Samples A, B, and C), while shifting from 149 K to 137 K when the topmost layer is replaced by EuIG (Sample D). The shift in T_1 is different from the T_{comp} fluctuation discussed previously. The modulated T_{comp} is highly related to the REIG bulk, such as the internal net magnetic moment and stress state. On the other hand, the

variable T_1 is attributed to the ability of spin magnetotransport at the REIG/Pt interface, as both MPE and SHE are interfacial effects. The sensitivity of interfaces is mainly reflected in two aspects: REIG/Pt exchange coupling energy and interface quality.

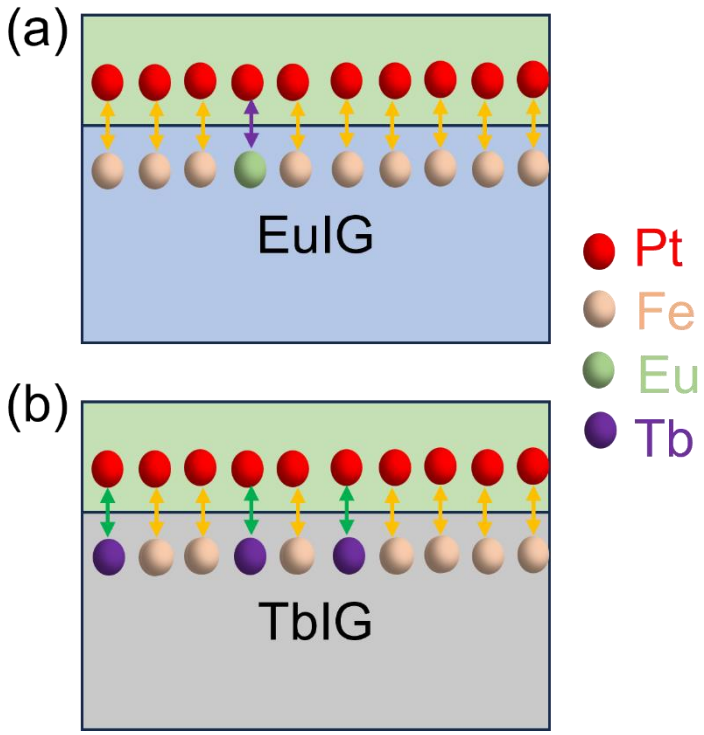

Fig. 6.11 Schematic model of exchange coupling for different REIG/Pt interfaces: (a) EuIG/Pt; (b) TbIG/Pt.

Previous work reported that the spin transport at REIG/Pt interface is dominated by Fe/Pt exchange coupling throughout the whole temperature range, as the *d*-orbit Fe^{3+} shows robust delocalization compared with the *f*-orbit RE^{3+} [39]. Interestingly, the ground state of Eu^{3+} seems unstable. If the second-order Zeeman effect is activated in EuIG, Eu^{3+} will exhibit limited paramagnetism, especially at higher temperatures [38]. Therefore, when studying the sensitivity of the REIG/Pt interface of T_1, the contribution of Eu^{3+} can be considered.

The simple interface exchange coupling model in Fig. 6.11 illustrates the interface sensitivity of T_1. As described above, the interface exchange coupling energy of Fe/Pt ($J_{\mathrm{Fe/Pt}}$) is much greater than that of Tb/Pt ($J_{\mathrm{Tb/Pt}}$)and Eu/Pt ($J_{\mathrm{Eu/Pt}}$) throughout the

testing temperature range [39]. Therefore, the difference in T_1 may originate from the coupling contribution from $J_{\mathrm{Tb/Pt}}$ and $J_{\mathrm{Eu/Pt}}$. It is known that TbIG has a T_{comp}, the net moment of which is dominated by Tb^{3+} at low temperatures. EuIG does not have the T_{comp}, and so the Fe^{3+} always dominates the net moment [40, 41]. In other words, Eu^{3+} and Tb^{3+} have different magnetic contributions, and for sandwich structure samples with the same device size, the intensity of SHE and MPE at different REIG/Pt interfaces will be affected.

The different contributions of $J_{\mathrm{Tb/Pt}}$ and $J_{\mathrm{Eu/Pt}}$ in spin transport can also be reflected through the slopes of R_{AHE}^{0} in Fig. 6.8(b). The slopes of R_{AHE}^{0} in Samples A-C are obviously steeper than that of Sample D. As R_{AHE}^{0} is related to the ability of the interface spin transport, the competition between MPE and SHE in Samples A-C may be more intense than that of Sample D. Thereby, the coupling energy $J_{\mathrm{Eu/Pt}}$ in Sample D is considered weaker than that of $J_{\mathrm{Tb/Pt}}$ in Samples A-C. If $J_{\mathrm{Fe/Pt}}$ is constant in all samples and excluded from comparison, the variation of $J_{\mathrm{REIG/Pt}}$ can be judged by the difference of $J_{\mathrm{RE/Pt}}$. The difference of $J_{\mathrm{REIG/Pt}}$ can be expressed by the model in Fig. 6.11. Because the interfacial MPE and SHE are competitive [13, 42], it finally results in the appearance of T_1. The T_1 variations display interface dependence, proving the sensitivity of the interfacial exchange coupling.

Given the complex multilayer structure, the changes in T_1 may require consideration of multiple factors. Due to the possible influence of interface quality on the coupling energy of REIG/Pt interface, the difference in interfacial roughness should be considered. As mentioned in Fig. 6.2, the roughness of the four samples seems to be somewhat correlated with the displayed interface sensitivity. The roughness of Samples A-C is similar, with values of 0.305 nm, 0.371 nm, and 0.382 nm, respectively, but Sample D is much rougher (0.537 nm). Therefore, the roughness effect of the topmost interface, as induced by different stacking orders, cannot be excluded. Different roughness could in turn lead to a change in the exchange coupling energy. From the

results, it appears that roughness has an impact on the difference in interface coupling energy, which indirectly reflects the interface sensitivity of T_1.

6.4 Conclusion

In summary, this Chapter analyzed the relative contributions of modulated REIG bulk and REIG/Pt interfaces on two cross-over points of R_{AHE}^{0}. I modulated the stacking orders of TbIG/EuIG/TbIG films with a fixed total thickness. The main results are highlighted below:

(1) The variations in T_{comp} of multilayer films originate the exchange coupling between different REIG layers, and the stacking order hardly affects the T_{comp} because of the inherent compensation mechanism of REIG.

(2) The fluctuation of M_s and T_{comp} values may be attributed to different RE:Fe ratio caused by deposition sequences, as well as difficulties in accurately controlling the layer thickness.

(3) The T_1 shows strong REIG/Pt interface sensitivity. Different stacking sequences may affect the interface quality, thereby altering interfacial spin transport.

References for Chapter 6

[1] S. Geprags, A. Kehlberger, F.D. Coletta, Z. Qiu, E.J. Guo, T. Schulz, C. Mix, S. Meyer, A. Kamra, M. Althammer, H. Huebl, G. Jakob, Y. Ohnuma, H. Adachi, J. Barker, S. Maekawa, G.E.W. Bauer, E. Saitoh, R. Gross, S.T.B. Goennenwein, M. Klaui, Origin of the spin Seebeck effect in compensated ferrimagnets, Nat. Commun. 7 (2016) 10452.

[2] M.V. Logunov, S.S. Safonov, A.S. Fedorov, A.A. Danilova, N.V. Moiseev, A.R. Safin, S.A. Nikitov, A. Kirilyuk, Domain wall motion across magnetic and spin compensation points in magnetic garnets, Phys. Rev. Appl. 15 (2021) 064024.

[3] Y.K. Liu, H.F. Wong, K.K. Lam, K.H. Chan, C.L. Mak, C.W. Leung, Anomalous Hall effect in Pt/$Tb_3Fe_5O_{12}$ heterostructure: Effect of compensation point, J. Magn. Magn. Mater. 468 (2018) 235-240.

[4] B.W. Dong, J. Cramer, K. Ganzhorn, H.Y. Yuan, E.J. Guo, S.T.B. Goennenwein, M. Klaui, Spin Hall magnetoresistance in the non-collinear ferrimagnet GdIG close to the compensation temperature, J. Phys. Condens. Matter. 30 (2018) 035802.

[5] Y.J. Hong, J.S. Kum, I.B. Shim, C.S. Kim, Spin rotation at compensation point studies of $Tb_3Fe_5O_{12}$ by Mössbauer spectroscopy, IEEE Trans. Magn. 40 (2004) 2808-2810.

[6] J.M. Liang, X.W. Zhao, Y.K. Liu, P.G. Li, S.M. Ng, H.F. Wong, W.F. Cheng, Y. Zhou, J.Y. Dai, C.L. Mak, C.W. Leung, The thickness effect on the compensation temperature of rare-earth garnet thin films, Appl. Phys. Lett. 122 (2023) 242401.

[7] J.J. Bauer, P. Quarterman, A.J. Grutter, B. Khurana, S. Kundu, K.A. Mkhoyan, J.A. Borchers, C.A. Ross, Magnetic proximity effect in magnetic-insulator/heavy-metal heterostructures across the compensation temperature, Phys. Rev. B 104 (2021) 094403.

[8] J.J. Bauer, E.R. Rosenberg, S. Kundu, K.A. Mkhoyan, P. Quarterman, A.J. Grutter, B.J. Kirby, J.A. Borchers, C.A. Ross, Dysprosium iron garnet thin films with perpendicular magnetic anisotropy on silicon, Adv. Electron. Mater. 6 (2019) 1900820.

[9] Y. Li, D. Zheng, C. Liu, C. Zhang, B. Fang, A. Chen, Y. Ma, A. Manchon, X. Zhang,

Current-induced magnetization switching across a nearly room-temperature compensation point in an insulating compensated ferrimagnet, ACS Nano 16 (2022) 8181-8189.

[10] L. Liu, Z. Fan, Z. Chen, Z. Chen, Z. Ye, H. Zheng, Q. Zeng, W. Jia, S. Li, N. Wang, J. Liu, L. Ma, T. Lin, M. Qiu, S. Li, P. Han, J. Shi, H. An, Spin–orbit torques in heavy metal/ferrimagnetic insulator bilayers near compensation, Appl. Phys. Lett. 119 (2021) 052401.

[11] A. Chanda, C. Holzmann, N. Schulz, J. Seyd, M. Albrecht, M.H. Phan, H. Srikanth, Scaling of the thermally induced sign inversion of longitudinal spin Seebeck effect in a compensated ferrimagnet: Role of magnetic anisotropy, Adv. Funct. Mater. 32 (2022) 2109170.

[12] E. P. Wohlfarth, (Ed). *Handbook of magnetic materials* (Vol. 2), (North-Holland, Amsterdam,1980).

[13] S. Ding, Z. Liang, C. Yun, R. Wu, M. Xue, Z. Lin, A. Ross, S. Becker, W. Yang, X. Ma, D. Chen, K. Sun, G. Jakob, M. Kläui, J. Yang, Anomalous Hall effect in magnetic insulator heterostructures: Contributions from spin-Hall and magnetic-proximity effects, Phys. Rev. B 104 (2021) 224410.

[14] N. Nagaosa, J. Sinova, S. Onoda, A.H. MacDonald, N.P. Ong, Anomalous Hall effect, Rev. Mod. Phys. 82 (2010) 1539-1592.

[15] H. Nakayama, M. Althammer, Y.T. Chen, K. Uchida, Y. Kajiwara, D. Kikuchi, T. Ohtani, S. Geprags, M. Opel, S. Takahashi, R. Gross, G.E. Bauer, S.T. Goennenwein, E. Saitoh, Spin Hall magnetoresistance induced by a nonequilibrium proximity effect, Phys. Rev. Lett. 110 (2013) 206601.

[16] Y.-T. Chen, S. Takahashi, H. Nakayama, M. Althammer, S.T.B. Goennenwein, E. Saitoh, G.E.W. Bauer, Theory of spin Hall magnetoresistance, Phys. Rev. B 87 (2013) 144411.

[17] Y.F. Li, X.H. Yang, H. Bai, M.Z. Wang, D.S. Cheng, C. Song, Z. Yuan, Y. Liu, Z. Shi, Strain-tunable magnetic compensation temperature of epitaxial $Tb_3Fe_5O_{12}$ thin films, Phys. Rev. B 108 (2023) 184403.

[18] T. Fu, S. Li, X. Feng, Y. Cui, J. Yao, B. Wang, J. Cao, Z. Shi, D. Xue, X. Fan, Complex anomalous Hall effect of CoGd alloy near the magnetization compensation temperature, Phys. Rev. B 103 (2021) 064432.

[19] T. Xu, Y. Cheng, Y. Dong, H. Bai, H.-A. Zhou, X. Shu, P. Gargiani, M. Valvidares, P. Yu, W. Jiang, Evolution of compensated magnetism and spin-torque switching in ferrimagnetic $Fe_{1-x}Tb_x$, Phys. Rev. Appl. 19 (2023) 034088.

[20] S. Becker, Z. Ren, F. Fuhrmann, A. Ross, S. Lord, S. Ding, R. Wu, J. Yang, J. Miao, M. Kläui, G. Jakob, Magnetic coupling in $Y_3Fe_5O_{12}/Gd_3Fe_5O_{12}$ heterostructures, Phys. Rev. Appl. 16 (2021) 014047.

[21] W. Zhang, M.B. Jungfleisch, W. Jiang, Y. Liu, J.E. Pearson, S.G.E.t. Velthuis, A. Hoffmann, F. Freimuth, Y. Mokrousov, Reduced spin-Hall effects from magnetic proximity, Phys. Rev. B 91 (2015) 115316.

[22] C. Tang, P. Sellappan, Y. Liu, Y. Xu, J.E. Garay, J. Shi, Anomalous Hall hysteresis inTm3Fe5O12/Ptwith strain-induced perpendicular magnetic anisotropy, Phys. Rev. B 94 (2016) 140403.

[23] L. Liu, J. Ye, H. Yang, L. Lin, H. An, Tunable anomalous Hall effect in Pt/ferrimagnetic insulator bilayer, Appl. Phys. Lett. 124 (2024) 132409.

[24] P.G. Li, J.M. Liang, S.M. Ng, H.F. Wong, Y. Zhou, L.J. Huang, K.W. Lin, Y.H. Tsang, C.L. Mak, C.W. Leung, Tunable compensation temperature through ferromagnetic coupling in perpendicular $Tb_3Fe_5O_{12}/Eu_3Fe_5O_{12}$ bilayer heterostructure, J. Magn. Magn. Mater. 592 (2024) 171785.

[25] H. Fuess, G. Bassi, M. Bonnet, A. Delapalme, Neutron scattering length of terbium structure refinement and magnetic moments of terbium iron garnet, Solid State Commun. 18 (1976) 557-562.

[26] S. Mokarian Zanjani, M.C. Onbaşlı, Predicting new iron garnet thin films with perpendicular magnetic anisotropy, J. Magn. Magn. Mater. 499 (2020) 166108.

[27] V.H. Ortiz, B. Arkook, J. Li, M. Aldosary, M. Biggerstaff, W. Yuan, C. Warren, Y. Kodera, J.E. Garay, I. Barsukov, J. Shi, First- and second-order magnetic anisotropy and damping of europium iron garnet under high strain, Phys. Rev. Mater. 5 (2021)

124414.

[28] V.H. Ortiz, M. Aldosary, J. Li, Y. Xu, M.I. Lohmann, P. Sellappan, Y. Kodera, J.E. Garay, J. Shi, Systematic control of strain-induced perpendicular magnetic anisotropy in epitaxial europium and terbium iron garnet thin films, APL Mater. 6 (2018) 121113.

[29] S.M. Zanjani, M.C. Onbasli, Thin film rare earth iron garnets with perpendicular magnetic anisotropy for spintronic applications, AIP Adv. 9 (2019) 035024.

[30] R. Yadav, A. Bake, W.T. Lee, Y.-K. Liu, D.R.G. Mitchell, X.-R. Yang, D.L. Cortie, K.-W. Lin, C.W. Leung, Interfacial spin structures in Pt/$Tb_3Fe_5O_{12}$ bilayer films on $Gd_3Ga_5O_{12}$ substrates, Phys. Rev. Mater. 7 (2023) 124407.

[31] J.M. Gomez-Perez, S. Vélez, L. McKenzie-Sell, M. Amado, J. Herrero-Martín, J. López-López, S. Blanco-Canosa, L.E. Hueso, A. Chuvilin, J.W.A. Robinson, F. Casanova, Synthetic antiferromagnetic coupling between ultrathin insulating garnets, Phys. Rev. Appl. 10 (2018) 044046.

[32] S.M. Suturin, A.M. Korovin, V.E. Bursian, L.V. Lutsev, V. Bourobina, N.L. Yakovlev, M. Montecchi, L. Pasquali, V. Ukleev, A. Vorobiev, A. Devishvili, N.S. Sokolov, Role of gallium diffusion in the formation of a magnetically dead layer at the $Y_3Fe_5O_{12}$/$Gd_3Ga_5O_{12}$ epitaxial interface, Phys. Rev. Mater. 2 (2018) 104404.

[33] R. Kumar, S.N. Sarangi, D. Samal, Z. Hossain, Positive exchange bias and inverted hysteresis loop in $Y_3Fe_5O_{12}$/$Gd_3Ga_5O_{12}$, Phys. Rev. B 103 (2021) 064421.

[34] J.J. Bauer, E.R. Rosenberg, C.A. Ross, Perpendicular magnetic anisotropy and spin mixing conductance in polycrystalline europium iron garnet thin films, Appl. Phys. Lett. 114 (2019) 052403.

[35] E.R. Rosenberg, L. Beran, C.O. Avci, C. Zeledon, B. Song, C. Gonzalez-Fuentes, J. Mendil, P. Gambardella, M. Veis, C. Garcia, G.S.D. Beach, C.A. Ross, Magnetism and spin transport in rare-earth-rich epitaxial terbium and europium iron garnet films, Phys. Rev. Mater. 2 (2018) 094405.

[36] Y. Wang, X. Wang, A.T. Clark, H. Chen, X.M. Cheng, J.W. Freeland, J.Q. Xiao, Probing exchange bias at the surface of a doped ferrimagnetic insulator, Phys. Rev.

Mater. 5 (2021) 074409.

[37] S. Damerio, C.O. Avci, Sputtered terbium iron garnet films with perpendicular magnetic anisotropy for spintronic applications, J. Appl. Phys. 133 (2023) 073902.

[38] W.P. Wolf, J.H. Van Vleck, Magnetism of europium garnet, Phys. Rev. 118 (1960) 1490-1492.

[39] Q. Shao, A. Grutter, Y. Liu, G. Yu, C.-Y. Yang, D.A. Gilbert, E. Arenholz, P. Shafer, X. Che, C. Tang, M. Aldosary, A. Navabi, Q.L. He, B.J. Kirby, J. Shi, K.L. Wang, Exploring interfacial exchange coupling and sublattice effect in heavy metal/ferrimagnetic insulator heterostructures using Hall measurements, x-ray magnetic circular dichroism, and neutron reflectometry, Phys. Rev. B 99 (2019) 104401.

[40] S. Geller, H.J. Williams, R.C. Sherwood, J.P. Remeika, G.P. Espinosa, Magnetic study of the lighter rare-earth ions in the iron garnets, Phys. Rev. 131 (1963) 1080-1082.

[41] S. Geller, J.P. Remeika, R.C. Sherwood, H.J. Williams, G.P. Espinosa, Magnetic study of the heavier rare-earth iron garnets, Phys. Rev. 137 (1965) A1034-A1038.

[42] X. Liang, Y. Zhu, B. Peng, L. Deng, J. Xie, H. Lu, M. Wu, L. Bi, Influence of interface structure on magnetic proximity effect in Pt/$Y_3Fe_5O_{12}$ heterostructures, ACS Appl. Mater. Inter. 8 (2016) 8175-8183.

Chapter 7 Conclusions and outlook

7.1 Summary of results

This project mainly focuses on the spin magnetotransport behavior of TbIG/Pt systems with perpendicular magnetic anisotropy. The spin magnetotransport is primarily reflected by the AHE loops, which display two sign cross-over temperatures. One is related to the net magnetization of different sublattices and is regarded as a bulk effect, while the other is related to the competition between MPE and SHE-induced AHE at the TbIG/Pt interface, which belongs to the interface effect.

Here, I explored three issues related to the two cross-over points. Firstly, the controllability of interfacial spin transport was studied using a non-magnetic spacer. Secondly, the controllability of T_{comp} was studied through bilayer film thickness control. Finally, the influence of modulated bulk and different REIG/Pt interfaces on spin transport was investigated by constructing a sandwich structure with a fixed total thickness.

The main results are summarized below:

(1) The impact of ultrathin garnet-like spacer on spin magnetotransport in epitaxial TbIG/Pt systems was studied. The R_{AHE} sign in TbIG/YAG/Pt systems showed two sign cross-overs, of which the T_{comp} of all samples had not changed, indicating that changes in the interface did not affect the internal magnetism of TbIG. However, as the YAG thickness increased, the competition between MPE and SHE at the TbIG/Pt interface was significantly affected, with T_1 dropped drastically from 135 K to 35 K. Additionally, the YAG spacer showed stronger magnon tunneling ability in spin magnetotransport than GGG spacer, which was attributed to strong Gd^{3+} moment disturbance below Curie temperature of GGG.

(2) The modulated T_{comp} in TbIG was studied by constructing TbIG/EuIG bilayers. Bilayer garnets with similar structures could maintain the PMA when deposited on GGG (111) substrate, because there was no significant stress change compared with

single-layer GGG/TbIG and GGG/EuIG. The H_c and R_{AHE}^0 in all GGG/TbIG (30 nm)/EuIG (t nm)/Pt samples showed two sign cross-overs. T_{comp} showed a strong EuIG thickness dependence, and the tunable T_{comp} in the bilayer system was attributed to the ferromagnetic coupling of the two REIG layers. Therefore, the regulation of spin Hall magnetotransport in TbIG can be achieved through additional REIG layers.

(3) The effect of modulated sandwich bulk and REIG/Pt interface on spin magnetotransport was studied. The modulated GGG/TbIG/EuIG/TbIG films maintained a fixed total thickness but a different layer stacking order. The results indicated that the stacking order hardly affected T_{comp} because of the inherent compensation mechanism of REIG. The fluctuation of M_s and T_{comp} may be attributed to different RE:Fe ratios caused by deposition sequences and difficulties in accurately controlling thickness. Besides, the T_1 showed strong REIG/Pt interface sensitivity. Different stacking sequences may affect the interface quality, thereby altering interfacial spin transport.

7.2 Future work

During my research on these topics, I noticed that some issues need to be addressed, as well as some ideas that I recommend for future work. If the following issues can be further explored, I believe research on garnets with compensation behavior will be more comprehensive and provide guidance for similar studies.

(1) In Chapter 4, I mentioned that the GGG spacer has a stronger disturbance on spin transport than the YAG spacer because of the Gd^{3+} moment. Polarized neutron reflectometry technology could help to analyze the magnetic moment of different spacers.

(2) In bilayer and sandwich systems, I mentioned ferromagnetic coupling between the garnet layers, and the REIG/Pt interface is dominated by Fe/Pt coupling. However, the specific coupling energy has not been calculated. First-principles calculations can help evaluate the coupling energy between different sublattices at the interface and confirm the hypothesis.

(3) The strength of magnetic proximity effects in Pt depends on the magnetization of the REIG. Measuring the magnetization induced in Pt is challenging yet meaningful when studying the competition between SHE and MPE. XMCD or Lorentz microscopy techniques can be used to study MPE intensity in future research.